CHARACTERISTICS OF TROPICAL MIDLEVEL CLOUDS USING A-TRAIN MEASUREMENTS

A Thesis

by

ALISHA BROOKE SUTPHIN

Submitted to the Office of Graduate Studies of
Texas A&M University
in partial fulfillment of the requirements for the degree of

MASTER OF SCIENCE

Chair of Committee,	Shaima Nasiri
Co-Chairs of Committee,	Anita Rapp
Committee Member,	Brendan Roark
Head of Department,	Ping Yang

August 2013

Major Subject: Atmospheric Science

Copyright 2013 Alisha Brooke Sutphin

ABSTRACT

Midlevel clouds are observed globally and impact the general circulation through their influence on the radiation budget and their precipitation production. However, because midlevel clouds occur less frequently than high and low clouds they are relatively understudied. Satellite observations from the MODIS, CALIPSO, and CloudSat instruments onboard the A-Train are combined to study midlevel cloud characteristics in the Tropical Western Pacific (TWP) between January 2007 and December 2010. Characteristic cloud and microphysical properties including cloud top height (CTH), geometric thickness, optical depth, effective radius, and liquid or ice water path (LWP or IWP), and environmental properties, including temperature and specific humidity profiles, are determined for precipitating and non-precipitating midlevel clouds.

In the study region, approximately 14% of all cloudy scenes are classified as midlevel clouds (4 km < CTH < 8 km). These are concentrated in areas of deeper convection associated with the Pacific warm pool, ITCZ, and SPCZ. Non-precipitating clouds dominate the region, accounting for approximately 70% of all single and two-layer midlevel clouds scenes. Midlevel clouds occur most frequently in three different scenarios: high over midlevel clouds (~65%), single-layer (~25%), and midlevel over mid- or low-level clouds (~10%). Environmental moisture appears to play a larger role than temperature in determining midlevel cloud distributions due to large variations in moisture between the different cloud scenarios.

In all scenes, a trimodal distribution in CTH frequency is found within the midlevel. Two of these peaks have been identified in previous studies, however a third midlevel mode is recognized here. CTHs occur most frequently in peaks between 5-6 km, 6-6.25 km, and 6.5-7.5 km. Although the past studies have only noted two midlevel peaks, this third mode is a robust feature in this dataset. Two types of clouds dominate these peaks: non-precipitating altostratus or altocumulus-like clouds less than 1 km thick and geometrically thick precipitating cumulus congestus clouds. Environmental temperature stable layers and dry maxima are found at each one of these peak frequency heights. Again, moisture seems to play a more dominant role in determining the height of the midlevel clouds due to larger variances between the moisture gradients associated with each peak.

Microphysical properties (optical depth, effective radius, and LWP or IWP) are characterized for single-layer clouds. Approximately 30% of all single-layer midlevel clouds are precipitating and these clouds tend to occur on the edges of the deep tropics. In general, precipitating clouds have greater optical depths, effective radii, and water path. This research implies that some past studies at single point locations can be representative of the broader tropics, whereas others are not.

DEDICATION

This thesis is dedicated to my family who have guided and supported me throughout my entire life with their unconditional love. Without them, none of this would have been possible.

.

ACKNOWLEDGEMENTS

I would like to first thank my committee chairs, Dr. Shaima Nasiri and Dr. Anita Rapp, and my committee member, Dr. Brendan Roark, for their guidance and tremendous support throughout the course of this research.

Thanks also go to my friends and colleagues and the department faculty and staff for making my six years at Texas A&M University a great experience. I also want to extend my gratitude to a fellow graduate student, Amanda DePasquale, who helped me throughout this entire process.

Finally, thanks to my mother and father and the rest of my family for their encouragement and support for the last two years.

TABLE OF CONTENTS

Page

LIST OF FIGURES

LIST OF TABLES

TABLE Page

1. INTRODUCTION AND LITERATURE REVIEW

1.1. Midlevel cloud overview

Midlevel clouds are observed globally and cover 10-30% of our planet (Hahn and Warren 2003; Stubenrauch et al. 2006). These clouds play a vital role in the Earth's general circulation through their effects on the radiation budget and their precipitation production (Johnson et al. 1999; Zhang et al. 2010). However, they have not been as frequently studied as high and low clouds and therefore, their characteristics and radiative effects are not as well understood (Mace et al. 2006; Riihimaki et al. 2012).

It is difficult to compare past studies of midlevel clouds because there are different definitions of what actually encompasses the midlevel. Depending on location, observation technique, and purpose of the study, the midlevel can be classified in many different ways. For example, studies using surface observations have often used cloud top or base heights to classify midlevel clouds, whereas satellite observation studies have used cloud top pressures. Recent efforts by Hongchun Jin, a member of Dr. Nasiri's research group, showed that changing the criteria for midlevel cloud identification could have large effects on the outcome of cloud frequency. For example, if midlevel clouds were defined by their base height (base between 2 and 5 km), then there were notably fewer midlevel clouds than if the International Satellite Cloud Climatology Project (ISCCP) definition of cloud top pressures between 680 and 440 hPa (Jin, Ph.D. dissertation, 2012) were used.

Although this study focuses on the tropics, midlevel clouds are also observed in the mid-latitudes and high-latitudes (Figure 1). Previous studies have shown that tropical midlevel clouds differ from their counterparts in the mid- and high-latitudes in frequency, thickness, and phase (e.g. Rossow and Zhang 2010; Seifert et al. 2010; Zhang et al. 2010; Jin, Ph.D. dissertation, 2012). Rossow and Zhang (2010) found that the number of midlevel clouds increases as you move from lower to higher latitudes. They also showed that midlevel clouds occur less often than low and high-level clouds, except in polar regions. Zhang et al. (2010) observed higher frequencies of thin midlevel clouds during nighttime overpasses than daytime overpasses using the Cloud-Aerosol Lidar and Infrared Pathfinder Satellite Observations (CALIPSO), especially in the tropics.

Midlevel clouds are relatively geometrically thinner in the tropics compared to the mid-latitudes (Zhang et al. 2010; Seifert et al. 2010). It is hypothesized that this low geometric thickness could be a reason for why less ice is observed in tropical midlevel clouds. Hobbs and Rangno (1985) found that thinner clouds might have a narrower liquid drop spectrum, which could lead to less heterogeneous ice formation. Although there are fewer tropical midlevel phase studies than mid- and high-latitude phase studies, some have found that tropical midlevel clouds are more likely to contain liquid water than in the other regions. In Cape Verde, Africa, midlevel clouds were found to have liquid layer tops at temperatures as cold as -36°C (Ansmann et al. 2009). Clouds containing ice in this region were far less frequent than in similar observations over Europe (Seifert et al. 2010). It is suggested that this lower occurrence of ice formation exists in the tropics because of different ice nuclei (i.e. aerosols), meteorology, or a combination of both (Seifert et al. 2010).

Even though tropical midlevel clouds are more likely to contain liquid water, these midlevel clouds can still extend through the 0°C melting layer, and thus have complex microphysics. These clouds can consist of all water droplets, all ice crystals, or a combination of both, also known as mixed phase (Heymsfield et al., 1991, Field 1999, Fleishauer et al., 2002; Riihimaki et al., 2012). The thermodynamic phase of midlevel clouds has a large impact on climate through its influence on the radiation budget (Sun and Shine, 1995). Le Treut et al. (1994) found that the mixed phase can have a substantial impact on shortwave and longwave (SW and LW) radiative forcings when examining various combinations of effective radii and absorption coefficients. Cloud thermodynamic phase has a greater impact on SW cloud forcing than LW cloud forcing, however, LW cloud forcing is more influenced by cloud temperature. Therefore, understanding the relationships between midlevel clouds and their temperature and phase is necessary for accurate estimates of the midlevel cloud radiative impacts. General circulation models (GCMs) often have difficultly simulating midlevel clouds because of their complex microphysics, frequently underestimating the total amount of midlevel clouds (Zhang et al. 2005; Bodas-Salcedo et al. 2008).

Particularly in the tropics, midlevel clouds play an essential role in convective dynamics. These clouds are frequent during the onset of the Madden-Julian Oscillation (MJO; Madden and Julian, 1972 or 1994), a 30-60 day eastward propagating oscillation originating in the Indian Ocean. Midlevel clouds are thought to moisten the atmosphere for deep convection associated with peak rainfall events in the MJO (Thayer-Calder and Randall 2009; Del Genio et al. 2011; Riley et al. 2011). However, convection parameterizations continue to have difficulty capturing this evolution (Inness et al. 2001; Hagos et al. 2011), which will be further addressed in the challenges of midlevel clouds in section 1.3.

The formation of midlevel clouds in the tropics depends heavily on convective meteorology, differing from mid-and high-latitudes (Riihimaki et al. 2012). In the Tropical Ocean Global Atmosphere Couple Ocean-Atmosphere Response Experiment (TOGA COARE; Webster and Lukas, 1992) stable layers were observed around the 0°C-melting layer in the tropics. These layers of heightened stability are thought to occur due to several different factors including advection of dry layers (Mapes and Zuidema 1996), melting effects (Johnson et al. 1996; Yasunaga et al. 2006) and radiative effects (Johnson et al. 1996). Some midlevel clouds, especially cumulus congestus, are believed to form when these stable layers inhibit cloud growth and cause detrainment, outflow of cloudy air into the surrounding environment, in the mid-troposphere (Mapes and Zuidema 1996; Johnson et al. 1996, Johnson et al. 1999). Detrainment occurs throughout the depth of a deep convective cloud, but dominates near the cloud top (Randall and Huffman 1982).

Before TOGA COARE, shallow and deep convection were the focus of most studies and midlevel convection was largely ignored. However, studies during TOGA COARE revitalized the study of midlevel clouds by recognizing them as a significant mode of convection. A study by Johnson et al. (1999) describes three modes of tropical convection, low trade wind cumulus, midlevel cumulus congestus, and high cumulus towers. Trade wind cumulus clouds, which are the most frequent type of convection in the tropics, are shallow convective clouds that are most prominent in the trade wind regions outside of the Intertropical Convergence Zone (ITCZ) (Lemone and Meitin 1984). These clouds typically only extend to just over 2 km, where large-scale subsidence (sinking of air from the Hadley circulation) and the trade inversion layer hinders cloud growth. Moving closer to the equator, the trade wind inversion layer (also known as a stable layer) slopes upward due to increased sea surface temperatures and decreased large-scale subsidence (Schubert et al. 1995). The second mode of convection in the tropics consists of deep cumulus towers that are typically generated by low-level convergence and extend through the entire depth of the troposphere. Cloud tops are limited to a height of 15-16 km due to the tropopause stable layer (Johnson et al. 1999). The final, relatively less studied, yet important mode of tropical convection is cumulus congestus. It was assumed that these midlevel clouds occur most frequently around the 0°C stable layer (Johnson et al. 1999), however recent studies have found evidence of a midlevel bimodal distribution (Haynes and Stephens; Riley and Mapes 2009).

Haynes and Stephens (2007) performed a three-month study to examine tropical cloudiness and precipitation incidence in the global tropical oceans. They found the three modes of tropical convection described by Johnson et al. (1999), but also a bimodal distribution in midlevel cloud height frequency. Riley and Mapes (2009) further examined this idea of dual peaks in the midlevel cloud distribution and found that midlevel clouds are most frequent between 5-6 km and between 7-8 km (Figure 2). A strong 0°C stable layer (also referred to as the melting layer) is suggested to enhance the cloud population at the 5-6 km peak (Johnson et al. 1999). The melting layer, which is where descending ice melts to water, is an enhanced stable layer due to the latent cooling of the environment. While these are possible explanations for the lower peak, the upper peak is still a mystery. A few theories of the increased cloud frequency between 7-8 km are rapid dendritic ice crystal growth, enhanced detrainment producing shelf clouds, forced gravity waves from melting layer reverberations in the vertical, and enhanced stable layers from midtropospheric dry intrusions (Riley and Mapes 2009). Other studies have supported and built onto this idea of a bimodal distribution in the midlevel (Riihimaki et al., 2012) but have yet to determine which cloud and environmental characteristics drive the two different peaks.

1.2. Midlevel precipitation

The study of tropical shallow and deep clouds has taken precedence in the past because these cloud types were thought to control precipitation in the tropics. However, the TOGA COARE field program recognized the importance of midlevel clouds and their contribution to precipitating cloud totals. Johnson et al. (1999) compared data between the Global Atmospheric Research Program Atlantic Tropical Experiment (GATE) and TOGA COARE field programs and found conclusive evidence to support three important modes of convection. The three different modes of tropical convection are low trade wind cumulus with tops near the trade wind inversion, deep cumulonimbus with tops near the tropopause, and midlevel cumulus congestus that have tops near the melting layer (Figure 3). Cumulus congestus clouds, which are considered midlevel by most definitions, comprised over half (~57%) of the precipitating convective clouds and over one-quarter (~28%) of the total tropical convective rainfall in the Johnson et al. (1999) study. Cumulus congestus are less frequent than shallow convection, but more abundant than deep cumulonimbus, although the deep convection contributes a greater fraction of the total rainfall (Johnson et al. 1999). A number of studies have suggested that convective cloudiness is one of the main regulators of tropical sea surface temperatures and the lower latitude radiation budget (for review see Stephens 2005). Since cumulus congestus are relatively frequent in the tropics, they will have an influence on these parameters.

Stephens and Wood (2007) used observations from various ground-based millimeter-wave radars (MWR) to study precipitation in active and break episodes of the MJO and in an active phase of the monsoon over the Indian Ocean. They found that the majority of tropical precipitating clouds (45% to 53% of all precipitating profiles) occur in multilayer scenes. The most common multilayered scene was higher-level cirrus of varying geometric thickness overlaying cumulus congestus-like convection. The majority of rainfall accumulated during their study (57% for the active monsoon, 53% during the active MJO, and 63% during the transition MJO) was from these multilayered cloud systems.

Midlevel convection has been hypothesized to precondition the atmosphere for deep convection (Johnson et al. 1999; Mapes et al. 2006; Chen and Del Genio 2009; Tromeur and Rossow 2010) and to play a role in the initiation and maintenance of the

MJO (Kikuchi and Takayabu, 2004). These studies noted an increase in cumulus congestus clouds prior to peak rainfall events associated with deep convection. Kikuchi and Takayabu (2004) determined that cumulus congestus clouds are abundant in the “developing stage” a few days before the “mature stage” of the MJO that is associated with heavy rainfall from deep convective clouds. The “discharge-recharge theorem” was coined to describe the lower level preconditioning and is illustrated in Figure 4. It is hypothesized that cumulus congestus clouds help precondition the atmosphere for deeper, more intense convection by moistening the lower atmosphere (Benedict and Randall 2007). These clouds affect the mid-tropospheric vapor field by moistening through detrainment, creating horizontal convergence from low-level heating, and drying from associated precipitation (Takayabu et al. 2010).

Although these clouds play an important role in the dynamics of tropical convection, not many studies have solely focused on midlevel precipitating clouds. Understanding the environment in which these midlevel clouds precipitate and how they contribute to the overall midlevel cloud population is a goal of this thesis.

1.3. Challenges of midlevel clouds

One of the main issues with midlevel clouds is that there are many definitions of what comprises the midlevel and it is important to understand how the differences affect midlevel cloud statistics. Surface-based cloud observations are typically defined by their base height (Hahn and Warren 1999) because detecting the cloud top height is difficult or impossible due to either lack of sight observation or attenuation of radar and lidar. Therefore, surface observations may have difficultly detecting altostratus or altocumulus clouds that are above low layer clouds (Wang et al. 2000). Furthermore, ground-based studies are limited on a spatial scale and therefore may not be globally representative.

Satellite observations, on the other hand, have global coverage; yet again, they come with their own sensitivities and biases. In the past, passive satellite instruments were the most commonly used spaceborne observations. These passive sensors can only view clouds from the top down and therefore only provide direct information on cloud top heights or pressure of the uppermost cloud. However, with the implementation of the National Aeronautics and Space Administration's (NASA) A-Train satellite constellation, a more complete cloud profile can be observed through new active sensors. By using these new combined radar and lidar measurements, vertical cloud distributions have become more accurate (e.g. multi-layered cloud scenarios) (Stephens et al. 2008). However, these active sensors can attenuate in the atmosphere when large aerosols or cloud particles (i.e. precipitation) are present, and therefore may not accurately report cloud base height. For example, when precipitation reaches the surface, high reflectivities from large particles cannot be distinguished from smaller cloud particles or ground clutter and the radar often reports the cloud as extending all the way to the surface (Stephens et al. 2008).

Hongchun Jin (2012) explored the differences between the various definitions of midlevel clouds, shown in Figure 5. This figure is divided between single and multi-layered clouds and shows the frequency of midlevel cloud differences between the cloud-top height definition (tops between 3 and 7 km), the cloud-base height definition (bases between 2 and 5 km), and the ISCCP definition (cloud top pressures between 680 and 440 hPa). Generally, if the cloud-base height definition is used, fewer midlevel clouds are detected than using the cloud-top or ISCCP method. From this figure, midlevel clouds are most frequent when using the cloud-top height method. It is evident here that choosing which parameters define the midlevel will strongly impact your results.

Midlevel clouds are often under represented in GCMs and Numerical Weather Prediction (NWP) models (Zhang et al. 2005; Haynes and Stephens 2007; Bodas-Salcedo et al. 2008). Because midlevel clouds are often found in multilayer clouds scenes, especially in the tropics (Poore et al. 1995; Wang et al. 2000), observations from both the ground and space can be significantly obscured. Comparisons with model output are often difficult because midlevel clouds are often underestimated in observations. Additional issues stem from midlevel clouds frequently extending through the melting layer, creating complex microphysics. Studies have shown that climate models typically underestimate the midlevel mode because they are unable to simulate these complex microphysics and because they cannot capture the midlevel clouds well in multilayer scenes (Zhang et al. 2005; Bodas-Salcedo et al. 2008). Additionally, models underestimate precipitation, perhaps because this midlevel mode is relatively absent (Demott et al. 2007; Nam and Quaas 2012). To improve climate models, a better understanding of the midlevel cloud distribution and midlevel cloud properties is required.

1.4. Organization of thesis

This thesis focuses on a four-year analysis of oceanic midlevel precipitating and non-precipitating clouds in the Tropical Western Pacific (TWP) using NASA's A-train satellite instruments. The actively and passively retrieved cloud and environmental properties are analyzed to determine the differences between precipitating and non-precipitating midlevel clouds. The recent findings of Riley and Mapes (2009), of a bimodal distribution of tropical midlevel clouds will also be more closely examined. Characterizing the precipitating and non-precipitating midlevel cloud properties and the dual peaks will ultimately improve our understanding of these relatively unstudied clouds.

In chapter 2 of this thesis, a review of the data and geographic location of this research project is presented. Chapter 3 describes the methods used in this analysis. Chapter 4 presents the results and discussion on the various characteristics of single and two-layered midlevel cloud scenarios. Chapter 5 presents the results and discussion of the multiple peaks found in the study. Finally, summary and future work are presented in chapter 6.

2. DATA

2.1. NASA's A-Train Constellation

NASAs "A-Train" satellite constellation consists of a set of satellites flying in a sun-synchronous low-earth orbit, crossing the equator around 1:30 p.m. local time within a few seconds of each other (Figure 6). Because of their near-simultaneous observations, instruments onboard different satellites can be used together to study the Earth's atmosphere. Each satellite mission within the A-Train has its own scientific objectives, providing unique contributions to improving our understanding of the changing climate. In this thesis, three of these instruments are used: the Moderate-Resolution Imaging Spectroradiometer (MODIS) onboard Aqua (King et al. 1997), the Cloud-Aerosol Lidar with Orthogonal Polarization (CALIOP) onboard Cloud-Aerosol Lidar and Infrared Pathfinder Satellite Observations (CALIPSO) (Winker et al. 2003), and the Cloud Profiling Radar (CPR) onboard CloudSat (Stephens et al. 2002). Each instrument has different sensitivities and limitations, but when used together, they can create a more complete view of the atmospheric profile. Table 1 shows a list of all A-Train products used in this study.

2.2. Instruments

2.2.1. MODIS

MODIS, launched in May of 2002, is a passive sensor onboard the Aqua satellite. It is a 36-band spectroradiometer (spectral bands ranging from 0.405 and 14.385 μm), measuring both infrared and visible radiances. It has a viewing swath of 2,330 km and is able to observe the entire Earth's surface every one to two days. The spatial resolution of the instrument ranges from 0.25 to 1 km depending on the wavelength, while the spatial resolution of data products depends on the product. MODIS is used to study a variety of different components of the Earth-Atmosphere system such as vegetation, cloud and aerosol properties, and land surface cover (Frey et al. 2008). This research uses a combination of MAC06S0 and MAC03S0 retrievals (referred to as Level-2 data products) at 1- and 5-km spatial resolution, which contain a subset of the MODIS MYD06 Cloud Product along the CloudSat track. These MODIS products are collocated with CloudSat and subset to the three pixels from each scan nearest the CloudSat track are kept from each scan.

MODIS employs a cloud mask algorithm that uses as many as 20 of the 36 spectral bands to maximize cloud detection (Ackerman et al. 1998). For every pixel, MODIS classifies the scene as confident clear, probably clear, uncertain/probably clouds, or cloudy. Uncertainties occur more frequently over land than ocean due to complex land surface characteristics. Cloud masking is also inherently more difficult during nighttime scenes, especially when a strong temperature inversion is present (Platnick et al. 2003).

Cloud top properties, such as pressure, temperature, and height, are found using a CO_2 slicing technique. This technique utilizes differing partial absorption in several of the MODIS infrared bands located within the 15-µm CO_2 absorption region. Specifically, the product uses ratios between MODIS spectral bands of 11-µm, 13.3-µm, 13.6-µm, 13.9-µm, and 14.2-µm and has a spatial resolution of 5 km at nadir. Because each CO_2 band is sensitive to a different level in the atmosphere, cloud top pressures can be retrieved for high and midlevel clouds. The 11-µm channel is used to retrieve cloud top temperature of low level clouds (Platnick et al. 2003). The MODIS infrared retrievals are used in this thesis to determine cloud top temperature.

MODIS provides information on cloud thermodynamic phase, optical depth, and microphysical properties (effective radius, water path) using simultaneous visible and near-infrared reflectance measurements (Nakajima and King, 1990). These properties are derived from spectral bands that include window regions in the visible and near-infrared, as well as the 1.6- and 2.1-µm shortwave infrared (SWIR) and the 3.7-µm midwave infrared band (MWIR) windows (Platnick et al. 2003). Cloud particle phase detection uses a combination of the 0.65 µm, 1.64 µm, and 2.13 µm wavelengths. The visible reflectance (0.65 µm band) has no appreciable absorption for either ice or liquid water, however, if the cloud contains ice, then reflectance at the 1.64 µm band will be smaller than for a liquid water cloud. The 2.13 µm band also shows a decrease in reflectance for ice. Accurate phase is imperative because it is an input to both the optical depth and effective radius retrievals. This thesis is limited to daytime only scenes because optical depth and effective radius are only retrieved from visible and near-infrared channels. Optical depth and effective radius are measured from the 0.65 μm, 2.13 μm, and 3.75 μm bands. The underlying principle is that the reflection function of clouds at the 0.65-μm band will be primarily a function of optical depth, whereas the reflection function at the 2.13-μm band is a function of particle size (Nakajima and King, 1990). It is important to note here that the liquid and ice water paths (LWP or IWP) are calculated from effective radius and optical depth. The MODIS retrieval calculates LWP and IWP (Equation 1 and 2) from the retrieved values of optical depth (τ) and cloud top effective radius (r_e). The density of water (1 g/cm^3) is represented by ρ_w.

$$\mathrm{LWP} = \frac{2}{3}\rho_w \tau r_e \qquad (1)$$

$$\mathrm{IWP} = 0.93 * \frac{2}{3}\rho_w \tau r_e \qquad (2)$$

2.2.2. CALIPSO

CALIPSO, launched in April 2006, uses a combination of an active lidar instrument with passive visible and infrared imagers to view properties of thin clouds. CALIPSO consists of three different nadir-viewing instruments: the CALIOP, the Infrared Imaging Radiometer (IIR), and the Wide Field Camera (WFC) (Winker et al. 2003). CALIOP provides high vertical resolution of aerosols and clouds and will be the focus of these three instruments in this study.

CALIOP is an active polarization-sensitive elastic backscatter lidar that transmits laser pulses at wavelengths of 1063 nm and 532 nm. Below 8.2 km, the maximum vertical and horizontal resolutions of this instrument are 30 m and 333 m. Between 8.2 and 20.2 km, they are 60 m and 1000 m, respectively (Winker et al. 2009). This study uses the lidar level 2 cloud and aerosol layer product that has a resolution of 1 km and identifies up to 10 cloud layers (CAL-LID_L2_01km_CLay) (Powell et al. 2010). The two lidar profiles provide information on the vertical distributions of aerosols and clouds, cloud ice/water phase, and aerosol size. The depolarization ratio provided by the CALIOP's 532 nm channel helps determine if the particle is ice or liquid water (Hu et al. 2009). CALIOP assumes that minimal depolarization occurs with spherical liquid particles, whereas ice particles are depolarizing (Sassen 1991). Cloud phase is detected using the spatial correlation of layer-integrated depolarization ratio, attenuated backscatter, and other factors including cloud temperature. Water clouds typically have a positive correlation between the layer-integrated depolarization ratio and attenuated backscatter, whereas ice clouds tend to be negatively correlated. The phase detection occurs in two steps. The first step uses a two-dimensional threshold method to provide an initial identification of ice clouds containing randomly oriented ice crystals, horizontally oriented ice crystals, and possible water clouds. The second step applies a spatial coherence analysis to distinguish water clouds from ice clouds containing horizontally oriented ice crystals (Hu et al. 2009).

Measurements made by the 532-nm channel are sensitive to thin clouds and aerosols, which makes the CALIOP most beneficial at detecting upper-level thin cirrus layers (Winker et al. 2003). In this analysis, CALIPSO cloud phase and cloud top and base heights are used. Because the CloudSat radar tends to miss thin clouds and the lidar gets attenuated in thick clouds (Stephens et al. 2008, Mace et al. 2009), a combined lidar-radar product (2B-GEOPROF-LIDAR within CloudSat, see next section) is used here to obtain the full atmospheric cloud profile (Stephens et al. 2002).

2.2.3. CloudSat

CloudSat, along with CALIPSO, was launched in April of 2006 and lags MODIS by approximately 120 seconds in orbit (Stephens et al. 2002). CloudSat carries the CPR, an active 94 GHz near-nadir-looking radar designed to observe clouds and precipitation from space. The CPR has a footprint of approximately 1.4 km across-track and 1.7 km along-track. CloudSat has a vertical resolution of 500 m, however, oversampling is utilized to produce an effective range sampling of approximately 250 m (Mace et al. 2007). This radar operates at millimeter-wavelength to detect all cloud particles, rather than just precipitation-sized droplets like centimeter-wavelength radars (Stephens et al. 2002). The minimum detectable signal is between -30 and -31 dBZ and the maximum detectable signal is approximately 29 dBZ (Haynes and Stephens 2007). With this range of sensitivity, a majority of clouds that significantly affect the radiation budget are detected (Stephens et al. 2008). Note here though that CloudSat will miss thin clouds, which are also important to radiation calculations. The lower the minimum detectable signal, the higher sensitivity the radar has to smaller particles in the atmosphere. Because millimeter radars are more sensitive to smaller particles, if larger particles are present (i.e. precipitation) the signal can become attenuated. Although CloudSat might not have as accurate rainfall rate measurements as centimeter-wavelength radars due to attenuation, CloudSat rainfall rates are estimated to be valid to about 5-8 mm/h (Stephens et al. 2002). However, for this study, CloudSat is just used as a precipitation mask and thus accurate rain rates are not necessary. Four CloudSat products are used to capture the characteristics of precipitating and non-precipitating tropical midlevel clouds in this study: 2B-GEOPROF, 2C-PRECIP-COLUMN, ECMWF-AUX, and 2B-GEOPROF-LIDAR.

CloudSat's CPR measures backscattered radiation as a function of distance from both solid (i.e. surface) and distributed (i.e., cloud particles) targets. Cloud detection information by the CPR is initially stored in the 2B-GEOPROF product (Mace et al. 2007). A cloud mask is created in this product and has values that range from 0 to 40. This cloud mask measures when the power returned (radiation reflected back towards the satellite) is likely due to clouds or other hydrometers or when it is likely to contain only noise. The higher the value, the less likely it is a false detection. One of the limitations of CloudSat is that of surface clutter. Because of ground noise, the signal from clouds is significantly masked in the lowest 750 meters, eliminating some low-level clouds and base heights from detection. In addition to cloud mask, this product also includes the radar reflectivity (power returned) and other quality indicator flags (Marchand et al., 2008). This product is also used in this analysis as a land mask. However, other data products, such as the 2C-PRECIP-COLUMN and 2B-GEOPROF-LIDAR, use the cloud top and base heights and reflectivity values from this product.

The 2C-PRECIP-COLUMN is used to detect precipitation in this study. The 2C-PRECIP-COLUMN estimates rain occurrence and intensity based on radar reflectivity and an estimate of path integrated attenuation (PIA) determined from surface reflection characteristics (Haynes et al. 2009). The presence of rain is closely related to the unattenuated radar reflectivity, Z_u, which is the sum of measured reflectivity, the PIA, and a component due to gaseous attenuation (determined from the ECMWF-AUX temperature and moisture profile). The higher the Z_u, the more likely a cloud is precipitating (Haynes et al. 2009). Attenuation-corrected reflectivity thresholds are included in the 2C-PRECIP-COLUMN algorithm to identify the likelihood of a profile containing precipitation. The following precipitation flags used in this analysis and their associated attenuation-corrected reflectivity range in dBZ are: 1-rain possible (-15 to 7.5), 2-rain probably (-7.5 to 0), and 3-rain certain (>0) (Haynes et al. 2009). This precipitation flag also includes flags for snow or mixed precipitation, but since this analysis is confined to tropics, these flags will not be used here.

The 2B-GEOPROF-LIDAR is the most important product for detecting midlevel clouds in this study. This product combines the CloudSat radar and CALIPSO lidar cloud masks to give the most representative cloud profile (Stephens et al. 2002). Because the radar's minimum detectable signal is around -31dBZ, a fraction of high thin cirrus and non-precipitating water clouds will be below the detection threshold of the CPR. It is for this reason that the lidar, which is able to detect these thinner, smaller particle clouds, is combined with the radar in this product (Marchand et al. 2008). Because the radar and lidar have different spatial and vertical resolutions (lidar finer resolution than radar), the 2B-GEOPROF-LIDAR combines the two instruments using a weighting scheme based on the spatial probability of overlap. A layer boundary is defined as the first appearance of a cloudy layer (either detected by the radar or lidar) following a cloud-free layer (Mace et al. 2009). The 2B-GEOPROF-LIDAR product reports the total number of cloud layers (up to 5), requiring at least one 250 m cloud-free range bin between two cloudy bins to be considered separate layers. The 2B-GEOPROF-LIDAR is used for determining cloud top height, cloud base height, and geometric thickness in this analysis.

2.2.4. Ancillary Data

The ECMWF-AUX is a product that contains the set of ancillary European Center for Medium Range Weather Forecasts (ECMWF) interpolated to each CloudSat CPR bin (Divakarla et al. 2006). The data contained in this product is used to determine environmental temperature and specific humidity (q) profiles along with cloud top temperatures and pressures. Specific humidity is the ratio of water vapor to dry air in a particular mass, measured here in g kg^{-1}.

This study will use sea surface temperatures (SSTs) from the 2C-PRECIP-COLUMN data product. The SSTs in this product are from the ECMWF model, again interpolated to each CloudSat CPR bin.

2.3 Area of interest

This study focuses on a four-year period from January 2007 through December 2010 in the tropical western Pacific (TWP). Midlevel clouds in this study are classified as clouds that have tops between 4 and 8 km as defined by Riihimaki et al. (2012). This definition is chosen because Riihimaki's study at the Darwin, Australia Atmospheric Radiation Measurement (ARM) site is recent and lies within the TWP. Riihimaki et al. (2012) used vertically pointing ground-based lidar and radar measurements to provide a four-year climatology of midlevel clouds. As with many ground-based studies, they only investigated a single location. One goal of this study is to determine whether or not a single surface site can represent the tropics as a whole, therefore satellite datasets are implemented to provide a large-scale analysis. Specifically, daytime, oceanic, midlevel clouds are examined from 20°S–20°N latitude and 125°E-180°E longitude (Figure 7). As mentioned before, only daytime scenes are processed so that retrievals from MODIS visible channels can be utilized in the study.

There are two main reasons why the TWP warrants the focus of this study. The first is that global frequency maps have shown enhanced midlevel clouds in this area compared to other areas in the tropics (Haynes and Stephens 2007; Jin 2012). The second is because this area has been the focus of many past investigations, which will allow comparisons of these results to previous research (e.g. Johnson et al. 1999; Haynes and Stephens 2007; Mather et al. 2007; Riley and Mapes 2009; Riihimaki et. al 2012).

3. METHODOLOGY

3.1. Collocating MODIS, CloudSat, and CALIPSO

Data processing begins with obtaining all daytime MODIS, CloudSat, and CALIPSO data for January 2007 through December 2010 in the study region. All individual product date and time files are stored for processing only when all data products are available (MAC06S0, MAC03S0, 2B-GEOPROF, 2C-PRECIP-COLUMN, ECMWF-AUX, 2B-GEOPROF-LIDAR, and CAL_LID_L2_01km_Clay).

Although these instruments fly in constellation in a sun-synchronous orbit, the MODIS field of view is significantly broader than that of both CloudSat and CALIPSO, as illustrated by the comparison of the CloudSat track and the full MODIS swath in Figure 8. CloudSat and CALIPSO have very similar track widths, therefore the CloudSat track represents both satellites in this figure. Because each instrument has different spatial resolutions, all data will be collocated to the nearest CloudSat pixel.

Collocation is performed on a pixel-by-pixel basis, where each MODIS and CALIPSO pixel is matched with the nearest CloudSat latitude and longitude. Although the MODIS MYD06 data have already been subset to the CloudSat track (MAC06S0 data file), there are still three pixels for every one CloudSat pixel (Figure 9). The three green swaths represent the subset MODIS pixels nearest the red CloudSat track. The middle MODIS track is collocated with CloudSat because it best matches the CloudSat track, as illustrated in Figure 9. The separation distance between each of the collocated

MODIS and CloudSat pixels was calculated. The 1-km resolution MODIS data had pixels most frequently collocated to within 1 km of CloudSat (~80% of all data), with the max distance around 3 km. Approximately 98% of all 1-km resolution MODIS data were collocated to within 2.5 km of the nearest CloudSat pixel. From there, the matched MODIS and CALIPSO data are output to separate files for further filtering for midlevel clouds.

3.2. Filtering midlevel clouds

This study only uses data over the ocean; the CloudSat 2B-GEOPROF navigation-land-sea flag is used to filter for oceanic scenes. The next step in collocation is to identify pixels that only contain midlevel clouds. If all MODIS, CALIPSO, and CloudSat products are available for an individual swath, all variables of interest within each product (see Table 1) are combined into one large file to simplify cloud identification. As stated in the last chapter, for this thesis, clouds are considered midlevel when they have cloud top heights between 4 and 8 km. The cloud top height field in the 2B-GEOPROF-LIDAR data product is used to detect midlevel clouds. All five layers included in CloudSat's 2B-GEOPROF-LIDAR are searched and pixels are flagged when any layer meets the midlevel criteria. If there are any midlevel clouds in the pixel, then it contributes to midlevel cloud occurrence. Although cloud scenes with more than one layer in the midlevel (midlevel clouds over midlevel clouds) are included in this study, these situations only are counted once in total midlevel frequency. It is important to note here that cloud top heights detected by only the radar or only the lidar will be separated in some cases to compare with past studies (e.g. Haynes and Stephens 2007; Riley and Mapes 2009).

All midlevel pixels are then divided into three groups: single-layer midlevel, multi-layer high over midlevel, and multi-layer midlevel over lower-level clouds. The different layered scenes in this study are filtered using the CloudSat 2B-GEOPROF-LIDAR product. Because previous studies have shown that two-layer cloud scenes dominate the multi-layered cloud systems (Wang et al. 2000; Mace 2009; Jin 2012), only single-layer and two-layered scenes are included. The two-layer high over midlevel scenario includes all pixels that have at least one layer of a high cloud (cloud top height greater than 8 km) above a midlevel cloud. The two-layer midlevel over low clouds scenario includes all pixels that have a midlevel cloud layer above lower midlevel clouds or low clouds (cloud top height less than 4 km). The single-layer midlevel scenario includes all pixels containing only one cloud layer with a cloud top height in the midlevel range (between 4 and 8 km).

The three different layered scenarios are then classified as precipitating and non-precipitating using the CloudSat 2C-PRECIP-COLUMN data product. A cloud is considered precipitating in this study when it meets CloudSat's CPR threshold of "rain possible", "rain probable", or "rain certain" in the precipitation flag within the 2C-PRECIP-COLUMN product. Tests were performed to examine the sensitivity of results to these different thresholds; however, the differences between the results for the various precipitating criteria were negligible. Because some rain may not reach the surface, all three thresholds are included to maximize the number of precipitating clouds.

3.3. Phase filtering

MODIS and CALIPSO each retrieve cloud thermodynamic phase, however the two phase detection algorithms differ (Chapter 2) and as a result, the products often do not agree. Single-layer clouds are the only scenes evaluated for properties that depend on phase, including effective radius, optical depth, and liquid or ice water path, because the MODIS retrievals assume single-layered cloud scenes. Effective radius and optical depth retrievals have large errors in multi-layer scenes, and therefore will not be used to ensure cloud properties are only associated with the midlevel clouds. In Table 2 the “CALIPSO filter” signifies the CALIPSO phase classification, just as the “MODIS filter” represents the MODIS phase classification. The agreement column indicates how often instruments coincide. It is evident here that the two instruments disagree on the frequency of ice clouds. CALIPSO detects many more liquid water clouds compared to MODIS. As a result, optical depth, liquid water path, and effective radius retrievals are only used when the CALIPSO and MODIS phases agree. It is necessary that the phases agree since precipitation detection is from CloudSat, whereas the microphysical properties are from MODIS.

These single-layer clouds with matching CALIPSO and MODIS phase classifications will be referred to as the Phase Subset throughout this thesis. However, for midlevel cloud detection, the full dataset (including cloud top heights, thicknesses, and layers) can be used since these variables do not depend on phase. After selecting only the data with phase agreement, clouds are identified as liquid and ice phase 94.7% and 5.3% of the time, respectively. Therefore, in this study there is a possible bias towards liquid water clouds.

3.4. Frequency distributions

Geographical and vertical frequency distributions are determined for midlevel cloud top height (CTH), thickness, temperature (CTT), LWP or IWP, effective radius, optical thickness, and sea surface temperature (SST). The histogram bin widths for each property are shown in Table 3. The joint frequency distributions of different cloud variables (e.g., CTH vs. effective radius) are compared using two-dimensional histograms. Each bin for these joint analyses uses the same bin widths as the vertical frequency distributions in Table 3.

3.5. Environmental properties

Thirty-seven layers from the surface to 9 km from CloudSat's ECMWF-AUX product are used to calculate the mean temperature and humidity environmental profiles. This product includes temperature and specific humidity interpolated to the CloudSat 250 m vertical resolution. Mean profiles for the different cloud layer scenarios and clear scenes are created to compare the environmental profiles. It should be noted here that a scene is considered clear when the 2B-GEOPROF-LIDAR reports zero cloud layers. Also, the midlevel over midlevel profile and midlevel over low-level profile are separated in the evaluation of the environment to see if these two cloud scenes form in different backgrounds.

Our results, which will be further discussed in Chapter 4, show three peaks in midlevel cloud top height frequency. Therefore, mean environmental profiles for each individual peak found in the midlevel (peaks between 5-6 km, 6-6.5 km, and 6.5-7.5 km) are also calculated for comparison.

Other ways of investigating the environmental profiles are also explored because inspection of the mean temperature and specific humidity profiles reveals negligible differences between different midlevel scenes. This occurs because temperature and specific humidity vary greatly in the vertical and because both have large ranges of values in the troposphere (Johnson et al. 1996). Two different ways of examining the environments are used to compare the profiles: (1) mean temperature or specific humidity for all scenes (including clear scenes) subtracted from the given cloud scenario and (2) the derivatives of temperature and specific humidity with respect to height (lapse rate). The latter is only used for single-layer midlevel clouds in each of the three peaks to isolate the factors that could result in higher frequencies of clouds at each height.

In addition to environmental profiles, all midlevel cloud characteristics, including CTH, CTT, optical depth, effective radius, LWP or IWP, are also compared directly to SST by taking the mean of each property for every 1°C of SST.

3.6. Seasonal cycle

One of the goals of this research is to determine midlevel cloud occurrence and seasonal evolution. Spatial distributions are surveyed for our area of interest on a 1.5° x 1.5°latitudinal and longitudinal grid to determine where and how often midlevel clouds occur. Each pixel is binned within the nearest latitude and longitude grid box.

The first spatial distribution examined uses the combination of all four years of data to evaluate the general location of all midlevel clouds. After the full four years is assessed then three months are grouped together to analyze the seasonal cycle: December, January, February (DJF); March, April, May (MAM); June, July, August (JJA); and September, October, November (SON). Seasonal cycles for midlevel cloud amounts are also examined for the three different peaks seen in the midlevel.

Another method for visualizing spatial distributions is used for analyzing the frequency of single-layer precipitating and non-precipitating clouds for the full time period. Spatial distributions for precipitating, non-precipitating, and all single-layer scenes are first created by using the above method for pixel binning. Frequencies are then calculated for precipitating and non-precipitating distributions by dividing each scenario by the all cloud scene. These values are again mapped to the study region to evaluate their distribution.

4. MIDLEVEL CLOUD SCENARIOS

4.1. All midlevel clouds

4.1.1. Midlevel Frequency and Geographic Distribution

Over the four-year study period, roughly 14% of all cloudy scenes within the study region contain midlevel clouds. Of these midlevel cloud scenes, approximately 48% and 24% of them are two-layered and single-layered, respectively. Figure 10 shows the spatial distribution of all single and two-layered midlevel clouds from 2007-2010. Midlevel clouds are concentrated along and just north of the equator, corresponding to the Intertropical Convergence Zone (ITCZ), and to the east of Australia in the South Pacific Convergence Zone (SPCZ). The greatest number of midlevel clouds occurs closer to the maritime continent as a consequence of the Pacific warm pool. These areas of the tropics are known for their enhanced cloud populations due to the warm sea surface temperatures (SSTs), increased moisture, and enhanced low-level convergence (Webster and Lukas 1992).

The areas where midlevel clouds are observed correspond to areas that are known for being convectively active (e.g. Schumacher and Houze 2003; Karlsson et al. 2012) and where deeper convection occurs more frequently. Shallow precipitating convection has previously been found to be most frequent on the outer edges of the deep tropics (Schumacher and Houze 2003, Figure 1) since environmental factors inhibit deep convection. In the deep tropics, convection frequently grows deeper than what is defined as the midlevel here and therefore, the spatial distribution found in this study is likely most influenced by non-precipitating midlevel clouds. It is likely that deep convection triggers the development of the frequent non-precipitating midlevel clouds through detrainment. Detrainment (outflow of cloudy air into the environment, Chapter 1) can produce shelf clouds and limit the growth of clouds by initiating a stable layer in the midlevel (Johnson et al. 1996). However, it is also possible that this shallower convection can precondition the atmosphere by providing moisture for deeper convection in this region (Johnson et al. 1999).

The seasonal cycle of midlevel clouds is shown in Figure 11. It should be noted that December is missing just over a combined month of data from the years 2007 and 2009, so cloud amounts are likely underestimated for DJF. Throughout the annual cycle, midlevel clouds are generally consistent in their location, except for the high concentration seen during JJA (boreal summer) in the Pacific warm pool region. In the boreal summer, the highest SSTs and specific humidities are observed in this region (Webster and Lukas 1992), possibly leading to the enhanced convection. Also during these months, convection is enhanced in the Western North Pacific monsoon region (Briegel and Frank 1997), located in Figure 11 in the area of large midlevel cloud frequencies just north of Papua New Guinea. It should be noted that all months show large concentrations in this warm pool area, however other features such as the ITCZ and SPCZ are just as dominant during DJF, MAM, and SON

4.1.2. Cloud Top Height (CTH) Distribution

CTH is an integral part of this thesis since it is used to define midlevel clouds. The differences between precipitating and non-precipitating clouds are also of primary interest. Figure 12 shows CTH for all (black line), non-precipitating (red dashed line), and precipitating (blue dashed line) midlevel clouds for two-layered and single-layered scenes. This figure shows that non-precipitating clouds are nearly twice as frequent as precipitating clouds at all midlevel heights, driving the features seen in that of “all clouds” (black line). Notice here there are three distinct peaks in midlevel cloud frequency, occurring around 5.5 km, 6.25 km, and 7 km. These peaks, two of which have been found in previous studies by Haynes and Stephens (2007) and Riley and Mapes (2009), are the topic of Chapter 5.

Although non-precipitating midlevel clouds are most frequent in the tropics, precipitating clouds also comprise a significant portion of midlevel cloud totals (Johnson et al. 1999). The colored bars in Figure 13 display the percentage of the total midlevel clouds that are precipitating (blue) and non-precipitating (red) for the three different scene types considered in this thesis (single-layer, midlevel over mid- or low-level clouds, and high over midlevel clouds). High clouds over midlevel clouds dominate this study region, accounting for 65.7% of all two- and single-layered scenes with midlevel clouds (Table 4). Nearly a quarter of all midlevel pixels are single-layer and about 10% are midlevel clouds above other mid- or low-level clouds. Non-precipitating midlevel clouds are more frequent than precipitating clouds, accounting for 73% of all midlevel scenes. Approximately 28% of high over midlevel clouds, 17% of midlevel over mid- or low-level clouds, and 29% of single-layer clouds are considered raining. It is important to note here that the lowest cloud in the midlevel over mid- or low-level cloud scene is precipitating, not the highest cloud located in the midlevel (Stephens and Woods 2007). Because the low cloud is precipitating, these clouds are not considered "midlevel precipitating" in CTH frequency distributions (Figure 12).

Figure 14 shows how the different midlevel cloud layering scenarios contribute to the overall (a) non-precipitating and (b) precipitating CTH distribution. Frequency of the different midlevel cloud scenarios is relative to all single- and two-layer midlevel clouds. It is evident once again that high over midlevel clouds dominate both precipitating and non-precipitating scenes and comprise most of the trimodal distribution seen in Figure 12. To evaluate other characteristics of precipitating and non-precipitating clouds in different midlevel cloud layer scenarios, the following sections are divided into two-layered cloud scenes (Section 4.2) and single-layer cloud scenes (Section 4.3).

4.2. Two-layered midlevel clouds

This section divides the two-layered scenes into two subsections (high over midlevel clouds and midlevel over mid- or lower-level clouds) to investigate the different CTHs and geometric thicknesses of each scenario. Because MODIS cannot accurately retrieve cloud microphysical properties for multi-layer scenes, optical depth, effective radius, and LWP or IWP will only be investigated for single-layer clouds.

4.2.1. High Over Midlevel Clouds

The vertical distributions of precipitating and non-precipitating clouds are examined first. Figure 15 represents the frequency distribution of CTH for non-precipitating (left column, a and c) and precipitating (right column, b and d) high over midlevel clouds relative to the number of pixels in each scenario. The frequency distribution of the highest cloud layer CTH (green line) is basically invariant between the non-precipitating and precipitating scenes (Figure 15a,b), implying that the high cloud does not affect precipitation probability. The most common height of the highest layer occurs around 16 km, corresponding to the height of the tropical tropopause stable layer (Johnson et al. 1999).

High cirrus clouds are most abundant in the tropics because they typically form from decaying deep convection (Luo and Rossow 2004). Therefore, this midlevel cloud scenario (high over midlevel) likely forms in conjunction with deeper convection. The largest variability occurs in the CTH of the lowest layer, which is most obvious in the joint frequency distribution for the two different layers (Figure 15c,d). When the scene is precipitating, there is an obvious shift to higher CTHs compared to non-precipitating clouds. The most frequent pairing for non-precipitating clouds is around 5-5.5 km for the lowest layer and about 16 km for the highest layer. However, the most common precipitating cloud scene has CTH around 5.5-6.5 km for the bottom layer and 16 km for the top layer. The melting layer could be responsible for the increase in non-precipitating clouds around 5-5.5 km, since this is near the 0°C level in the tropics (shown later in the environmental profiles). As ice falls through the melting layer, the environmental air cools (due to latent heating) and stabilizes the air at or just below the 0°C isotherm. This stable layer potentially enhances the detrainment of nearby convective clouds, resulting in the increased frequency of clouds at this level (Johnson et al. 1996; Johnson et al. 1999; Thatcher et al. 2012). Although the melting layer likely inhibits growth of precipitating clouds, the higher CTHs may be a result of these clouds forming in more buoyant environments next to deep convection.

Jin (2012) compared CTHs of two-layer midlevel clouds for the tropics, mid-latitudes, and high-latitudes for three different midlevel definitions. Figure 16 shows an adaptation of Figure 3.2 from Jin (2012). While Jin (2012) defined the midlevel differently (3 km < CTH < 7 km), this figure also shows the characteristics of the midlevel clouds identified in this thesis (4 km < CTH < 8 km). High over midlevel clouds are labeled B in Figure 16. The results from this study in Figure 15c,d for high over midlevel clouds show the basic characteristics of the area labeled B. On Figure 16, there is enhancement (shown in red) when the lowest layer of cloud is between 5-7 km and the highest layer around 16 km. The results found in the present study show more features due to the exclusion of scenes that do not contain midlevel clouds. The features in Jin (2012) of midlevel clouds are washed out because of the large occurrence of high clouds over low-level clouds, shown in purple on Figure 16.

To determine the types of clouds that occur in the midlevel, cloud geometric thickness is evaluated for non-precipitating (Figure 17a,c) and precipitating clouds (Figure 17b,d). For non-precipitating clouds, the lowest cloud layer typically has a thickness of less than 1 km. Although the highest layer has a larger range of thicknesses,

thicknesses of less than 1 km are most frequent here too. This suggests again that thin cirrus or varying anvil thicknesses are responsible for the highest layer in this cloud scene, while thinner, altostratus or altocumulus dominate the lowest layer. The geometric thickness of the highest cloud layer of non-precipitating clouds is very similar to the highest layer of precipitating clouds. The biggest difference between the precipitating and non-precipitating scenes is the thickness of the lowest cloud layer. Precipitating clouds in the lowest layer are substantially thicker than their non-precipitating counterparts. There appears to be a peak in thickness frequency between 5.5-6 km in the lowest layer in these scenes, possibly representing cumulus congestus clouds that extend to the melting layer (Johnson et al. 1999). The most common precipitating midlevel scene in this region consists of cumulus congestus below upper-level clouds that are generally less than 1 km thick (Figure 17d).

Because high over midlevel clouds account for over 65% of all midlevel clouds evaluated in this study, the most common precipitating scene comes from this midlevel scenario. Although the fraction of precipitating clouds is similar for single-layer clouds (~29%) and high over midlevel clouds (~28%), the latter is more frequent and thus represents more of the total precipitation. This result coincides with the Stephens and Wood (2007) study, which showed that a majority of tropical precipitation comes from multi-layer cloud scenes (45-53% of all precipitating profiles) of higher cirrus overlaying cumulus congestus-like convection. One issue with the Stephens and Wood (2007) study is that it used zenith-pointing ground-based millimeter radars at the ARM Manus site and occasional shipborne radar measurements in the Indian Ocean. The results here show that the Stephens and Wood (2007) results may be representative of the broader tropics, especially the TWP region and that even though the shallow mode has been ignored in past studies, it is an important mode in atmospheric heating. While high over midlevel clouds dominate the study region, midlevel clouds also appear over lower level clouds, and thus also contribute to atmospheric heating.

4.2.2. Midlevel Over Mid- or Low-Level Clouds

While the high over midlevel clouds occur much more frequently than midlevel over lower level clouds, the latter mode cannot be discounted, mainly because there is once again evidence in both non-precipitating and precipitating scenarios of the three peaks in CTH frequency in the midlevel (Figures 18a,b). The vertical distribution of CTH for midlevel clouds above mid- or other low-level clouds is illustrated for non-precipitating scenes (Figure 18a,c) and for precipitating scenes (Figure 18b,d). For this scenario, unlike the high over midlevel clouds, both CTHs of the two cloud layers change between precipitating and non-precipitating scenes.

For the highest layer, the three peaks in CTH for all midlevel clouds (Figure 12) are evident in both scenarios. However, the precipitating cloud peak frequencies are slightly shifted upward for the mid and highest peak compared to the non-precipitating clouds. This may be due to an overall more buoyant atmosphere in the precipitating scenes (Esbensen 1978). The lowest cloud layer shows the greatest difference between precipitating and non-precipitating clouds, with precipitating clouds having on average higher CTHs (~2-3 km). The lowest layer in the non-precipitating scenes has CTHs right around 1 km, which corresponds to shallow tropical cumulus clouds (Behrangi et al. 2012). The lowest layer cloud in this scenario has greater vertical extent in precipitating scenes because it is the cloud that is precipitating (Haynes and Stephens 2007). The differences in the height distribution between the two scenes are most obvious between the joint distributions of CTHs for the two layers (Figure 18c,d). In each figure, there is once again evidence for a trimodal distribution in CTH frequency.

Looking again at Figure 16, the Jin (2012) midlevel clouds over lower-level clouds are highlighted in box A. The study here also includes the box to the right of A (directly under B) since midlevel over midlevel clouds are also considered. Most of the lower level CTHs in Jin (2012) are between 1 km and just over 2 km, while the highest CTHs range from 4 km to 7 km. Here again, the results in this study (Figure 18c,d) support the Jin (2012) results. As stated in the previous section, features are more apparent in this research because only scenes with midlevel clouds are included.

As with high over midlevel clouds, geometric thickness is examined for non-precipitating and precipitating midlevel over lower level clouds to evaluate the varying thicknesses between the two layers (Figure 19). Non-precipitating scenes have almost the same thickness frequency distribution for both cloud layers (Figure 19a). Thicknesses are mostly very thin for the lowest layer (CTHs at 1 km), again corresponding to shallow low level cumulus clouds. For precipitating clouds, the lowest layer cloud is much thicker, likely a result of precipitating trade wind cumuli. Trade wind cumulus clouds are a common feature of tropical cloud distributions, accounting for over half of the convective clouds in the tropics (Johnson et al. 1999). This shallow precipitating convection is capped by the trade stable layer near 2 km, the height of most low-level precipitating cloud tops found here (Figure 18b,d). In these precipitating scenes, thin midlevel clouds (< 1 km thick) are typically above these thicker (~ 2 km) low-level clouds (Figure 19d). This shows that the lowest cloud in this midlevel scene is likely the cloud precipitating given its greater thickness than the cloud above it. This matches well with past studies that found that the lowest layer of cloud in multi-layered scenes is typically the cloud that is precipitating (Haynes and Stephens 2007).

4.2.3. Environment of Layered Clouds

Understanding the environmental controls on different midlevel cloud scenes is critical for improving cloud parameterizations in climate models. The average temperature and specific humidity (q) profiles from the ECMWF-AUX product are examined for each of the midlevel cloud scenarios (Figures 20 and 21). Figure 20a shows the atmospheric temperature profile from the surface to 9 km for single-layer clouds, midlevel over low clouds, midlevel over midlevel clouds, high over midlevel clouds, and clear scenes. The average melting layer (0°C isotherm) height for the study domain is indicated near 5 km. As a whole, there are negligible temperature differences between all of these scenarios, including the clear scene. Figure 20b represents the difference between each given layer scenario and all scenes (including clear scenes), reinforcing the small temperature differences between each scenario (vary at most by 1°C). Although the differences in environmental temperatures may not seem significant, a general pattern can be deduced. All scenes have the largest negative anomalies from around 3 km to 7 km, where they are about 0.5-1°C cooler than the average environment. The high over midlevel clouds are the warmest of all scenarios and the only one with a warm anomaly in the lowest 2 km. This could be because these clouds are more frequently observed in the deeper tropics, and thus have warmer SSTs and environmental temperatures. SSTs were examined (not shown) for the various layer scenarios, and high over midlevel clouds did have more frequent warmer SSTs than the other scenes. Single and midlevel over lower clouds tended to be slightly cooler, with midlevel over lower clouds having the highest frequencies of lower SSTs.

While environmental temperature did not vary greatly between the different scenarios, the analysis performed here shows that specific humidity does. Due to the larger differences between different midlevel scenarios, moisture rather than temperature likely has greater influences in the development of different midlevel clouds. This supports a number of studies that have attributed environmental moisture as the main regulator of cloud development and distribution (e.g. Johnson et al. 1996; Takemi et al. 2004). The environmental specific humidity profile shows the differences between the five scenes (Figure 21). Not surprisingly, the clear scene has the driest profile of all scenarios. It is interesting that midlevel over low clouds have the lowest surface specific humidity of the various midlevel clouds scenes even though these clouds occur closest to this level (average heights around 1 km). This is likely due to the clouds forming in areas of cooler SSTs on the outer edges of the deep tropics where trade wind cumulus clouds are more frequent.

Midlevel clouds over midlevel clouds have nearly the same specific humidity as single-layer clouds from the surface up to about 2 km, which is dryer than the high over midlevel clouds (Figure 21b). However, these environments become significantly moister than those of the single-layer clouds, and begin to match the high over midlevel cloud profile around 3.5 km, extending to 9 km. The enhanced moisture of this scenario is observed throughout the midlevel because two clouds form between the levels of 4 km and 8 km. The greatest moisture is consistently seen in the high over midlevel cloud scenario, which is intuitive since the upper levels require greater moisture for cloud development. The environmental background in which high over midlevel clouds form could be a reason why the lower atmosphere also has more moisture than the other scenarios. Again, if these clouds are forming as result of nearby convection, the environment will likely be more moist.

4.3. Single-layer midlevel clouds

Single-layer clouds are a focus of this study because cloud microphysical properties from MODIS can also be evaluated. This section highlights different midlevel cloud characteristics in the following order: geographic frequency, CTH and thickness, optical depth, effective radius, LWP/IWP, and environmental profile and SSTs. Table 5 shows the mean, median, and standard deviation of CTH and geometric thickness for the full dataset (i.e., not subset by phase). Table 6 lists the MODIS retrievals used in the Phase Subset to evaluate optical depth, effective radius, and

LWP/IWP. These two tables are used throughout this section to highlight the differences between thermodynamic phase and precipitating and non-precipitating clouds.

4.3.1. Geographic Frequency Distribution

Non-precipitating single-layer clouds are much more frequent than precipitating single-layer clouds, accounting for approximately 70% of all single-layer scenes. Figure 22 shows the geographic frequency of (a) precipitating and (b) non-precipitating clouds relative to the total number of single-layer clouds for all four years of data. Although non-precipitating clouds are found in all areas of the study region, there is a greater frequency of precipitating clouds along the most northern edges of the domain. There also seems to be enhancement of precipitating clouds to the very southeast of the region, just east of the SPCZ.

The single-layer precipitating clouds in the northern part of the area correspond to areas where single-layer clouds are more dominant than multi-layer cloud systems (Figure 22). Figure 23, adapted from Jin (2012, Figure 2.1), shows that the precipitating clouds in this study correspond to the enhanced area of single-layer clouds just below 30°N in the TWP. Midlevel single-layer convection is more abundant in this region, while near the equator, multi-layer and deeper convection is more frequent (see Section 4.1.1). Schumacher and Houze (2003) found increased rain accumulations for shallow precipitation in the same locations as this study. They find the precipitation on the northern part of the area because deeper convection is substantially more frequent in the warm pool and ITCZ. The more frequent single-layer precipitation in the southeast of our domain matches the increased rain accumulation observed in Schumacher and Houze (2003, Figure 1) between 160-180°E south of the equator, corresponding to the eastern edge of the SPCZ. Figures 22 and 23 show that single-layer midlevel precipitating clouds are more frequent along the northern and southeastern edges of the study domain, supporting the idea that isolated, shallow convection probably consists of cumulus congestus in these areas (Schumacher and Houze, 2003).

Non-precipitating midlevel clouds occur much more frequently in the TWP compared to precipitating clouds, especially in the deep tropics. This means that geometrically thinner, midlevel clouds are more likely to form around deep convective systems (since these are the most common around the equatorial TWP). As a result of these clouds forming around deeper convection, non-precipitating clouds are most likely produced from detraining cloudy air.

4.3.2. CTH and Geometric Thickness

The vertical frequency distribution of single-layer CTH (Figure 24a) closely resembles the CTH distribution in Figure 12 for total midlevel clouds. Figure 24a represents the fraction of either precipitating, non-precipitating, or all single-layer clouds relative to each scenario, whereas Figure 12 represents fraction of each scene relative to all single and two-layer scenes (i.e. each scenario divided by the sum of all single and two-layer clouds). Figure 24a also shows evidence of three peaks (5.5 km, 6.25 km, and 7 km) in midlevel cloud frequency for all single-layer clouds (black line). It is most distinct for non-precipitating clouds (red line); however, there is still enhancement of the peaks at these levels for precipitating clouds (blue line). There are a greater number of precipitating clouds towards the lower end of the midlevel, but these clouds are most likely the tops of low-level trade wind cumulus clouds (see Figure 2). As mentioned previously, trade wind cumulus clouds are the most prevalent form of convection in the tropics. However, these clouds could also be transient cumulus congestus clouds, meaning they are still growing convection. Luo et al. (2009) found that approximately 30-40% of cumulus congestus detected by CloudSat are considered "transient" and will grow to greater altitude at a later time.

Cloud geometric thickness, Figure 24b, is shown for each scenario relative to either total precipitating, non-precipitating, or all single-layer clouds, respectively. Precipitating clouds are significantly thicker, on average, ranging from 3-7.5 km (average of 5.2 km), whereas the average thickness for non-precipitating clouds is 1.6 km (see Table 5). In fact, approximately 73% of non-precipitating clouds are less than 2 km thick, corresponding to more altostratus or altocumulus-like clouds. A peak near 5.5 km is observed in all three scenarios, resulting from a higher population of midlevel clouds at this height, likely due to the melting level limiting cloud vertical growth. The non-precipitating scene correlates well with Riihimaki et al. (2012) who found that 70% of all midlevel clouds at the Darwin ARM site were less than 2 km thick. However, Riihimaki et al. (2012) investigated thickness of all midlevel clouds and did not separate the midlevel into precipitating and non-precipitating scenes. The signal from thicker precipitating clouds was therefore masked in their results since non-precipitating clouds are much more frequent (~70% of all single-layer clouds). Combining all single and two-layer precipitating and non-precipitating clouds in this study results in 55% of all midlevel clouds with thicknesses less than 2 km. Although this does not vary much from Riihimaki et al. (2012), it is likely their single location experienced fewer precipitating clouds since they found more frequent thinner clouds.

4.3.3. Optical Depth

Cloud optical depth is the measure of how much radiation is either scattered or absorbed when passing through a cloud. It is related to cloud particle sizes and concentrations, such that clouds with larger and greater numbers of cloud particles will have higher optical depths (Stephens 1978). Figure 25 shows the frequency distribution of optical depth for liquid clouds (upper panel) and ice clouds (lower panel) for both precipitating and non-precipitating scenarios. Note here that cloud phase (ice or liquid) and optical depth are retrieved by MODIS, while the precipitation flag is from CloudSat. This analysis shows that optical depth correlates well with geometric thickness. Although optical depth also depends on particle size, in general, the geometrically thicker clouds have greater optical depths. Therefore, it is intuitive that precipitating clouds will have much larger optical depths since they are, on average, three times as geometrically thick as non-precipitating clouds. For both cloud thermodynamic phases, precipitating clouds frequently have larger optical depths than non-precipitating clouds. Also, overall, ice clouds have much higher optical depths in this study region than liquid clouds. The average optical depth for precipitating liquid and ice clouds is 18 and 21 compared to non-precipitating averages of 6 and 13, respectively (Table 6).

These distributions can have substantial impacts on the energy budget, affecting both incoming and outgoing radiation since optical depths range from near 0 to over 40. Large optical depths, which generally correspond to geometrically thicker clouds, reduce both outgoing longwave radiation and incoming solar radiation (Ramanathan et al. 1989). Other studies have shown that altostratus and altocumulus clouds, which have smaller optical depths, can have a substantial impact on both global surface shortwave and longwave radiative fluxes (Chen et al. 2000). Since all of these clouds are observed in this study, their influence on the radiation budget is likely significant. Future studies should focus on how various midlevel clouds affect top of atmosphere radiative fluxes.

4.3.4. Liquid and Ice Effective Radius

Effective radius is a weighted average of cloud particle size distribution. It is a quantity that is retrieved by the MODIS instrument using the dual reflectance technique (Nakajima and King 1990) introduced in Chapter 3. Figure 26 shows that effective radius varies greatly between precipitating and non-precipitating clouds for both liquid and ice phase. However, in both phases, precipitating clouds have greater effective radii. Effective radius for liquid clouds is plotted against CTT to analyze the presence of supercooled water and the vertical distribution (Figure 27). The non-precipitating effective radii are concentrated around 15 μm, with the highest frequencies of CTT just above the melting layer up to about -5°C. There is a second area of enhancement around

-12.5°C, which was also found in Riihimaki et al. (2012) for thin midlevel clouds. This temperature also corresponds to the highest peak found in the Riley and Mapes (2009) bimodal distribution. In the precipitating case, the most frequent cloud top effective radii ranges from 20 to 27 μm and are located below just below the 0°C isotherm. Because of the large particles and warm CTTs (i.e. lower CTHs), this area likely represents the frequent precipitating trade wind cumulus clouds mentioned earlier in this chapter. Assuming CALIPSO and MODIS accurately retrieve cloud particle phase, Figure 27 also shows that in both non-precipitating and precipitating clouds, supercooled water is likely frequent at midlevel cloud tops (high fraction of CTT less than 0°C). This agrees with Riihimaki et al. (2012) who found that ~50% of all clouds at -20°C and ~65% of all clouds at -10°C contain supercooled liquid water.

There is a significant portion of this cloud population that has relatively large particles (an average of 16 μm). Rosenfeld and Gutman (1994) suggest a satellite-retrieved effective radius threshold of 15 μm to identify precipitating clouds with tops warmer than about -28°C. However, if their threshold were applied here, nearly 65% of clouds that CloudSat identifies as non-precipitating would be misclassified. The Rosenfeld and Gutman (1994) threshold was developed using only observations only over Israel, and therefore may not be tropically representative. Past studies (Rosenfeld and Lensky 1998; Ba and Gruber 2001; Jensen et al. 2008) have used this 15-μm threshold to detect precipitating clouds, and therefore likely misclassified clouds. Also, because midlevel clouds occur at temperatures at which mixed-phase clouds are possible, the impacts of the cloud phase retrieval on the cloud particle size retrieval should be considered. The retrieved effective radius will be incorrect if an ice cloud is incorrectly identified as water. Future work should involve testing different measurements (whether ground based or satellite) to confirm that the large non-precipitating liquid effective radii are a true signature and not a MODIS retrieval issue.

4.3.5. LWP/IWP

LWP and IWP represent the vertically integrated atmospheric liquid and ice water content per unit area, given here in gm^{-2}. LWP and IWP are calculated from effective radius and optical depth, and therefore will be proportional to both (Equation 1 and 2, Chapter 2). The frequency distributions of LWP and IWP are shown in Figure 28. The most obvious difference between these two phases is that ice clouds contain much more water than the liquid clouds because the optical depth and effective radius for ice clouds are larger than the liquid phase clouds. Not surprisingly, precipitating clouds contain more water than non-precipitating clouds for both phases. The average LWP for precipitating and non-precipitating clouds is 301 gm^{-2} and 71 gm^{-2}, respectively. For IWP, the averages are 356 gm^{-2} for precipitating clouds and 200 gm^{-2} for non-precipitating clouds (Table 6). LWP and IWP (Figure 27) once again show vast differences between the ice and liquid phase, demonstrating why it is imperative for cloud parameterizations to capture the different phases of these midlevel.

4.3.6. Environment

The environments in which single-layer precipitating and non-precipitating clouds form is evaluated to better understand the underlying mechanisms of tropical convection. Figure 29 shows the (a) average temperature and (b) specific humidity environmental profiles for precipitating and non-precipitating scenes. The temperature difference between single-layer precipitating and non-precipitating clouds (Figure 29a) is even less noticeable than between the various layered clouds (Figure 20a). Like temperature, there is little difference between the specific humidity profiles for single-layer precipitating and non-precipitating clouds (Figure 29b). The average non-precipitating profile actually had a slightly moister profile than the precipitating scenes. Assuming the ECMWF atmospheric profiles truly capture the spatial variability, this difference may be because the thin non-precipitating clouds occur in the moist deep tropics, whereas the precipitating clouds are located in drier environments poleward of this area (Figure 22).

Figure 30 shows the average CTHs for given SSTs. In general, warmer SSTs correspond to higher CTHs for both precipitating and non-precipitating midlevel clouds. This figure shows more variability for midlevel cloud heights than for environmental temperature, suggesting that SSTs likely play an important role in determining cloud populations.

The lack of differences in the environmental profiles suggests that either precipitation onset is not dependent on the environment or the ECMWF model’s spatial scale does not capture the environmental variability important for convection. The former is unlikely since past studies show a positive correlation between water vapor and precipitation (Holloway and Neelin 2009). Because there is greater buoyancy in precipitating scenes, the small differences between the varying scenarios are most likely the result of these clouds being on a smaller spatial or temporal scale than the ECMWF model. Yue et al. (2011) point out that the physics of the ECMWF model could also be the cause of some errors in vertical profiles, however this issue still needs further investigation.

5. TRIMODAL DISTRIBUTION OF MIDLEVEL CLOUDS

5.1. Frequency of each peak

In the previous chapter, three distinct peaks in the frequency of midlevel CTH were evident for all cloud scenarios (Figures 12, 15a,b, 18a,b, 24a). These three peaks occur between 5-6 km (low peak), 6-6.5 km (mid peak), and 6.5-7.5 km (high peak) and account for over 62% of all midlevel clouds. Non-precipitating clouds occur more often and are the main constituents of these peaks, however there are also small peaks in the precipitating cloud distribution. Out of all single and two-layered midlevel cloud scenes, 26% have CTHs in the low peak, 12% in the mid peak, and 24% in the high peak (Table 7). Table 7 shows the frequency of each peak and the thicknesses associated with each precipitating or non-precipitating scenario. All three modes have similar precipitating and non-precipitating cloud frequencies; however, since the low peak is most frequent there are more precipitating clouds at this level.

Geometric thickness of single-layered clouds is evaluated for each different peak to determine which cloud populations are most frequent in each peak in Figure 31. The frequency distribution of geometric thickness for each peak in single-layered clouds is shown in Figure 31a. Figure 31b separates them into precipitating and non-precipitating frequency. The average thickness for precipitating clouds in the low, mid, and high peak is 4.8 km, 5.6 km, and 6.3 km, respectively. For non-precipitating clouds in the peaks, average thicknesses are 1.2 km, 1.6 km, and 1.9 km (see Table 7). Different cloud types may be responsible for the varying non-precipitating peak thicknesses. Sassen and Wang (2012) found that altostratus clouds are typically geometrically thicker and ice dominated or mixed phase when compared to altocumulus clouds, which are generally geometrically thinner and water-dominated or mixed phase. Both of these clouds are frequently observed in the TWP throughout their two-year study. Their findings suggest that the thicker altostratus clouds likely occur in the highest non-precipitating peak since ice and mixed phase is more likely at this level than the other two peaks. Altocumulus clouds are likely the most frequent cloud in the lowest peak since these clouds are mostly water or mixed phase and the height of the peak is near the melting layer. Frequency distributions of thermodynamic phase are examined for liquid and ice to determine if a certain phase is more apparent in each mode (Figure 32). All three peaks are mostly dominated by water, with only a little ice in the highest peak. More ice may be present, but could be excluded here since MODIS and CALIPSO often do not agree on ice phase.

The greatest overall thickness of each mode corresponds directly to the CTH of each peak; the lower the peak, the lower the thickness of the clouds. The higher frequencies of these large thicknesses in Figure 31 are represented by the sharp increases in the blue (low peak), red (mid peak), and green (high peak) lines after 4 km. These large thicknesses are likely occurring because deep, precipitating clouds are raining to the surface and CloudSat therefore sees the cloud extending to near the surface. These figures show that there are two distinct types of clouds that occur in each one of these peaks. The most common clouds in each of these peaks are thin altostratus or altocumulus-like clouds less than 1 km thick. The second most common type is a cumulus congestus-like cloud, thick and precipitating.

Distributions of the various single-layer cloud properties were also evaluated for each individual peak. Optical depth, effective radius, and LWP/IWP were all examined, however, there were no obvious differences in the distributions of cloud properties associated with each peak. To aid in determining what role the environment may play in the formation of the various peaks, the background environment is evaluated for the clouds comprising each peak.

5.2. Environment

The environment of the different peaks is essential to understanding each mode's development; therefore, the average temperature and specific humidity profiles are evaluated. The average temperature profile is shown for all three peaks, all midlevel clouds, and clear scenes in Figure 33. As with the temperature profile for precipitating and non-precipitating clouds (see Figure 29a), the profiles barely fluctuate between each scenario. This occurs, as stated previously, because of the large range of temperature and specific humidity in the troposphere. Even the clear scene only varies by less than a degree from the cloudy scenes. Figure 33b shows the temperature difference between each cloud scenario and all scenes (including clear scenarios). While there are visible differences in this figure, ΔT still only varies by $\pm 0.5°C$. The largest differences are observed in the vertical temperature gradient (Figure 33c). The vertical temperature gradients' general features reflect the findings of Johnson et al. (1996, Figure 3). Instead of creating one average environmental profile as in Johnson et al. (1996), average vertical gradient profiles are calculated for each peak to emphasize the differences between the three environments. Note here that only single-layer clouds are used to evaluate the different gradients so that the individual peak environment features could be isolated. There is a stable layer around 2 km in all profiles, which represents the trade inversion, and there is a second stable layer occurring around 5 km (0°C stable layer). The strongest 0°C stable layer occurs with the low peak. However, there appears to be layers of increased stability occurring around the CTHs of the other two peaks. In general, the greatest stability at the three peak heights corresponds directly to that given peak. For example, on Figure 33c the high peak (CTH of 7 km) has the greatest stability at 7 km compared to the other two modes. Although the average temperature profile had negligible differences between the three peaks, the vertical gradient shows that there are temperature stable layers in the midlevel for each of these midlevel modes.

Whereas the average temperature profile had small differences, average specific humidity profiles are distinguishable between the three scenarios, especially in the midlevels (Figure 34). As expected, the clear scene is much drier than the cloudy scenes. Specific humidity (q) profiles for all peaks have roughly the same average value from the surface to about 4 km. Above 4km, the three peak profiles diverge, with the low peak corresponding to the lowest midlevel humidity, followed by the mid peak, and with the most upper level moisture associated with the high peak. Figure 34b emphasizes the humidity differences between the midlevel environments for each peak.

Larger specific humidities are observed for higher peaks possibly because the higher clouds provide more moisture to the upper levels of the environment. However, higher clouds may also result from a moister environment in the upper levels. Because the midlevel clouds scenes are “snapshots”, time variations in temperature and humidity cannot be observed. Therefore, it is difficult to determine whether the clouds or the environment is creating the temperature differences or supplying the moisture to the midlevel atmosphere. Thicker clouds in the non-precipitating higher peaks are possibly due to the atmosphere containing more moisture than the lower peaks. The vertical gradient is also examined for specific humidity (Figure 34c). As with temperature there are differences at each peak height for the vertical specific humidity gradient. There are layers of decreased moisture at all three peak heights, 5.5 km, 6.25 km, and 7 km, in the atmosphere, which again, corresponds directly to the peak profile seen at that level. The differences between these three modes are greater in the specific humidity gradients than the temperature gradients, implying again that moisture most likely controls midlevel environments.

Temperature and specific humidity profiles were also examined for precipitating and non-precipitating clouds (not shown), however differences between the profiles were negligible, similar to the single-layer clouds in Figure 29.

5.3. Seasonal cycle

The seasonal cycle is examined for each different mode in the trimodal distribution to see if the individual peaks occur more frequently in a certain time of the year. The seasonal cycle relative to the annual frequency of clouds for each of the three different peaks is shown in Figure 35. Panels a-c represent the different cloud layer scenarios, with Figure 35d showing all single and two-layer midlevel cloud scenes. Clouds associated with each peak in the single-layer and midlevel over low cloud scenes have greater frequencies between the months of May through October, corresponding to all midlevel cloud frequency (see Chapter 4.1). Once again, it should be noted here that there was limited CloudSat data during December of 2007 and 2009, and therefore, the DJF cloud frequency is likely underestimated for all cloud scenarios. For all single and two-layer scenes (Figure 35d), the peak frequencies most resemble the high over midlevel cloud scenario (Figure 35b) since these clouds dominate the frequency distribution in the study region.

A trimodal distribution in CTH frequency is found here, however, past studies have only ever recognized a bimodal distribution. Reexamining past studies will help differentiate between the various studies and the one performed here to help determine if the third peak in midlevel CTH frequency is a robust feature.

5.4. Past studies

In past analyses (Haynes and Stephens 2007; Riley and Mapes 2009; Riihimaki et al. 2012) only two peaks of clouds in the midlevel have been documented. Spatial distributions of the seasonal cycle were created for all three modes (not shown) in this study; however, there was no variability between the CTHs of the peak midlevel cloud frequencies. All three peaks demonstrated the same characteristics, with all most frequent during the boreal summer in the northern hemisphere. Individual years were also examined (not shown) to see if interannual variability might explain why three peaks are observed rather than the two in past studies. During the four-year study period, a strong El Niño (2009) and a strong La Niña (2010) occurred. The year 2007 was deemed a moderate La Niña and 2008 was considered a normal year. Here again, even with the different ENSO periods, in all years there was evidence of three peaks in the midlevel CTH frequency. While the stable layer associated with the melting layer can explain the first peak, which is also the most common peak, the causes for the other two have yet to be determined.

Haynes and Stephens (2007) were the first to notice the dual peaks of the midlevel cloud distribution using the CloudSat 2B-GEOPROF product. They performed their study with early results from the first three months (JJA) of CloudSat data in each individual ocean basin, including the Western Pacific. They found the lowest peak to occur between 5-6 km and the highest peak around 7-8 km (Figure 36), which is just slightly above the highest peak found here (6.5-7.5 km). There is a slight increase of clouds between their two peaks in Figure 36 (Haynes and Stevens 2007, their Figure 4), which may represent the additional peak found in this study.

Riley and Mapes (2009) expanded on the previous study also using the CloudSat 2B-GEOPROF, which does not include information from the CALIPSO lidar. Their study used one year of data (year not specified), spanning over the entire tropical belt (latitude < 20°). They included all ocean and low-level land (< 1 km) scenes in their analysis and, like Haynes and Stephens (2007), found a bimodal distribution of CTHs in the midlevel (one between 5-6 km and the other 7-8 km). The peaks were more prevalent at night and over land, especially the high peak. The possible differences between these two studies and the one presented here could be a result of different observation locations and periods and the use of different satellite instruments (radar vs. the combined lidar-radar instruments).

Dessler et al. (2006) analyzed CTH distributions of all clouds in global tropical latitudes (10°S to 20°N) with the Geoscience Laser Altimeter System (GLAS) onboard the Ice, Cloud, and Land Elevation Satellite (ICESat). While they were not specifically studying the midlevel, their distribution of midlevel clouds is consistent with the results found here. Figure 37 shows the Dessler et al. (2006, Figure 2) vertical distribution of clouds for different scenarios. In all cases, a trimodal distribution of clouds is found. However, the focus of this figure is on the case that most resembles the study here (oceanic tropical scenes), which is highlighted with the red box. There is a peak for thick clouds between 5-6 km, 6-6.5 km, and 6.5-7.5 km. The distributions are constructed using bins of 76.8 m, which is the resolution of the GLAS data. Although other studies have found only two peaks in the midlevel, the third mid peak located in the midlevel should not be discounted until further investigation. The Dessler et al. (2006) results show that this third peak is most likely a real feature, rather than it being noise or a retrieval error. However, observational and retrieval uncertainties could still play a role in the variations in results between the different studies.

To help determine how instrument sensitivities may impact the detection of these peaks, the combined radar and lidar dataset used to detect CTHs in this study is subset into clouds separately identified by each instrument. Figure 38 shows the radar-only and lidar-only midlevel CTH frequency distributions relative to (a) the individual instruments and (b) all combined midlevel single-and two-layer clouds. Figure 38a shows the same peaks as Haynes and Stephens (2007) and Riley and Mapes (2009) for the CloudSat radar-only data (pink line). It also shows the same peaks found in Dessler et al. (2006) for the CTHs detected by the lidar-only (green line). It is obvious from this figure that the CloudSat radar misses the mid midlevel peak altogether and that it is the CALIPSO lidar that detects it. Riley and Mapes (2009) mention that the high peak could possibly be a radar artifact, although it is unlikely since it is observed in independent studies of the midlevel. Figure 38 shows that these peaks are a real feature since the lidar also captures them. The highest and lowest CTH peaks detected by the lidar correspond to the two peaks in the radar CTHs. However, it is important to note that the lidar CTH peaks are slightly lower than the radar, which seems counterintuitive. One possible explanation is that the populations of clouds within the radar-only and lidar-only curves are skewed towards detecting deeper, congestus-like clouds with the radar and thinner, more altostratus or altocumulus-like clouds with the lidar. It is currently unclear why the radar indicates peak frequencies at greater heights compared to the lidar, however an algorithm artifact also cannot be rue out and should be a focus of future study.

6. CONCLUSION

6.1. Summary of results

The goal of this research was to provide a four-year analysis of midlevel precipitating and non-precipitating clouds in the TWP using NASA's A-Train satellite instruments. Collocated MODIS, CALIPSO, and CloudSat data products were used to evaluate the different characteristics and environments of these midlevel clouds. Distributions of various properties such as cloud frequency, height, and thickness were assessed for precipitating and non-precipitating clouds in single and two layer midlevel cloud scenarios. The two-layer scenarios were divided into high over midlevel clouds and midlevel clouds over mid- or low-level clouds. Temperature and specific humidity profiles were also investigated for all cloud layers. Microphysical properties such as optical depth, effective radius, and LWP/IWP were only examined for single-layer midlevel clouds due to the limitations of the passive MODIS instrument.

In this study, approximately 14% of all clouds in the TWP were considered midlevel (4 km < CTH < 8 km). They are concentrated mainly in the Pacific warm pool region, however there is also enhancement in the convergences zones located within the TWP (ITCZ and SPCZ). Midlevel clouds follow a seasonal cycle, being most numerous between May and October. This correlates well with other convection, resulting from higher SSTs and enhanced low-level convergence during these months (Mitchell and Wallace 1992).

Midlevel clouds most frequently occur in two-layer clouds scenes in the tropics (~50% of all midlevel scenes), with the most common cloud scene of thin cirrus above midlevel clouds (~65% of all clouds evaluated in this study). The most common precipitating scenario of the tropics was cumulus congestus under high clouds. Typically the congestus clouds are found under thin cirrus clouds, but clouds under thicker anvils from nearby deep convection are also observed. Midlevel clouds over lower level clouds occur least often in the tropics, however they still account for approximately 10% of all midlevel scenes. Thin midlevel clouds can exist over precipitating trade wind cumulus clouds, although not frequently in this area (< 2% of all midlevel scenes). The distributions of these clouds correspond to past ground-based studies at the ARM Manus site, thereby expanding their results to the greater tropics rather than just a point location (Stephens and Wood 2007). In this study 55% of all midlevel clouds were less than 2 km thick, whereas Riihimaki et al. (2012) found 70% of midlevel clouds were less than 2 km thick. It is most likely that the ARM Darwin site experiences fewer precipitating clouds than the broader tropics, in general. Therefore, their study may not be entirely representative of the greater TWP. This research also shows more features of the midlevel, such as the trimodal distribution of CTHs, than past global analyses (Jin 2012) since this study focuses on a smaller region.

Single-layer clouds are important to midlevel climatology since they account for nearly a quarter of all midlevel clouds and over a quarter of all midlevel precipitating scenes. These precipitating clouds are concentrated on the outer regions of the deep tropics, corresponding to the Schumacher and Houze (2003) areas of shallow convection. This study supports the Schumacher and Houze (2003) idea that isolated shallow convection probably consists of cumulus congestus clouds in these areas. Non-precipitating single-layer clouds are substantially more frequent than precipitating clouds, and occur throughout the deep tropics, most likely forming as a result of detrainment from deep convection. On average, precipitating clouds have higher optical depths, effective radii, and LWP/IWP than non-precipitating clouds. Although these results were intuitive, they supported the use of collocated MODIS, CALIPSO, and CloudSat independent datasets. One unexpected result is that a large fraction of the non-precipitating liquid clouds had effective radii larger than the 15-μm threshold used to detect precipitating clouds (Rosenfeld and Gutman 1994). Although these differences could be attributed to the location of the study and because only oceanic tropical scenes were assessed, further evaluations are necessary to verify these results.

Three peaks of increased frequency in CTH were found between 5-6 km, 6-6.5 km, and 6.5-7.5 km in all cloud scenarios. Non-precipitating clouds occur in the TWP more frequently than precipitating clouds and are the main contributors to these peaks. All three modes consist mainly of liquid water clouds, with only a small fraction of ice clouds in the uppermost peak. There appears to be two distinct types of clouds that form in each one of these modes. The most frequent clouds that dominate each peak are non-precipitating, thin altostratus or altocumulus-like clouds less than 1 km thick. The second type are precipitating, cumulus congestus-like clouds with large thicknesses. Multiple tests were performed for each peak to assess the spatial and temporal variability to attempt to determine possible formation mechanisms. Unfortunately environmental profile, geographic location, seasonal variation, and interannual variability analyses were all inconclusive.

The bimodal distribution was observed in the CloudSat radar only data, corresponding directly to the two peaks found in Haynes and Stephens (2007) and Riley and Mapes (2009). These two peaks were also detected with the lidar and are mostly identified as water, providing evidence against the Riley and Mapes (2009) idea that the upper peak is a result of radar brightening due to large ice crystals dominating radar reflectivity. Although these previous studies have shown only two peaks in the midlevel CTH frequency, the results here and those of Dessler et al. (2006) suggest the third peak located around 6.25 km in the midlevel cannot be discounted until further investigation. It is important to note that the lidar detects more frequent clouds at lower heights than the radar, which is counterintuitive since the lidar should detect thinner clouds before the radar. This could be an algorithm artifact or a function of the distribution of clouds within the subsampled populations, however it is unclear at this time and should be a focus of future study.

Average temperature and specific humidity profiles were also evaluated in this study. Profiles for all layer scenarios (single-layer versus different two-layer scenes), clear scenes, single-layer precipitating versus non-precipitating, and the three peaks were among the scenes examined. In general, temperature did not provide substantial information on the environment in which these clouds form since there were negligible differences between all scenarios evaluated. While temperature did not vary much between the scenes, specific humidity analysis showed large differences. For all various cloud scenes, the average specific humidity at every level is greater than clear scenes. On average, higher clouds are associated with a moister profile. This is especially true for the three different peak levels. Analysis of the three peaks showed that specific humidity differences between each scene are greatest at midlevels from 5 km to 9 km. The moistest profile in the midlevel coincided with the high peak. The other two peaks had lower specific humidities, with the lowest peak being the driest.

For the midlevel peaks, vertical gradients of temperature and specific humidity were also examined. Evaluation of these two gradients showed stable and drier layers at approximately the same height as each of the cloud top peaks. Even though there were apparent differences in the temperature gradient, specific humidity once again had greater variances between the three profiles. Because of the greater variability, moisture rather than temperature may control the development of different midlevel modes. Again, this supports past studies that found that environmental moisture plays a larger role than temperature stable layers in determining cloud vertical development (e.g. Takemi et al. 2004).

The temperature and specific humidity between the precipitating and non-precipitating clouds showed little variation. In fact, moister profiles were observed for non-precipitating scenes. This may be because the study region is large, resulting in significant averaging. As seen in the precipitating cloud distribution, these clouds tend to occur in the northern part of the area, perhaps also contributing to the drier environmental profile. However, it is also likely that the ECMWF model does not capture the spatial or temporal scale of environmental variability important for convection since this study is evaluated on a pixel-by-pixel basis. A more accurate evaluation of the environment should be the focus of future study.

6.2. Future work

This thesis focused on midlevel clouds only in the TWP. Future studies should expand the observation area to include the entire tropical belt (all latitudes < 20°) to determine the representativeness of these results. As mentioned in previous sections, future improvements to this study should focus on the validity of the MODIS effective radius measurements to confirm the results found here. If the large non-precipitating effective radii are in fact a real feature, then the 15-μm threshold for precipitation would not be universally applicable. This implies that past studies that use this threshold to identify precipitating clouds may include many non-precipitating clouds in their analyses. Also, further investigation of the midlevel trimodal distribution is necessary to understand midlevel dynamics. Future studies should focus on the mechanisms behind the mid and high peaks observed in the midlevel CTH frequency. As discussed by Riley and Mapes (2009), detrainment from nearby deep convection could be one reason the enhanced populations of midlevel clouds are observed at the different peaks heights. Detrainment from convection may cause the stable layers observed in the environmental profiles, however confirmation from *in situ* measurements (preferably in several locations across the TWP) would be useful since the 2B-GEOPROF-LIDAR only provides a snapshot of the cloud scenes. And finally, future studies should compare these results with the environmental profiles measured from AIRS. It is likely that the CloudSat ECMWF-AUX cannot capture the scale of variability important for the clouds identified this study. AIRS would provide more accurate measurements since it is an atmospheric sounder located in the same satellite orbit as CloudSat, CALIPSO, and MODIS.

REFERENCES

Ackerman, S. A., K. I. Strabala, W. P. Menzel, R. A. Frey, C. C. Moeller, and L. E. Gumley, 1998: Discriminating clear sky from clouds with MODIS. *J. Geophys. Res.,* **103,** 32141–32157.

Ansmann, A., et al., 2009: Evolution of the ice phase in tropical altocumulus: SAMUM lidar observations over Cape Verde. *J. Geophys. Res.,* **114,** D17208, doi: 10.1029/2008JD011659.

Ba, M. B. and A. Gruber, 2001: GOES multispectral rainfall algorithm. *J. Appl. Meteor.,* **40,** 1500-1514.

Behrangi, A., T. Kubar, B. Lambrigtsen, 2012: Phenomenological Description of Tropical Clouds Using CloudSat Cloud Classification. *Mon. Wea. Rev.*, **140**, 3235–3249.

Benedict, J. J. and D. A. Randall, 2007: Observed characteristics of the MJO relative to maximum rainfall. *J. Atmos. Sci.,* **64,** 2332-2354.

Bodas-Salcedo, A., M. J. Webb, M. E. Brooks, M. A. Ringer, K. D. Williams, S. F. Milton, and D. R. Wilson, 2008: Evaluating cloud systems in the Met Office global forecast model using simulated CloudSat radar reflectivities. *J. Geophys. Res.,* **113,** D00A13, doi:10.1029/2007JD009620.

Briegel, L. M., W. M. Frank, 1997: Large-scale influences on tropical cyclogenesis in the western North Pacific. *Mon. Wea. Rev.,* **125,** 1397-1413.

Chen, T., W. B. Rossow, Y. Zhang, 2000: Radiative effects of cloud-type variations. *J. Climate*, **13**, 264–286.

Chen, Y. and A. D. Del Genio, 2009: Evaluation of tropical cloud regimes in observations and a general circulation model. *Clim. Dynam.,* **32,** 355-369, doi:10.1007/s00382-008-0386-6.

Demott, C. A., D. A. Randall, M. Khairoutdinov, 2006: Convective precipitation variability as a tool for general circulation model analysis. *J. Climate,* **20,** 91-112.

Del Genio, A. D., Y. Chen, D. Kim, and M. Yao, 2012: The MJO Transition from Shallow to Deep Convection in CloudSat/CALIPSO Data and GISS GCM Simulations. *J. Climate*, **25**, 3755–3770.

Divakarla, M., G. C. D. Barnet, M. D. Goldberg, L. M. McMillin, E. Maddy, L. Z. W. Wolf, and X. Liu, 2006: Validation of atmospheric infrared sounder temperature and water vapor retrievals with matched radiosonde measurements and forecasts. *J. Geophys. Res.,* **111,** D09S15, doi:10.1029/2005JD006116.

Esbensen, S., 1978: Bulk Thermodynamic Effects and Properties of Small Tropical Cumuli. *J. Atmos. Sci.*, **35**, 826–837.

Field, P. R., 1999: Aircraft observations of ice crystal evolution in an altostratus cloud. *J. Atmos. Sci.,* **56,** 1925-1941.

Frey, R. A., S. A. Ackerman, Y. Liu, K. I. Strabala, H. Zhang, J. R. Key, and X. Wang, 2008: Cloud detection with MODIS. Part 1: improvements in the MODIS cloud mask for collection 5. *J. Atmos. and Ocean Tech.,* **25,** 1067-1072.

Fleishauer, R. P., V. E. Larson, and T. H. Vonder Haar, 2002: Observed microphysical structure of midlevel, mixed phase clouds. *J. Atmos. Sci.,* **59,** 1779-1804.

Hagos, S., L. Leung, and J. Dudhia, 2011: Thermodynamics of Madden-Julian Oscillation in a regional model with constrained moisture. *J. Atmos. Sci.,* **68,** 1974-1989, doi: 10.1175/2011JAS3592.1.

Hahn, C. J. and S. G. Warren, 1999: Extended edited synoptic cloud reports from ships and land stations over the globe, 1952-1996. ORNL/CDIAC-123 NDP026C, Carbon Dioxide Information Analysis Center, Oak Ridge National Laboratory, Oak Ridge, TN.

Hahn, C. J. and S. G. Warren, 2003: Cloud climatology for land stations worldwide, 1971–1996. Tech. Rep. NDP-026D, Carbon Dioxide Information Analysis Center, Oak Ridge National Laboratory, Oak Ridge, TN.

Haladay, T. and G. Stephens, 2009: Characteristics of tropical thin cirrus deduced from joint CloudSat and CALIPSO observations. *J. Geophys. Res.,* **114,** D00A25, doi:10.1029/2008JD010675.

Haynes, J. and G. L. Stephens, 2007: Tropical oceanic cloudiness and the incidence of precipitation: Early results from CloudSat. *Geophys. Res. Lett.*, **34,** L09811, doi:10.1029/2007GL029335.

Haynes, J., T. S. L'Ecuyer, G. L. Stephens, C. M. S. D. Miller, N. B. Wood, and S. Tanelli, 2009: Rainfall retrieval over the ocean with spaceborne W-band radar. *J. Geophys. Res.,* **114,** D00A22, doi:10.1029/2008JD009973.

Heymsfield, A. J., L. M. Miloshevich, A. Slingo, K. Sassen, D. Starr, 1991: An observational and theoretical study of highly supercooled altocumulus. *J. Atmos. Sci.,* **48,** 923-945.

Hobbs, P. and A. Rangno, 1985: Ice particle concentrations in clouds. *J. Atmos. Sci.,* **42,** 2523-2549.

Holloway, C. E., J. D. Neelin, 2009: Moisture vertical structure, column water vapor, and tropical deep convection. *J. Atmos. Sci.*, **66**, 1665–1683.

Hu, Y., et al., 2009: CALIPSO/CALIOP cloud phase discrimination algorithm. *J. Atmos. Oceanic Technol.,* **26,** 2293-2309, doi:10.1175/2009JTECHA1280.1.

Inness, P., J. Slingo, S. Wollnough, R. Neale, and V. Pope, 2001: Organization of tropical convection in a GCM with varying vertical resolution; implications for the simulation of the Madden-Julian Oscillation. *Clim. Dyn.,* **17,** 777-793.

Jensen, M. P., A. M. Vogelmann, W. D. Collins, G. J. Zhang, E. P. Luke, 2008: Investigation of regional and seasonal variations in marine boundary layer cloud properties from MODIS observations. *J. Climate*, **21,** 4955–4973.

Jin, H., 2012: Satellite remote sensing of mid-level clouds. Ph.D. dissertation, Texas A&M University, 174 pp.

Johnson, R. H., P. Ciesielski, and K. Hart, 1996: Tropical inversions near the 0°C level. *J. Atmos. Sci.,* **53,** 1838-1855.

Johnson, R. H., T. M. Rickenbach, S. A. Rutledge, P. E. Ciesielski, W. H. Schubert, 1999: Trimodal Characteristics of Tropical Convection. *J. Climate*, **12,** 2397–2418.

Karlsson, K. G., Riihelä, A., Müller, R., Meirink, J. F., Sedlar, J., Stengel, M., Lockhoff, M., Trentmann, J., Kaspar, F., Hollmann, R., Wolters, E., 2012: CLARA-A1: CM SAF clouds, albedo and radiation dataset from AVHRR data - Edition 1 - monthly means/daily means/pentad means/monthly histograms. Satellite Application Facility on Climate Monitoring. doi:10.5676/EUM_SAF_CM/CLARA_AVHRR/V001.

Kikuchi, K., and Y. N. Takayabu, 2004: The development of organized convection associated with the MJO during TOGA COARE IOP: trimodal characteristics. *J. Geophys. Res.,* **31**, L10101, doi:10.1029/2004GL019601.

King, M. D., S. C. Tsay, S. E. Platnick, M. Wang, and K. N. Liou, 1997: Cloud retrieval algorithms for MODIS: optical thickness, effective particle radius, and thermodynamic phase. MODIS Algorithm Theoretical Basis Doc. ATBD-MOD-05, MOD06-Cloud product, 83 pp.

LeMone, M. A. and R. J. Meitin, 1984: Three examples of fair-weather mesoscale boundary-layer convection in the tropics. *Mon. Weather Rev.,* **112,** 1985-1997.

Lensky, I. M. and D. Rosenfeld, 1997: Estimation of precipitating area and rain intensity based on the microphysical properties retrieved from NOAA AVHRR data. *J. Appl. Meteor.,* **36,** 234-242.

Lensky, I. M. and D. Rosenfeld, 2003: Satellite-based insights into precipitation formation processes in continental and maritime convective clouds at nighttime. *J. Appl. Meteor.,* **42,** 1227-1233.

Le Treut, H., X. Li, and M. Forichon, 1994: Sensitivity of the LMD general circulation model to greenhouse forcing associated with two different cloud water parameterizations. *J. Climate*, **7,** 1827-1841.

Luo, Z. and W. B. Rossow, 2004: Characterizing tropical cirrus life cycle, evolution, and interaction with upper-tropopsheric water vapor using lagrangian trajectory analysis of satellite observations. *J. Climate,* **17,** 4541-4563.

Mace, G. G., S. Benson, and S. Kato, 2006: Cloud radiative forcing at the Atmospheric Radiation Measurement Program Climate Research Facility: 2. Vertical redistribution of radiant energy by clouds. *J. Geophys. Res.,* **111,** D11S91, doi:10.1029/2005JD005922.

Mace, G. G., R. Marchand, Q. Zhang, and G. Stephens, 2007: Global hydrometeor occurrence as observed by CloudSat: initial observations from summer 2006. *Geophys Res. Lett.,* doi:10.1029/2006GL029017.

Mace, G. G., Q. Zhang, M. Vaughn, R. Marchand, G. Stephens, C. Trepte, and D. Winker, 2008: A description of hydrometeor layer occurrence statistics derived from the first year of merged CloudSat and CALIPSO data. *J. Geophys. Res*., **114,** D00A26, doi:10.1029/2007JD009755.

Mace, G. G., Q. Zhang, M. Vaughan, R. Marchand, G. Stephens, C. Trepte, and D. Winker, 2009: A description of hydrometer layer occurrence statistics derived from the first year of merged CloudSat and CALIPSO data. *J. Geophys. Res.,* **114,** D00A26, doi:10.1029/2007JD009755.

Marchand, R., G. G. Mace, T. Ackerman, and G. Stephens, 2008: Hydrometer detection using CloudSat-an earth-orbiting 94-GHz cloud radar. *J. Atmos. Oceanic. Technol.,* **25,** 519-533.

Mapes, B. and P. Zuidema, 1996: Radiative-dynamical consequences of dry tongues in the tropical atmosphere. *J. Atmos. Sci.,* **53,** 620-638.

Mapes, B., S. Tulich, J. Lin, and P. Zuidema, 2006: The mesoscale convection life cycle: building block or prototypes for large-scale tropical waves? *Dynam. Atmos. Oceans,* **42,** 3-29, doi:10.1016/j.dynatmoce.2006.03.003

Minnis, P., Sun-Mack, S., Chen, Y., Khaiyer, M. M., Yi, Y., Ayers, J. K., Brown, R. R., Dong, X., Gibson, S. C., Heck, P. W., Lin, B., Nordeen, M. L., Nguyen, L., Palikonda, R., Smith Jr., W. L., Spangenberg, D. A., Trepte, Q. Z., Xi, B., 2011: CERES edition-2 cloud property retrievals using TRMM VIRS and Terra and Aqua MODIS data, part II: examples of average results and comparisons with other data. *IEEE Trans. Geosci. Remote Sens.,* **49 (11),** 4401–4430.

Mitchell, T. P., J. M. Wallace, 1992: The annual cycle in equatorial convection and sea surface temperature. *J. Climate*, **5,** 1140–1156

Nakajima, T., and M. D. King, 1990: Determination of the optical thickness and effective radius of clouds from reflected solar radiation measurements. Part I: theory. *J. Atmos Sci.,* **47,** 1878-1893.

Nam, C. C. W. and J. Quaas, 2012: Evaluation of Clouds and Precipitation in the ECHAM5 General Circulation Model Using CALIPSO and CloudSat Satellite Data. *J. Climate*, **25**, 4975–4992.

Plantick, S., M. D. King, S. A. Ackerman, W. P. Menzel, B. A. Baum, J. C. Riedi, and R. A. Frey, 2003: The MODIS cloud products: algorithms and examples from TERRA. *IEEE Trans. Geos. And Remote Sensing*, **41 (2),** 459-473.

Poore, K., J. H. Wang, and W. B. Rossow, 1995: Cloud layer thicknesses from a combination of surface and upper-air observations. *J. Climate,* **8,** 550-568.

Powell, K., M. Vaughan, D. Winker, K. P. Lee, M. Pitts, C. Trepte, P. Detweiler, W. Hunt, J. Lambeth, P. Lucker, T. Murray, O. Hagolle, A. Lifermann, M. Faivre, A. Garnier, J. Pelon, 2010: Cloud-Aerosol LIDAR Infrared Pathfinder Satellite Observations. Data Management System Data Products Catalog, 106 pp.

Ramanathan, V., R. D. Cess, E. F. Harrison et al., 1989: Cloud-radiative forcing and climate: results from the earth radiation budget experiment. *Science*, **243,** 57–63.

Randall, D. A. and G. J. Huffman, 1982: Entrainment and detrainment in simple cumulus cloud model. *J. Atmo. Sci.*, **39,** 2793-2805.

Riihimaki, L. D., S. A. McFarlane, J. M. Comstock, 2012: Climatology and formation of tropical midlevel clouds at the Darwin ARM site. *J. Climate*, **25,** 6835–6850.

Riley, E. M. and B. E. Mapes, 2009: Unexpected peak near -15°C in CloudSat echo top climatology. *J. Geophs. Res.,* **36,** L09819, doi: 10.1029/2009GL037558.

Riley, E. M., B. E. Mapes, and S. N. Tulich, 2011: Clouds associated with the Madden-Julian Oscillation: a new perspective from CloudSat. *J. Atmo. Sci.,* **68,** 3032-3051.

Rosenfeld, D. and G. Gutman, 1994: Retrieving microphysical properties near the tops of potential rain clouds by multispectral analysis of AVHRR data. *Atmos. Res.,* **34,** 259-283.

Rosenfeld, D. and I. Lensky, 1998: Satellite-based insights into precipitation formation processes in continental and maritime convective clouds. *Bull. Amer. Meteor. Soc.*, **79,** 2457-2476.

Rossow, W. B. and Y. Zhang, 2010: Evaluation of a Statistical Model of Cloud Vertical Structure using combind CloudSat and CALIPSO cloud layer profiles. *J. Climate,* **23,** 6641-6653.

Sassen, K., 1991: The polarization lidar technique for cloud research: a review and current assessment. *Bull. Amer. Meteor. Soc.,* **72,** 1848-1866.

Sassen, K. and Z. Wang, 2012: The clouds of the middle troposphere: composition, radiative impact, and global distribution. *Surveys in Geophys.,* **33**:3-4, 677-691

Schubert, W. H., P. E. Ciesielski, C. Lu, R. H. Johnson, 1995: Dynamical Adjustment of the Trade Wind Inversion Layer. *J. Atmos. Sci.*, **52**, 2941–2952.

Schumacher, C. and R.A. Houze, 2003: The TRMM precipitation radar's view of shallow, isolated rain. *J. Appl. Meteor.,* **42,** 1519-1524.

Seifert, P., and Coauthors, 2010: Saharan dust and heterogeneous ice formation: Eleven years of cloud observations at a central European EARLINET site. *J. Geophys. Res.*, **115,** D20201, doi:10.1029/2009JD013222.

Stephens, G. L., 1978: Radiation profiles in extended water clouds. I: theory. *J. Atmos Sci.,* **35,** 2111-2122.

Stephens, G. L., D. G. Vane, R. J. Boain, G. G. Mace, K. Sassen, Z. Wang, A. J. Illingworth, E. J. O'Connor, W. B. Rossow, S. L. Durden, S. D. Miller, R. T.

Austin, A. Benedetti, C. Mitrescu, and the CloudSat Science Team, 2002: The CloudSat mission and the A-TRAIN: A new dimension to space-based observations of clouds and precipitation. *Bull. Am. Met. Soc.,* **83,** 1771-1790.

Stephens, G. L., 2005: Cloud feedback in the climate system: a critical review. *J. Climate,* **18,** 237-273.

Stephens, G. L. and N. B. Wood, 2007: Properties of tropical convection observed by millimeter-wave radar systems. *Mon. Weather Rev.,* **125,** 821-842.

Stephens, G. L., et al. 2008: CloudSat mission: performance and early science after the first year of operation. *J. Geophys. Res.,* **113,** D00A18, doi:10.1029/2008JD009982.

Stubenrauch, C. J., A. Chedin, G. Radel, N. Scott, and S. Serrar, 2006: Cloud properties and their seasonal and diurnal variability from TOVS Path-B. *J. Climate*, **19,** 5531–5553.

Sun, Z. and K. P. Shine, 1995: Parameterization of ice clouds radiative properties and its application to potential climatic importance of mixed-phase clouds. *J. Climate,* **9,** 1874-1888.

Takayabu, Y. N., S. Shige, W. K. Tao, and N. Hirota, 2010: Shallow and deep latent heating modes over tropical oceans observed with TRMM PR spectral latent heating data. *J. Climate,* **23,** 2030-2046.

Takemi, T., O. Hirayama, and C. Liu, 2004. Factors responsible for the vertical development of tropical oceanic cumulus convection. *Geophys. Res. Lett.*, **31,** L11109, doi: 10.1029/2004GL020225.

Thatcher, L., Y. N. Takayabu, C. Yokoyama, and Z. Pu, 2012: Characteristics of tropical cyclone precipitation features over the western Pacific warm pool. *J. Geophys. Res.,* **117,** D16208, doi:10.1029/2011JD017351.

Thayer-Calder, K., and D. Randall, 2009: The role of convective moistening in the Madden–Julian oscillation. *J. Atmos. Sci.*, **66,** 3297–3312.

Tromeur, E. and W. B. Rossow, 2010: Interaction of the deep convection with the large scale circulation in the MJO. *J. Climate,* **23,** 1837-1853.

Twomey, S. and T. A. Wojciechowski, 1969: Observations of the Geographical Variation of Cloud Nuclei. *J. Atmos. Sci.*, **26**, 648–651.

Yasunaga, K., and Coauthors, 2006: Melting layer cloud observed during R/V Mirai cruise MR01-K05. *J. Atmos. Sci*., **63,** 3020–3032.

Winker, D. M., J. Pelon, and M. P. McCormick, 2003: The CALIPSO mission: Spaceborne lidar for observation of aerosols and clouds. Lidar Remote Sensing for Industry and Environment Monitoring III, U.N. Singh, T. Itabe, and Z. Lui, Eds., International Society for Optical Engineering (SPIE Proceedings, Vol. 4893), 1–11.

Winker, D. M., M. A. Vaughan, A. Omar, Y. Hu, K. A. Powell, Z. Liu, W. H. Hunt, and S. A. Young, 2009: Overview of the CALIPSO mission and CALIOP data processing algorithms. *J. Atmos. Oceanic Technol.*, **26,** 2310–2323.

Yue, Q., B. H. Kahn, E. J. Fetzer, and J. Teixeira, 2011: Relationship between marine boundary layer clouds and lower tropospheric stability observed by AIRS, CloudSat, and CALIOP. *J. Geophys. Res.*, **116,** D18212, doi:10.1029/2011JD016136.

Wang, J. H., W. B. Rossow, and Y. Zhang, 2000: Cloud vertical structure and its variations from a 20-year global rawinsonde dataset. *J. Climate,* **13,** 3041-3056.

Webster, P. J. and R. Lukas, 1992: TOGA-COARE: the coupled ocean-atmosphere response experiment. *Bull. Amer. Meteor. Soc.,* **73,** 1377-1416.

Zhang, M. H. *et al.,* 2005: Comparing clouds and their seasonal variations in 10 atmospheric general circulation models with satellite measurements. *J. Geophys. Res.,* **110**, D15S02, doi:10.1029/2004JD005021.

Zhang, D., Z. Wang, and D. Liu, 2010: A global view of midlevel liquid-layer topped stratiform cloud distribution and phase partition from CALIPSO and CloudSat measurements, *J. Geophys. Res.*, **115,** D00H13, doi:10.1029/2009JD012143

APPENDIX A

TABLES

Table 1. Satellite instruments and products used in this thesis.

Instrument	**Product**	**Variables**	**Nadir Resolution**
MODIS			
	MAC06S0	Optical depth, effective radius, liquid/ice water path, cloud top temperature, phase	1 km and 5 km horizontal; 1 cloud layer
CALIPSO			
	CAL_LID_L2_01km_Clay	Phase, cloud top/base height	1 km horizontal; Up to 10 cloud layers
CloudSat			
	2B-GEOPROF	Cloud top and base height, radar reflectivity, land/sea flag	2.5 km horizontal; 250 m vertical
	2B-GEOPROF-LIDAR*	Cloud top/base height, cloud layers, geometric thickness	2.5 km horizontal; 250 m vertical
	2C-PRECIP-COLUMN	Rain detection, precipitation flag	2.5 km horizontal; 250 m vertical
	ECMWF-AUX	Temperature/ humidity/ pressure profile	2.5 km horizontal; 250 m vertical

*2B-GEOPROF-LIDAR is a combined CloudSat and CALIPSO product.

Table 2. Different filters for particle phase. Agreement column represents how often the specified instrument agrees with the filter. The red text indicates the poor agreement between MODIS and CALIPSO for the non-precipitating ice phase.

CALIPSO FILTER		**MODIS AGREEMENT**
	Precipitating Liquid	66.5%
	Precipitating Ice	58.0%
	Non-Precipitation Liquid	63.0%
	Non-Precipitation Ice	14.7%
	LIQUID	**64.1%**
	ICE	**33.38%**
MODIS FILTER		**CALIPSO AGREEMENT**
	Precipitating Liquid	89.6%
	Precipitating Ice	26.9%
	Non-Precipitation Liquid	90.4%
	Non-Precipitation Ice	13.2%
	LIQUID	**90.18%**
	ICE	**21.34%**

Table 3. Bin sizes of the various midlevel properties used to create frequency distributions.

Midlevel Characteristic	Bin Size
Cloud Top Height/Thickness	0.25 km
Optical Thickness	2
Effective Radius	1 µm
LWP/IWP	25 g/m^2
Sea Surface Temperature	1°C
Cloud Top Temperature	1°C

Table 4. Each scene divided into fraction of the total midlevel cloud population and fraction of each scene that is precipitating relative to each layer scenario.

Midlevel Cloud Scene	% of Midlevel Clouds	% Precipitating
Single-layer	24.1%	28.5%
High Over Mid	65.7%	27.9%
Mid Over Mid/Low	10.2%	17.2%

Table 5. Full dataset is used for CTH and geometric thickness since precipitating and non-precipitating clouds are only investigated rather than phase.

Cloud Property		Precipitating	Non-Precipitating
CTH (km)*			
	Mean	5.85	6.04
	Median	5.78	6.01
	STD	1.18	1.10
Thickness (km)*			
	Mean	5.17	1.61
	Median	5.05	0.76
	STD	1.17	1.73

Table 6. All variables included in this study for single-layer midlevel clouds. Each column represents the mean, median, and standard deviation for the Phase Subset. (P = precipitating, NP = non-precipitating)

Cloud Property		P-Liquid	NP-Liquid	P-Ice	NP-Ice
Optical Depth					
	Mean	18	6	21	13
	Median	15	4	18	11
	STD	15.4	4.8	15.9	10.7
Effective Radius					
(μm)	Mean	22	16	28	24
	Median	23	16	28	23
	STD	4.7	5.5	7.6	9.5
LWP/IWP					
(gm^{-2})	Mean	301	71	356	200
	Median	249	46	285	161
	STD	250	79	262	180

Table 7. The fraction of each peak relative to all midlevel clouds is represented in the second column. The frequency of precipitation in the three peaks relative to the total amount of clouds in each is also characterized along with the thickness of each scenario.

Peak	**% of all Midlevel Clouds**	**Precipitating**	**Non-Precipitating**	**Avg. Thickness Precip.**	**Avg. Thickness Non-precip.**
Low	26%	25.8%	74.2%	4.8 km	1.2 km
Mid	12%	26.3%	73.7%	5.6 km	1.6 km
High	24%	24.9%	75.1%	6.3 km	1.9 km

APPENDIX B

FIGURES

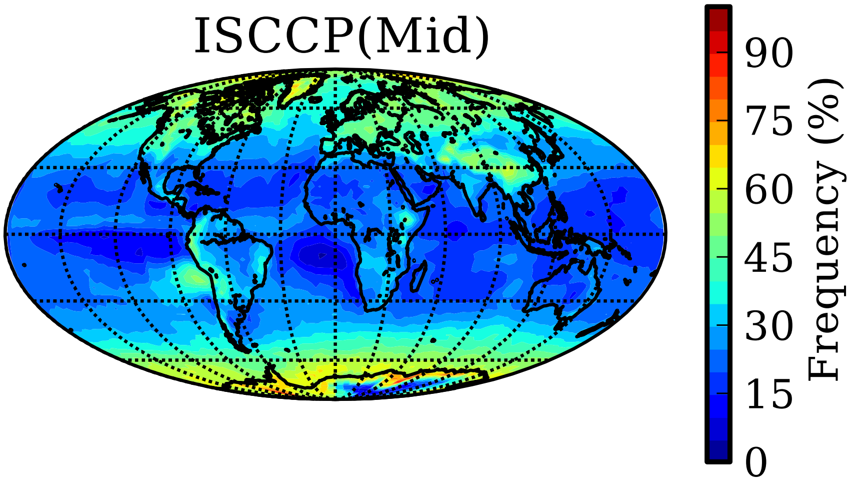

Figure 1. Normalized frequency of ISCCP midlevel cloud amounts. Midlevel defined here as clouds with cloud top pressures between 680 to 440 hPa. Adapted from Jin (2012).

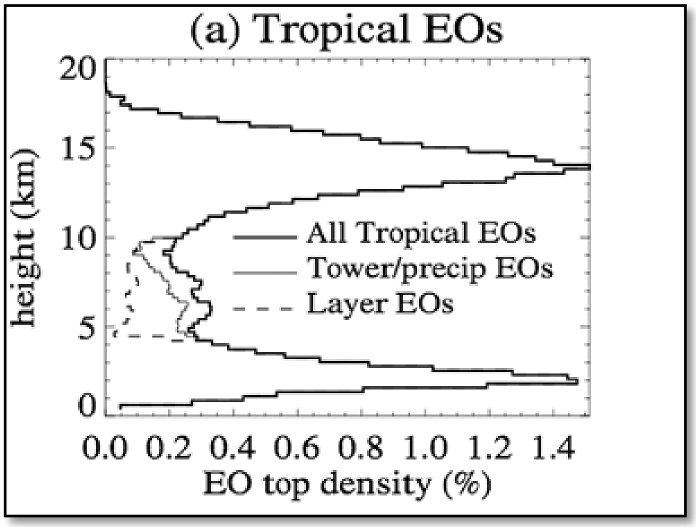

Figure 2. All tropical echo object (EOs) cloud top heights. A midlevel bimodal distribution is evident between 5 and 8 km. Taken from Riley and Mapes (2009).

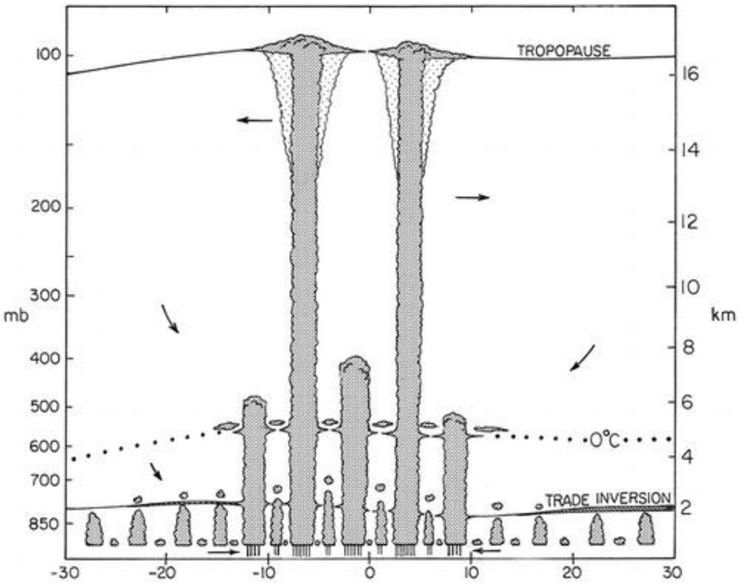

Figure 3. Trimodal distribution of tropical convection. The three types of convection are shown here: low trade wind cumulus capped by the trade wind inversion, midlevel cumulus congestus capped by the 0°C stable layer, and deep convection capped by the tropopause. Taken from Johnson et al. (1999).

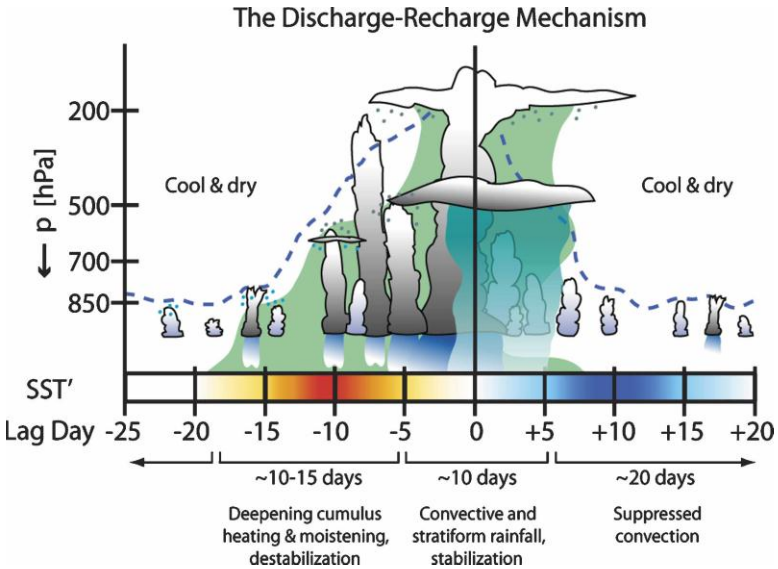

Figure 4. Schematic diagram of the discharge-recharge theorem showing the build up of cumulus congestus clouds, about 10-15 days prior to peak rainfall on day 0. The blue dashed line represents the approximate convective cloud top heights, while the blue dots indicate shallower convective clouds moistening the environment through detrainment. Taken from Benedict and Randall (2007).

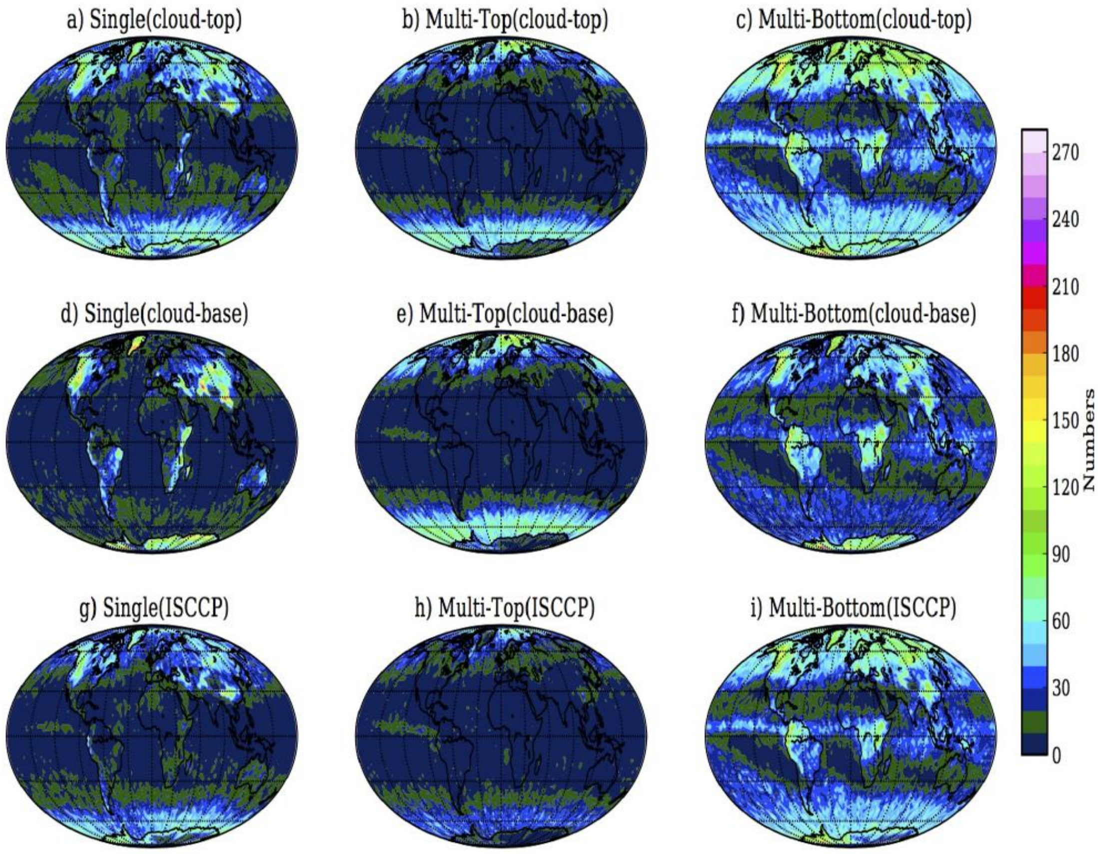

Figure 5. Differences between global distributions of midlevel clouds using the cloud top definition between 3 and 7 km, the cloud base definition between 2 and 5 km, and the ISCCP definition (cloud top pressures between 680 and 440 hPa) for single and multi-layered cloud scenes. The multi-top represents the top layer of the multi-layered clouds, whereas the multi-bottom represents the bottom layer of the multi-layered clouds. Taken from Jin (2012).

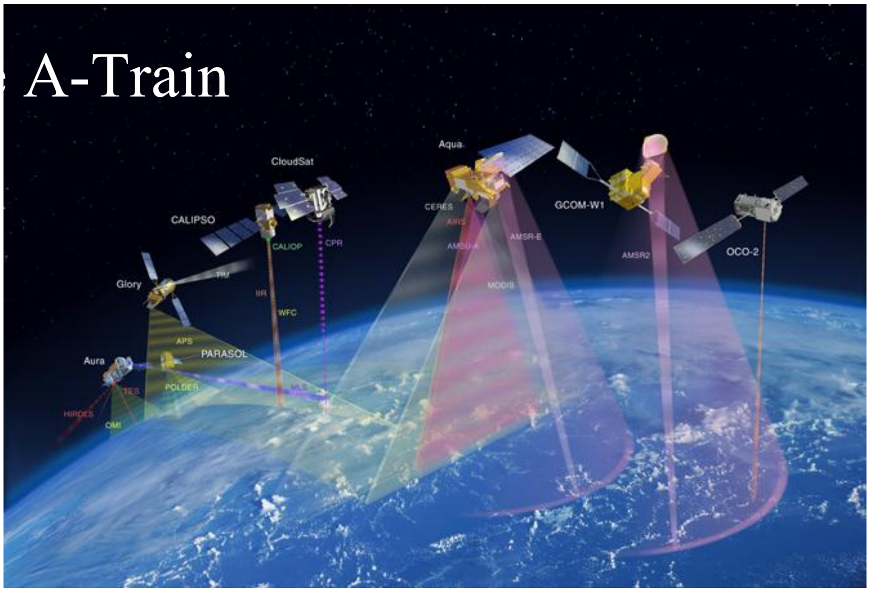

Figure 6. Artist's visualization of NASAs A-Train satellite constellation. Also shown are the relative swath widths of each instrument. AQUA, CloudSat, and CALIPSO are used in this study. Image courtesy of www.nasa.gov

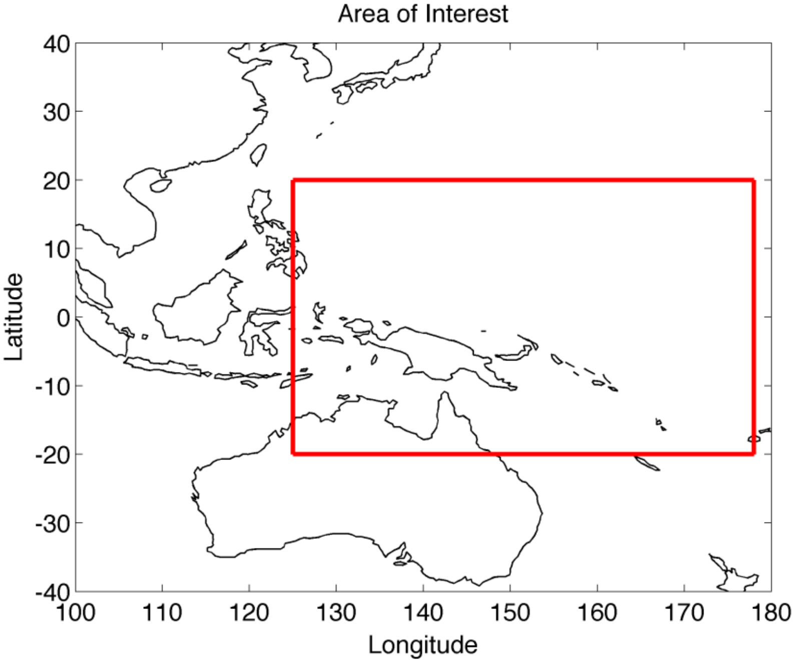

Figure 7. Area of interest for daytime, oceanic, midlevel clouds between January 2007 through December 2010.

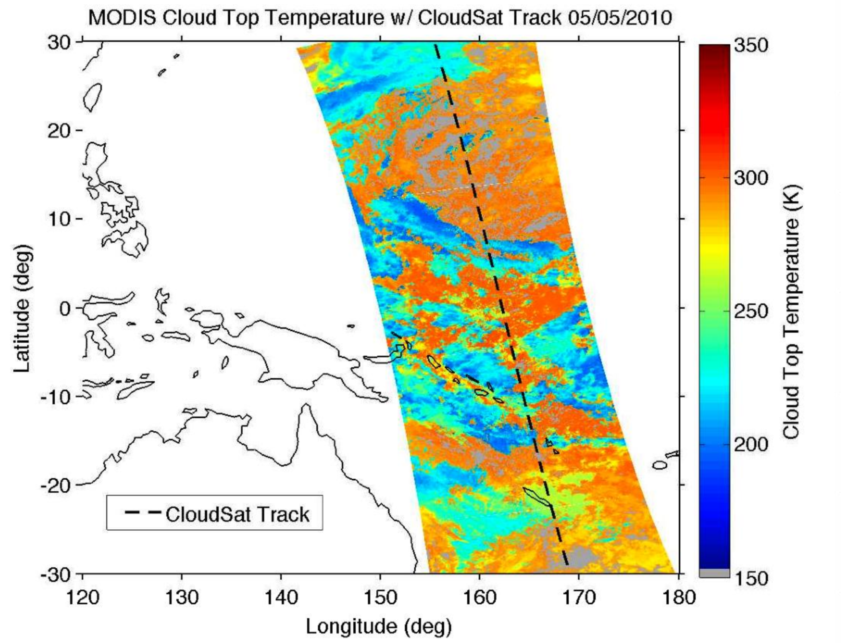

Figure 8: Comparison of the broad MODIS swath with the relatively narrow CloudSat track. Grey areas mark clear sky.

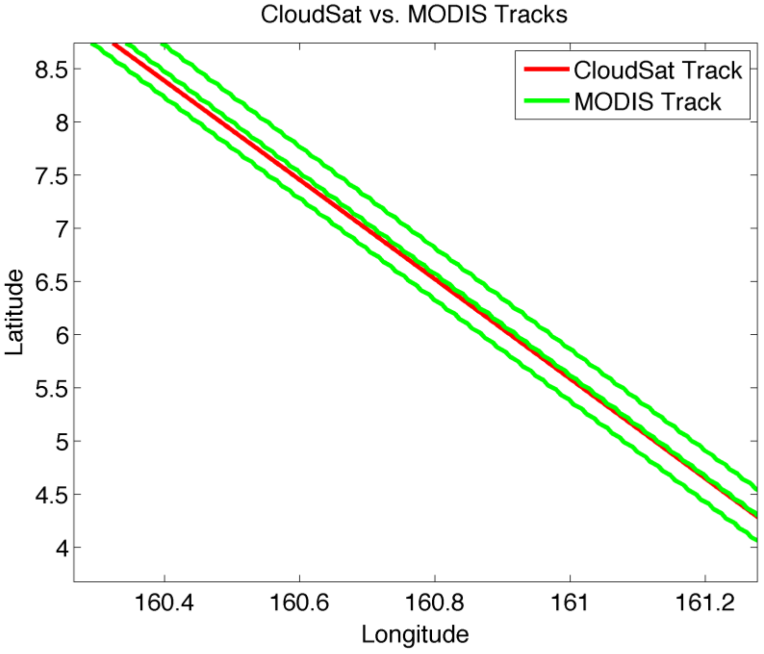

Figure 9. A comparison of the CloudSat track versus the subset MODIS pixels for an individual granule. This illustrates that the middle was chosen of the three MODIS pixels in the MAC06S0 or MAC03S0 because it best matches the CloudSat track.

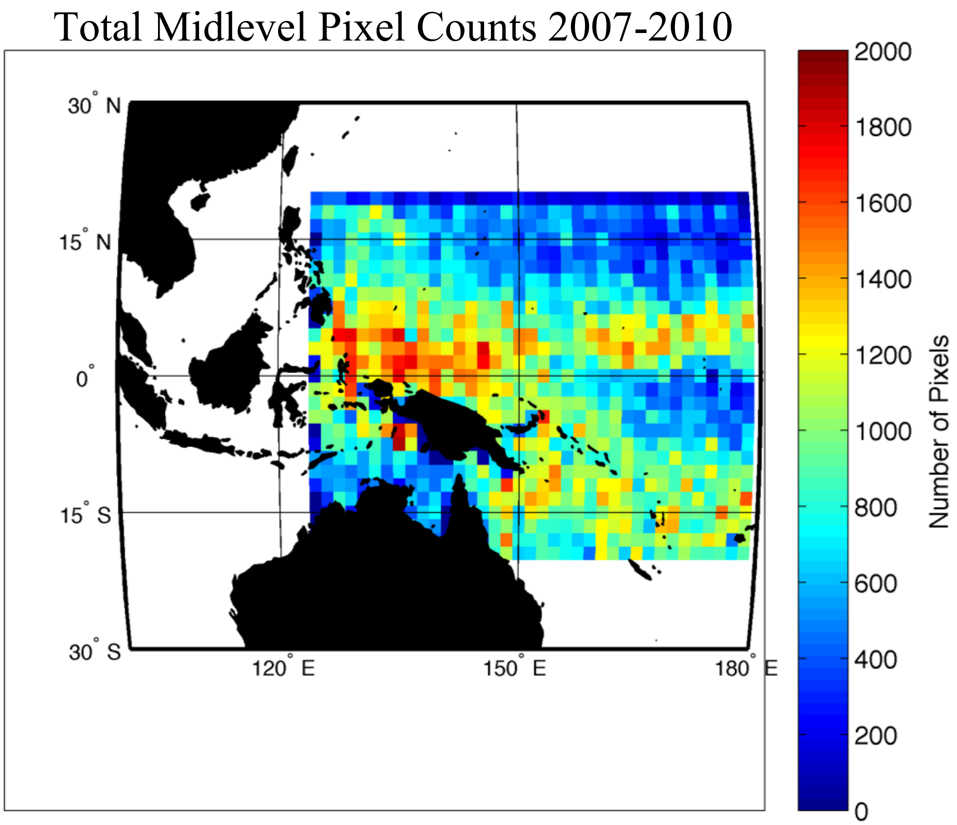

Figure 10. Geographic frequency of all single and two-layer midlevel clouds in the study region between January 2007 through December 2010. Midlevel clouds most frequently occur in the ITCZ, SPCZ, and the Pacific warm pool.

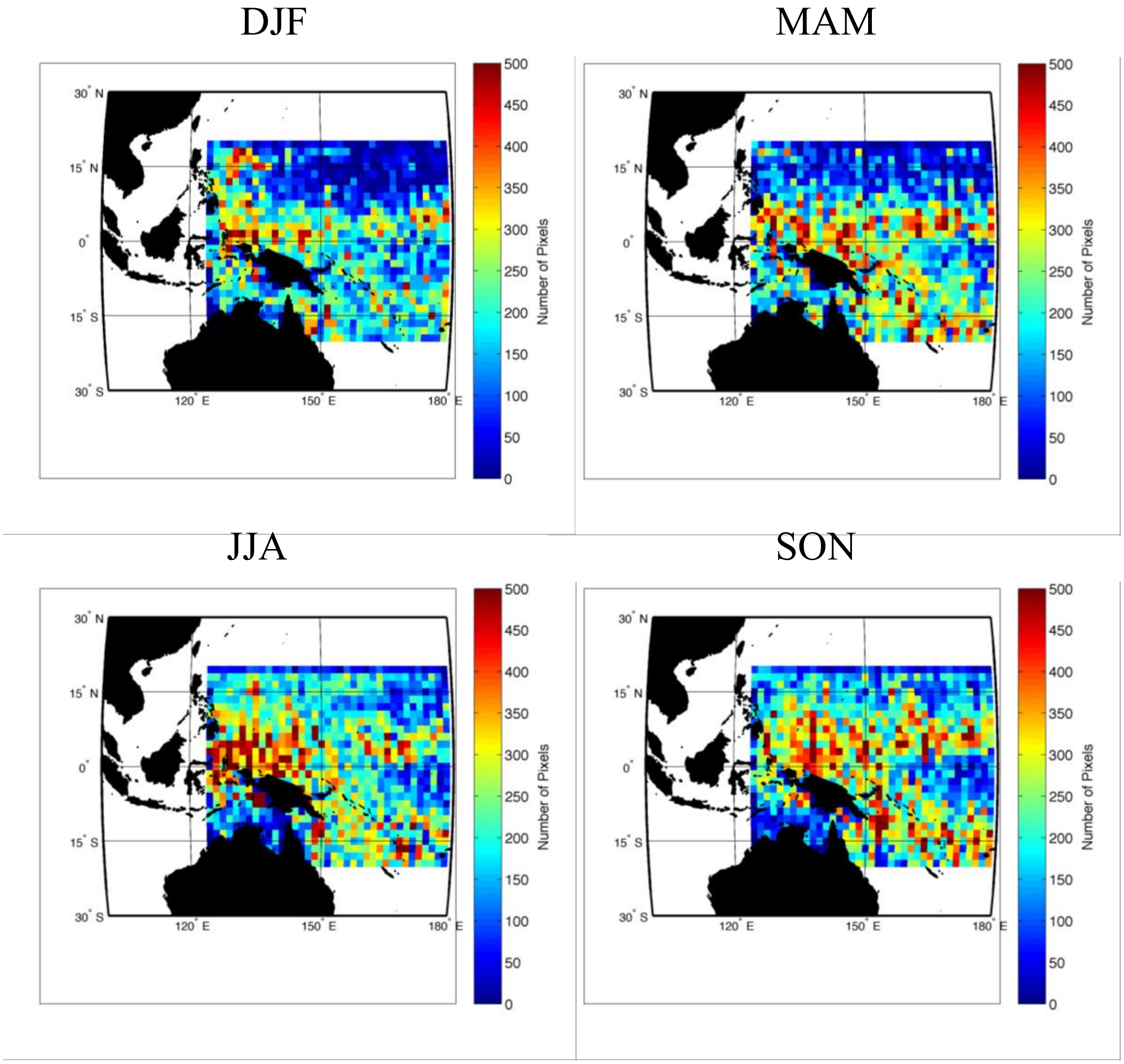
DJF

MAM

JJA

SON

Figure 11. Similar to Figure 10, but showing the seasonal dependence of the geographic frequency of midlevel clouds.

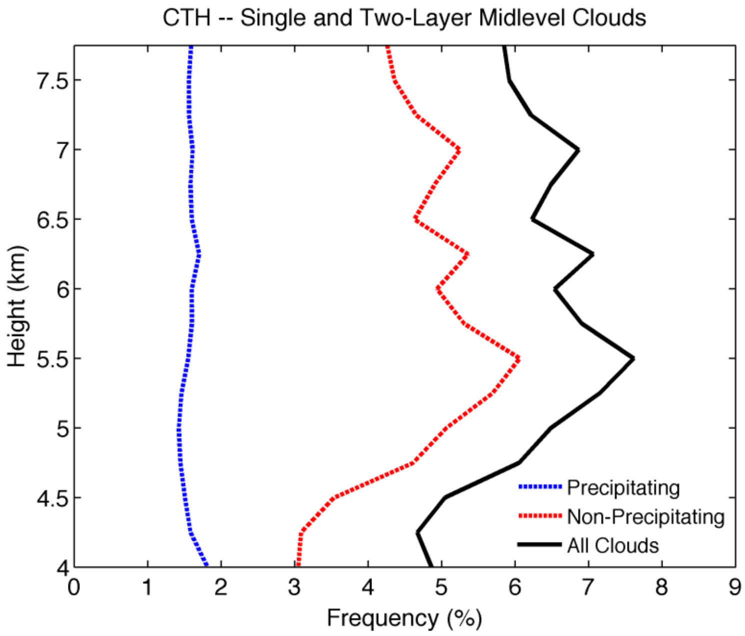

Figure 12. CTH (km) for all (black), precipitating (blue), and non-precipitating (red) single and two-layered midlevel clouds. Frequency here represents the percentage of all single and two-layer clouds at a given height.

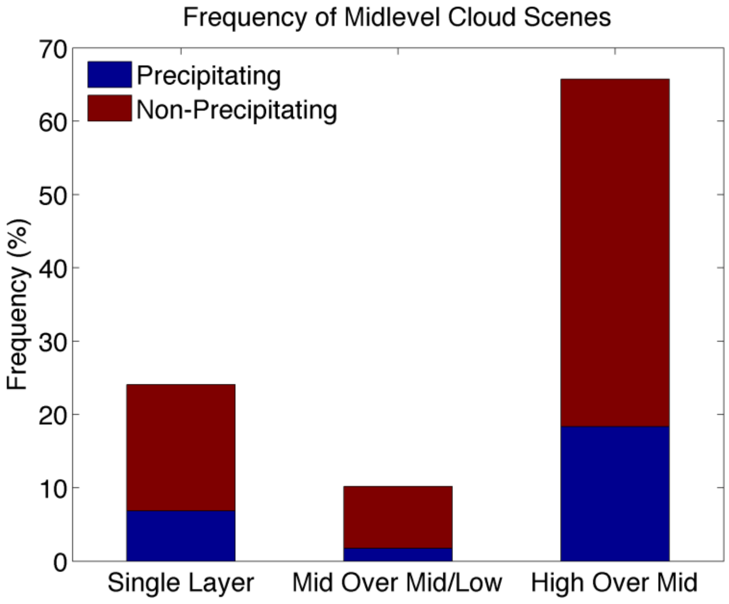

Figure 13. Fraction of total midlevel precipitating (blue) and non-precipitating (red) clouds for January 2007 through December 2010 for three different scenarios: single-layer, low under midlevel clouds, and high over midlevel clouds.

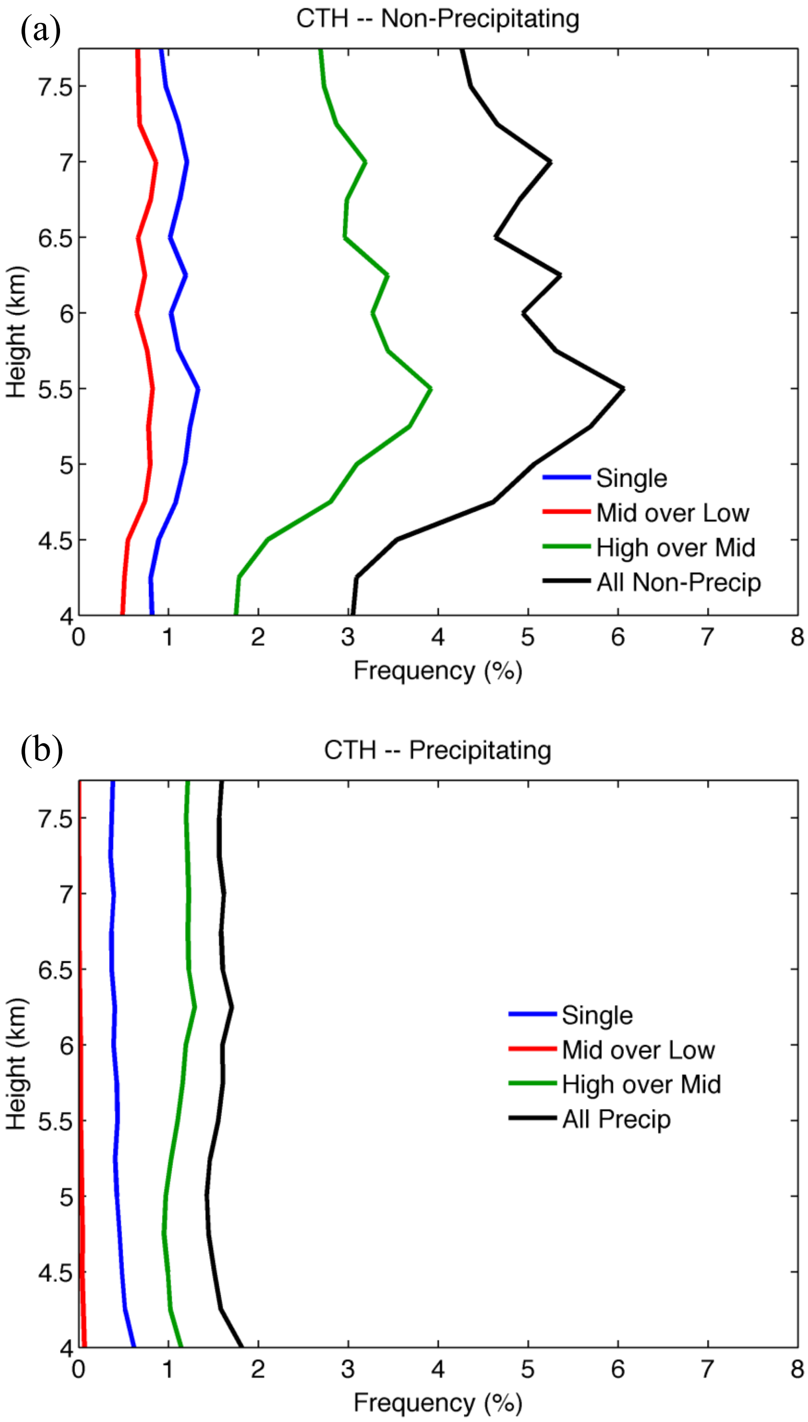

Figure 14. Midlevel CTH (km) frequency for (a) non-precipitating and (b) precipitating midlevel clouds. Frequency in both figures is relative to all single and two-layer midlevel clouds.

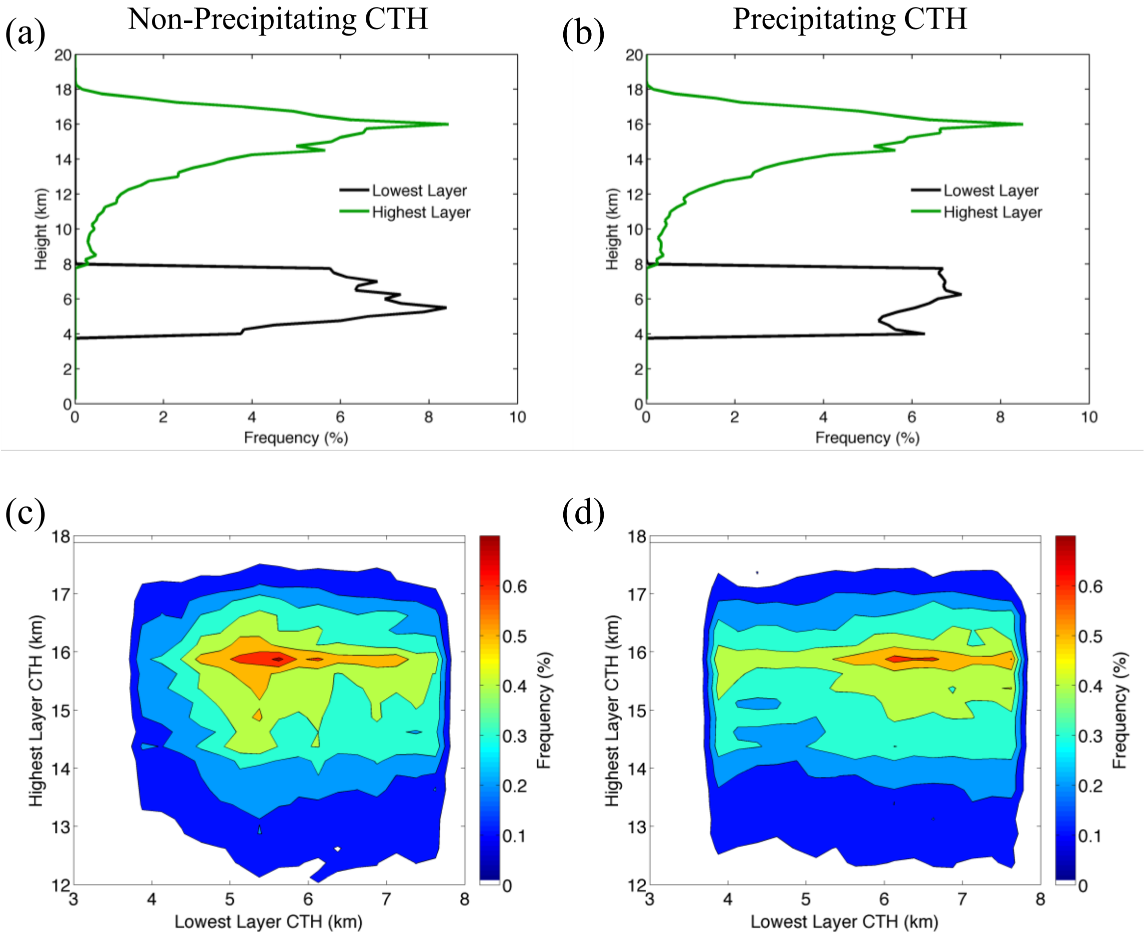

Figure 15. CTH (km) for non-precipitating and precipitating high over midlevel clouds. The top panels represent the frequency of (a) non-precipitating and (b) precipitating CTHs of both layers relative to each scenario. The bottom panels represent the joint frequency distribution of (c) non-precipitating and (d) precipitating CTHs for the two layers.

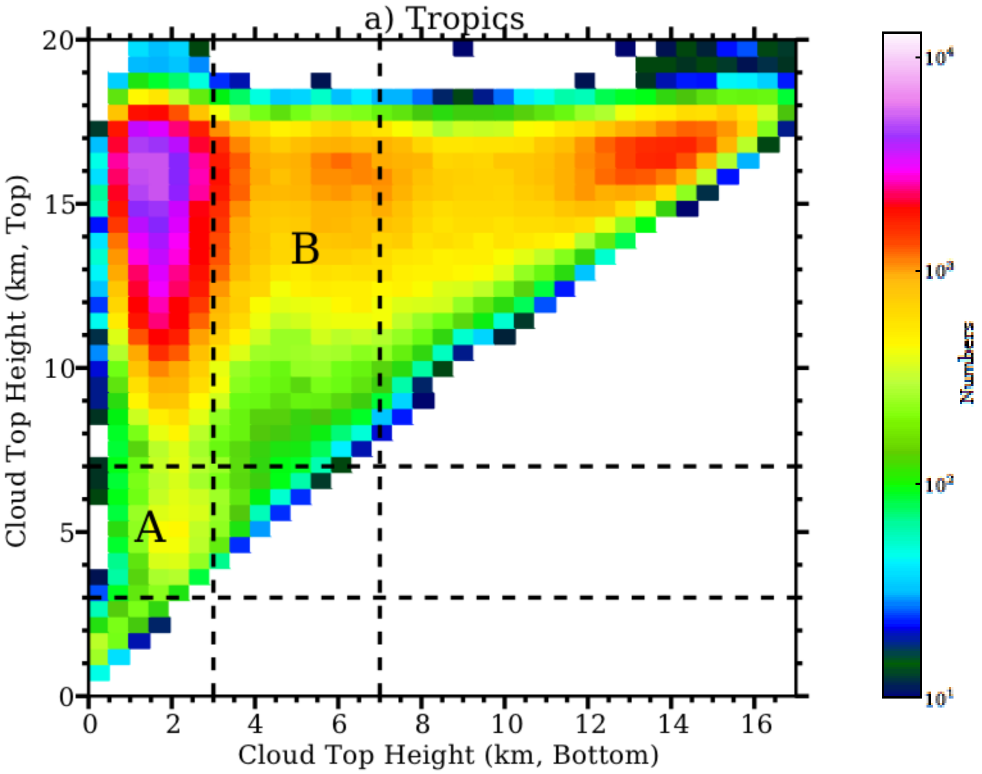

Figure 16. Joint histogram for bottom layer (x axis) and top layer (y axis) for the two layer cloud scenes. This figure only includes the tropics and the cloud top height definition (3 km < CTH < 7 km) for the midlevel from Jin (2012) Figure 3.2. Box A represents midlevel over low clouds and box B represents high over midlevel clouds. Adapted from Jin (2012).

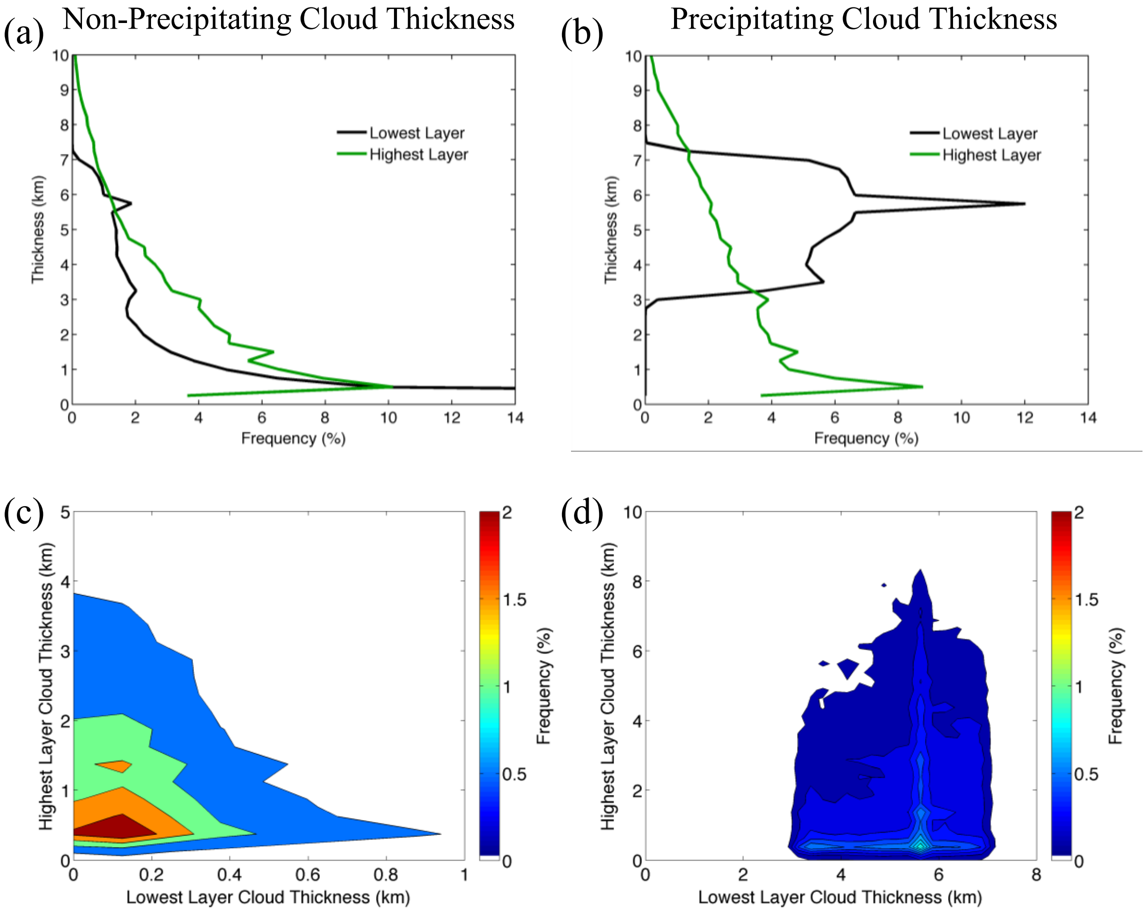

Figure 17. Geometric thickness (km) for non-precipitating and precipitating high over midlevel clouds. The top panels represent the frequency of (a) non-precipitating and (b) precipitating thicknesses of both layers relative to each scenario. The bottom panels represent the joint frequency distribution of (c) non-precipitating and (d) precipitating thickness for the two layers.

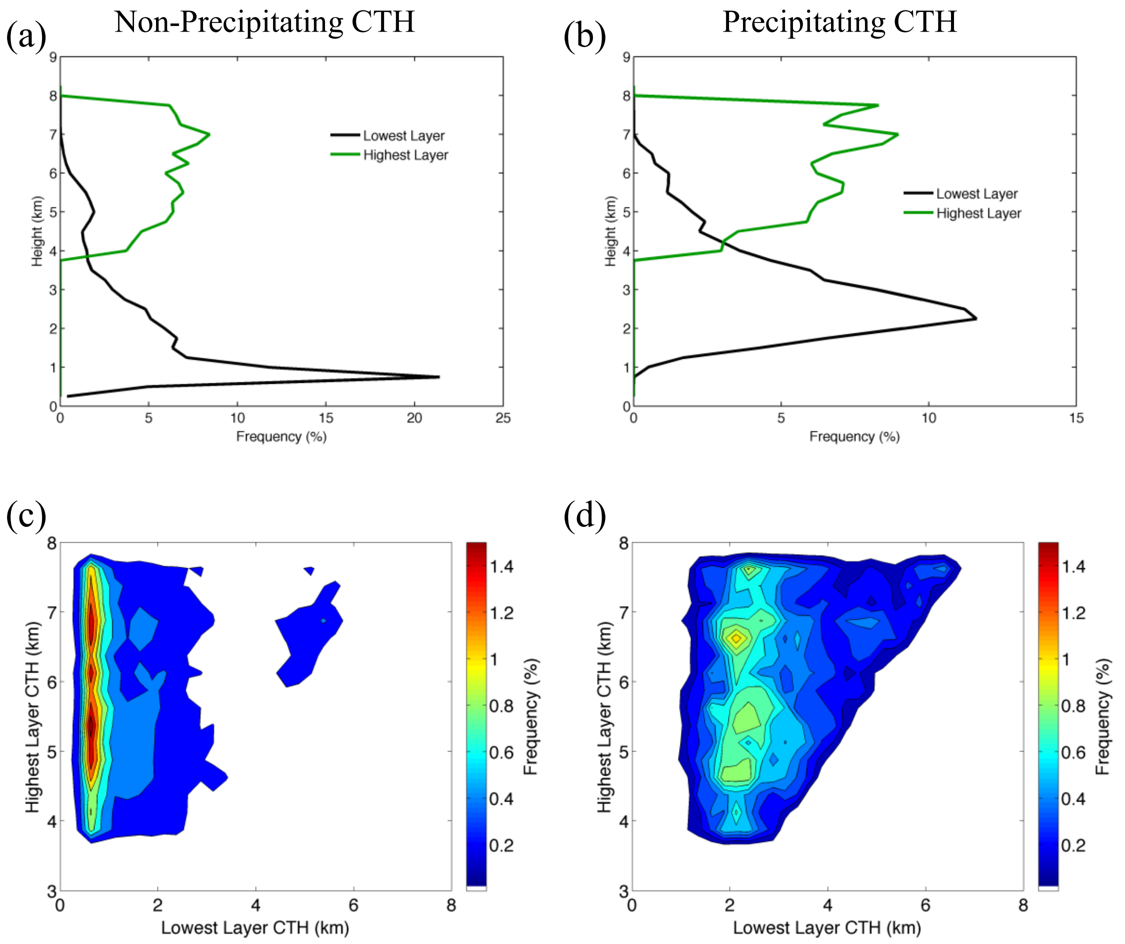

Figure 18. CTH (km) for non-precipitating and precipitating midlevel over lower level clouds. The top panels represent the frequency of (a) non-precipitating and (b) precipitating CTHs of both layers relative to each scenario. The bottom panels represent the joint frequency distribution of (c) non-precipitating and (d) precipitating CTHs for the two layers.

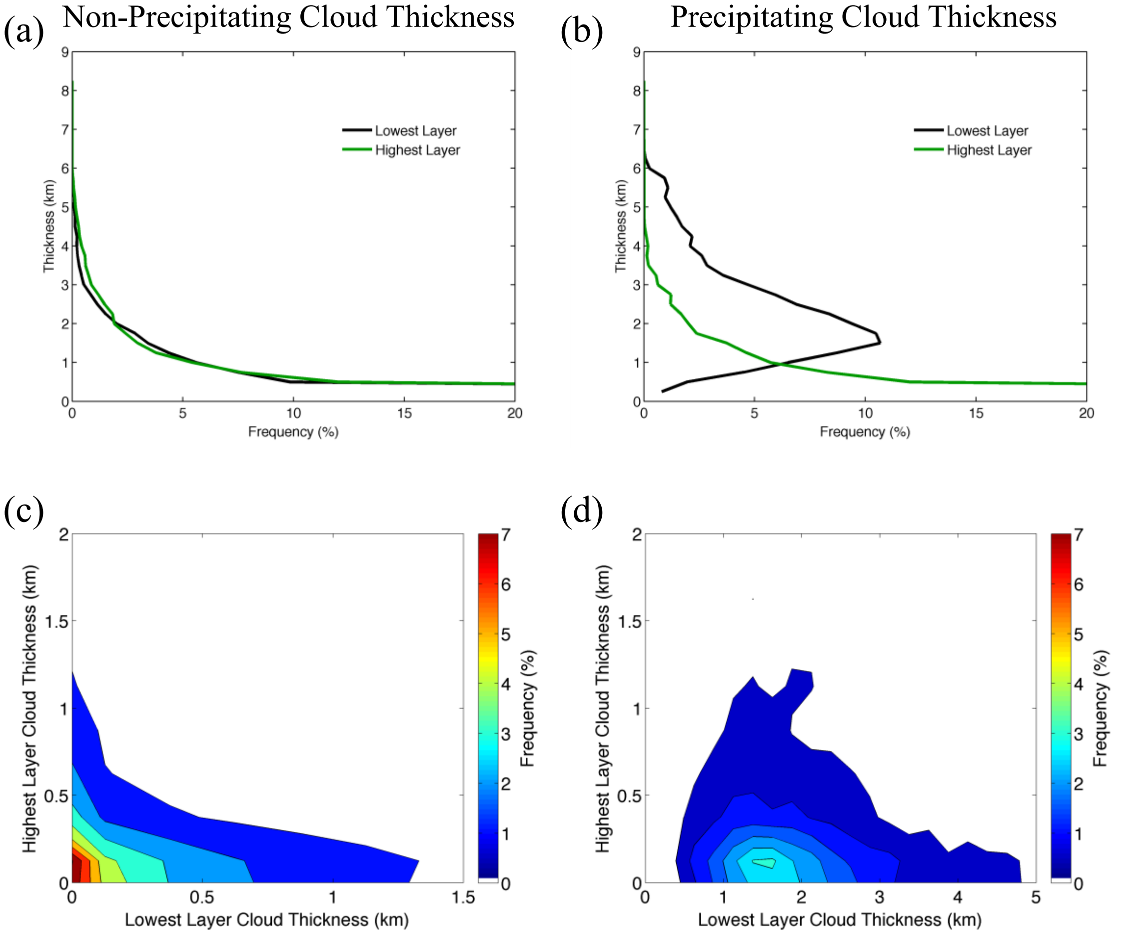

Figure 19. Geometric thickness (km) for non-precipitating and precipitating midlevel over lower clouds. The top panels represent the frequency of (a) non-precipitating and (b) precipitating thicknesses of both layers relative to each scenario. The bottom panels represent the joint frequency distribution of (c) non-precipitating and (d) precipitating thickness for the two layers.

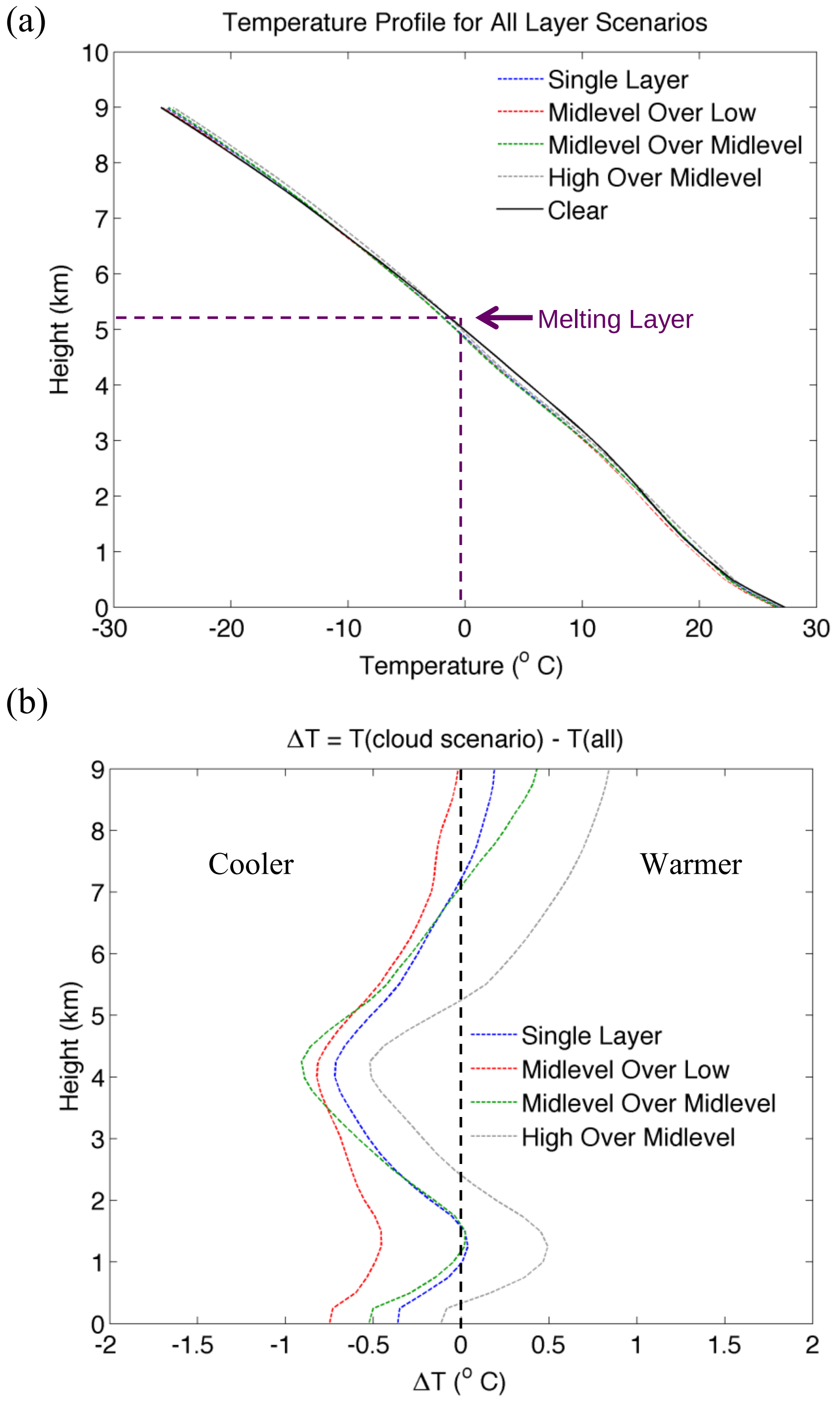

Figure 20. (a) Average temperature (°C) profile for all scenes and (b) difference in temperature between each cloud scenario and all scenes (includes all clouds and clear scenes).

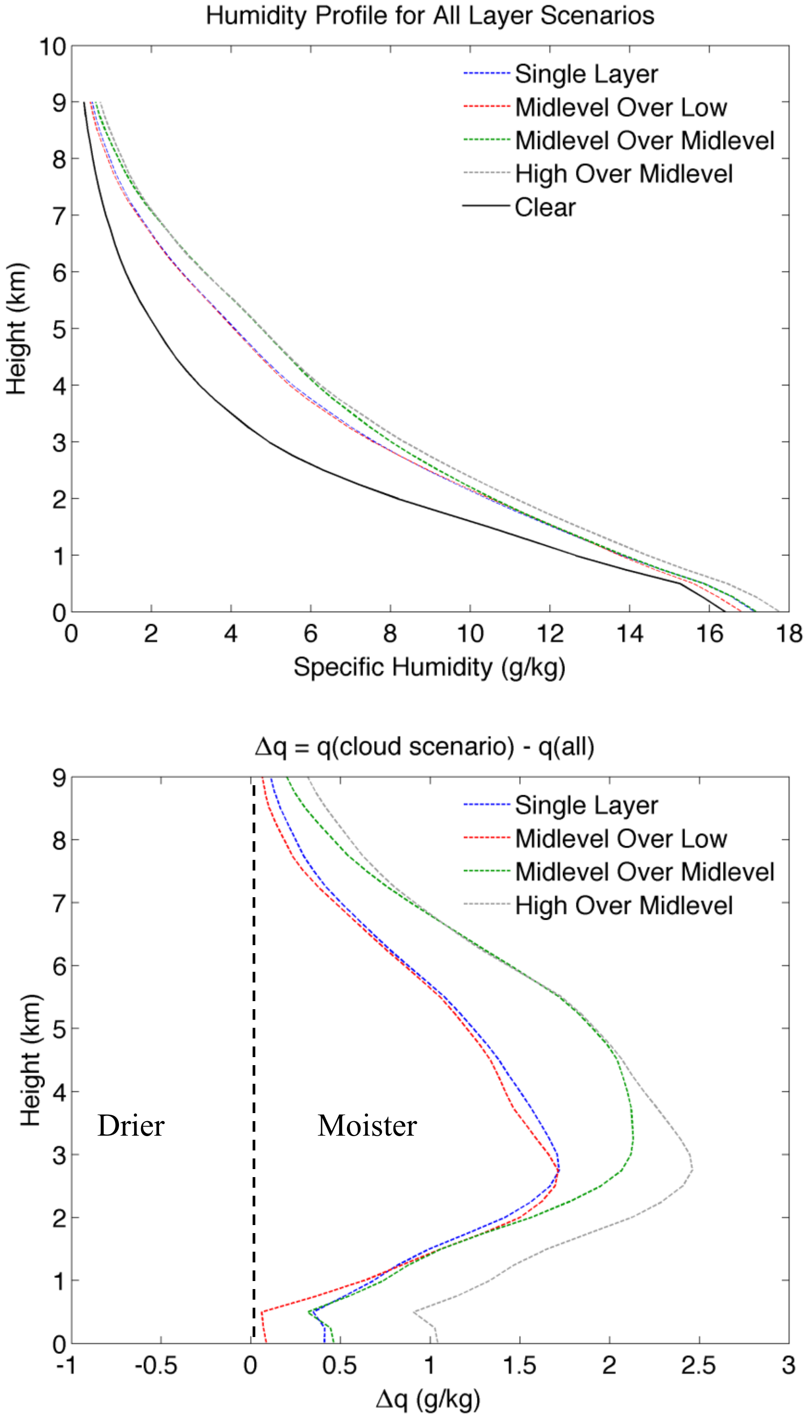

Figure 21. (a) Average specific humidity (g kg^{-1}) profile for all layers and (b) difference in specific humidity between each cloud scenario and all scenes (includes all clouds and clear scenes).

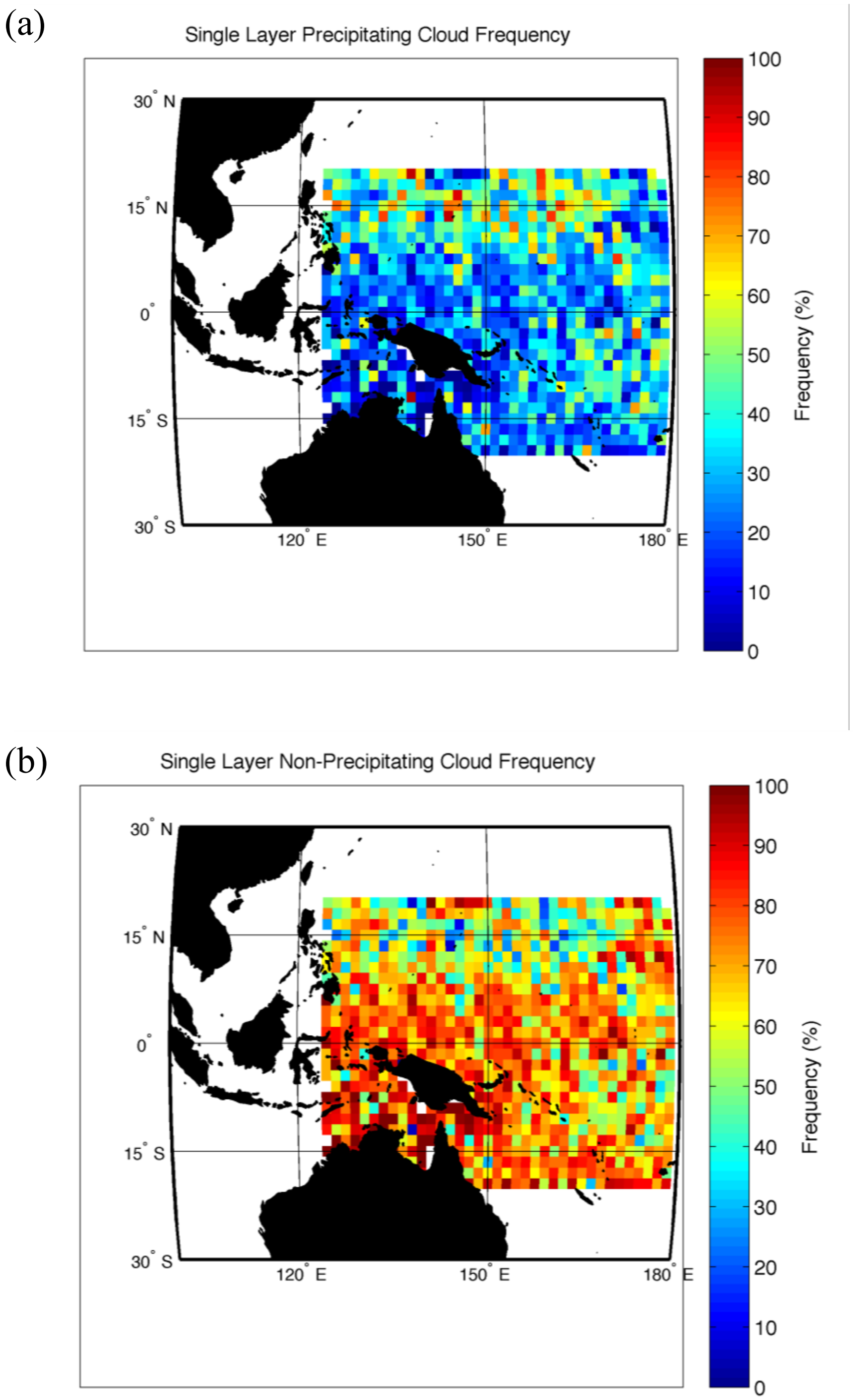

Figure 22. The spatial frequency distribution of (a) precipitating (b) and non-precipitating clouds relative to total single-layer midlevel clouds.

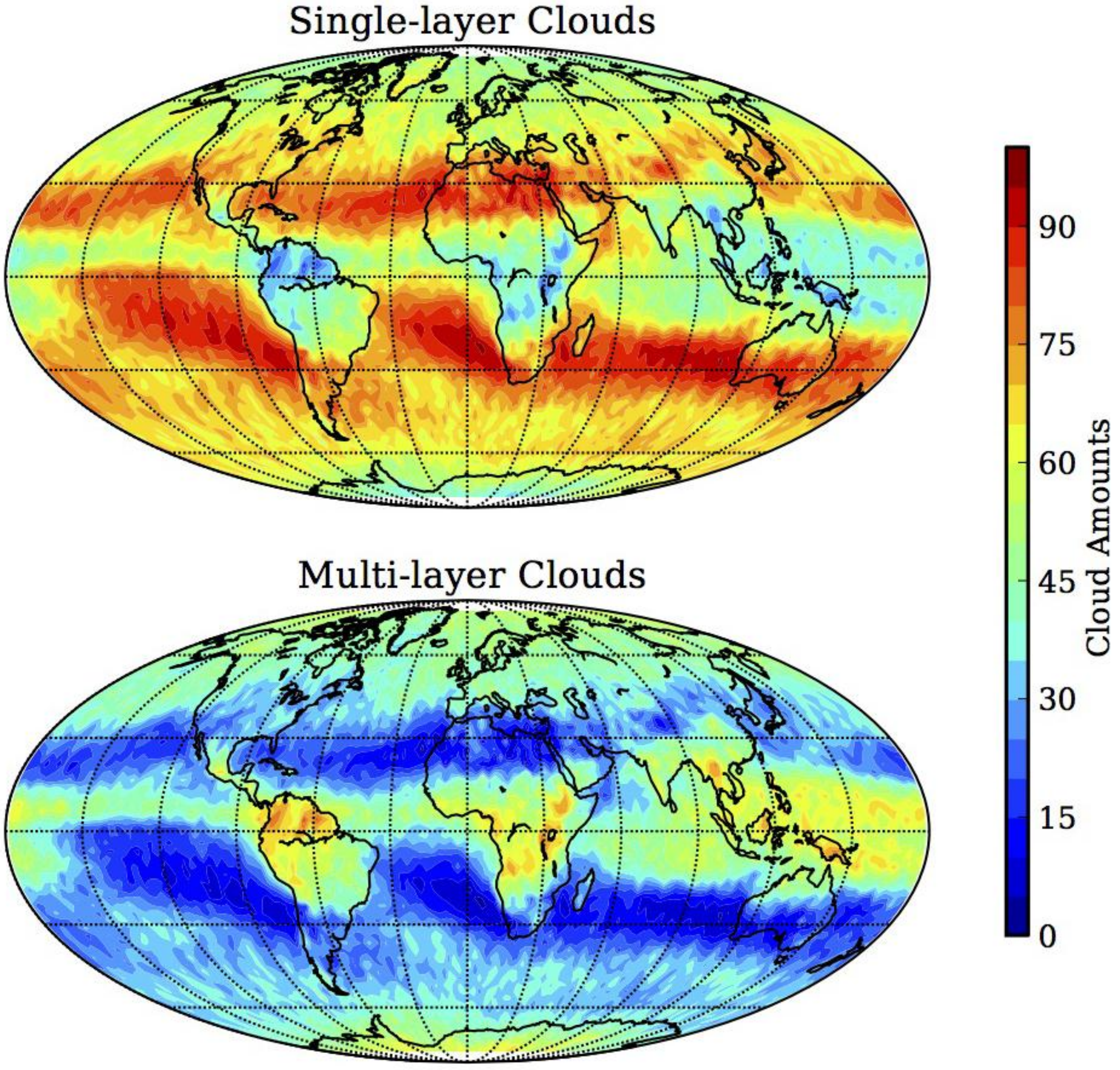

Figure 23. The global distributions of cloud amounts for single- and multi-layered clouds from collocated CALIPSO and CloudSat between December 2007 and November 2008. Cloud amounts here represent the fraction of either single-layer or multi-layer clouds with respect to the total merged cloud profiles. Latitude lines are shown for 0°, ±30°, and ±60°. Adapted from Jin (2012), Figure 2.1.

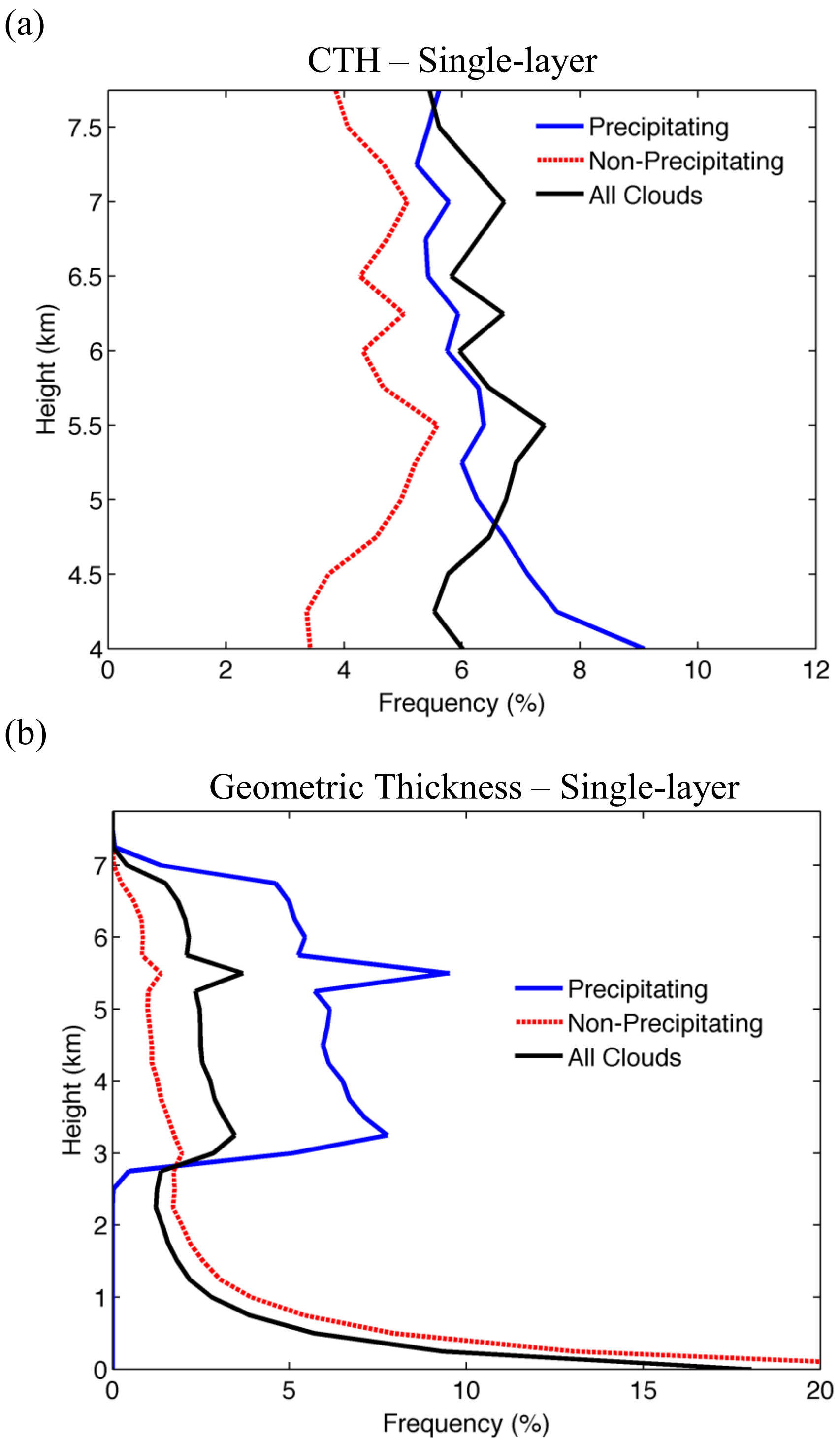

Figure 24. Frequency distributions of (a) CTH (km) for single-layer clouds and (b) geometric thickness (km) for all single-layer midlevel clouds relative to either total precipitating, non-precipitating, or all single-layer clouds.

(a) Liquid Cloud Optical Depth

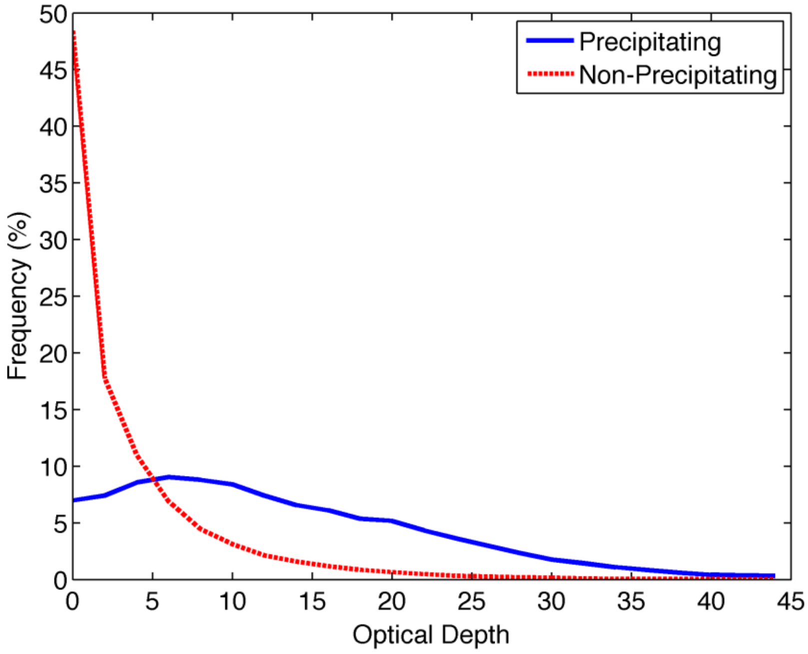

(b) Ice Cloud Optical Depth

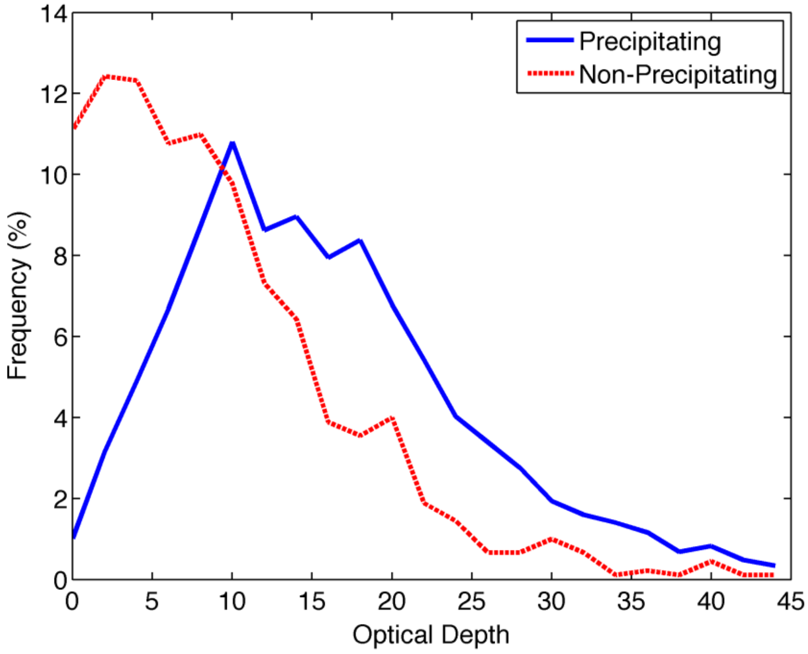

Figure 25. Frequency distribution of optical depth for precipitating and non-precipitating clouds for both (a) liquid phase and (b) ice phase . Frequency is relative to either precipitating or non-precipitating scenarios. Phase is determined from the Phase Subset data.

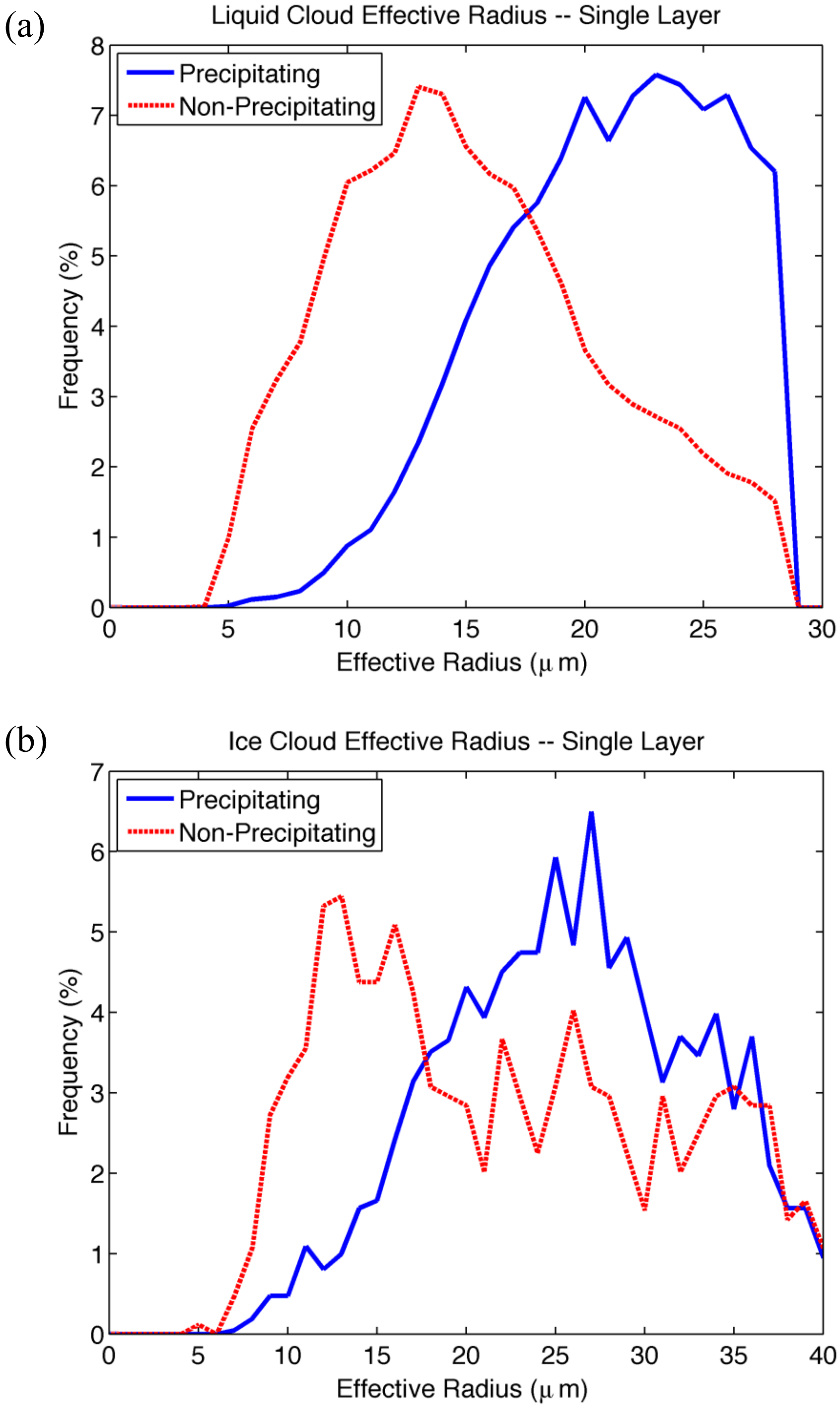

Figure 26. Frequency distribution of effective radius (μm) for precipitating and non-precipitating clouds for both (a) liquid phase and (b) ice phase. Frequency is relative to either precipitating or non-precipitating scenarios.

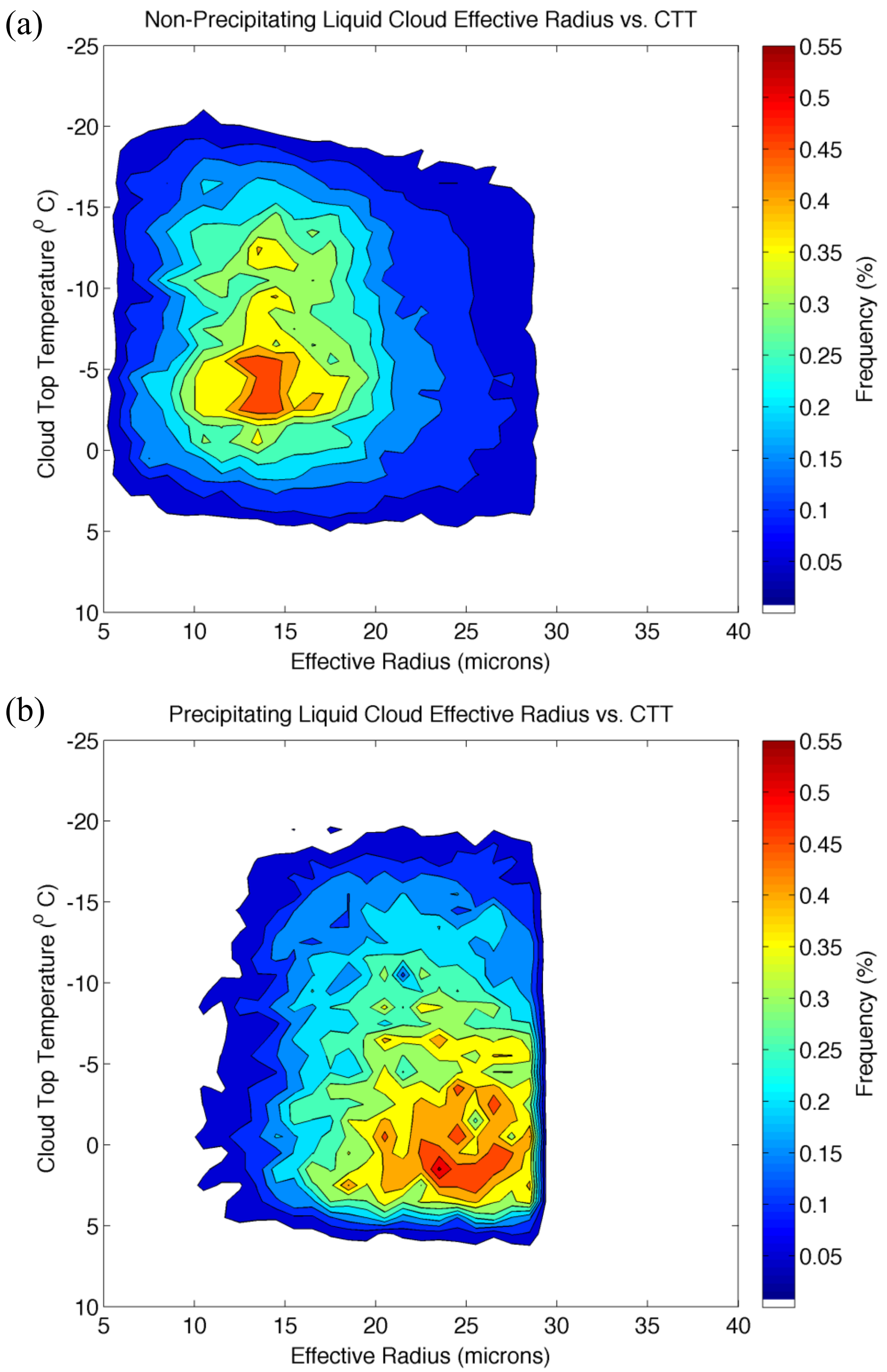

Figure 27. Joint frequency distribution of effective radius (μm) and CTT (°C) for a) non-precipitating and b) precipitating single-layer midlevel clouds.

(a) LWP – Single-layer

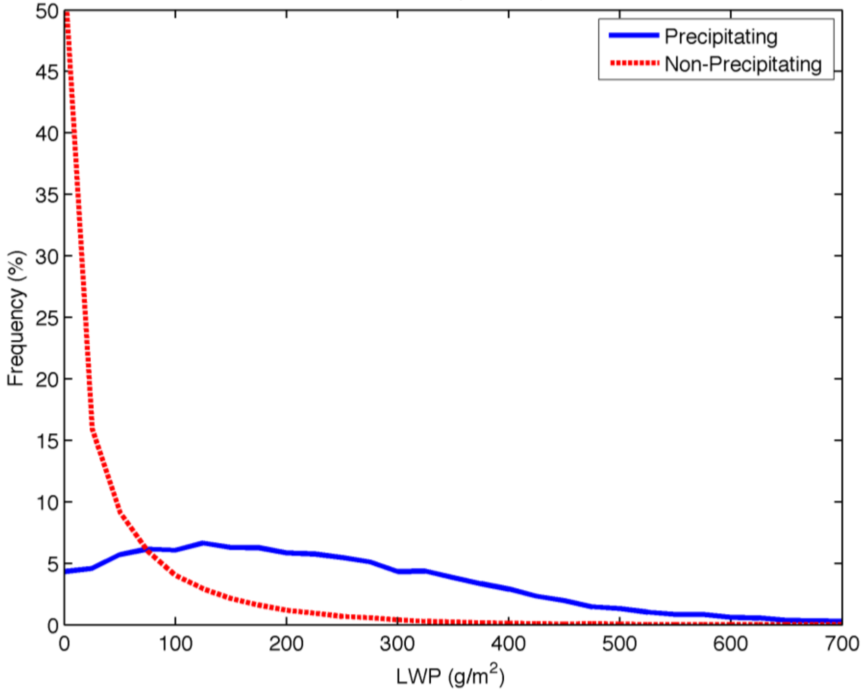

(b) IWP – Single-layer

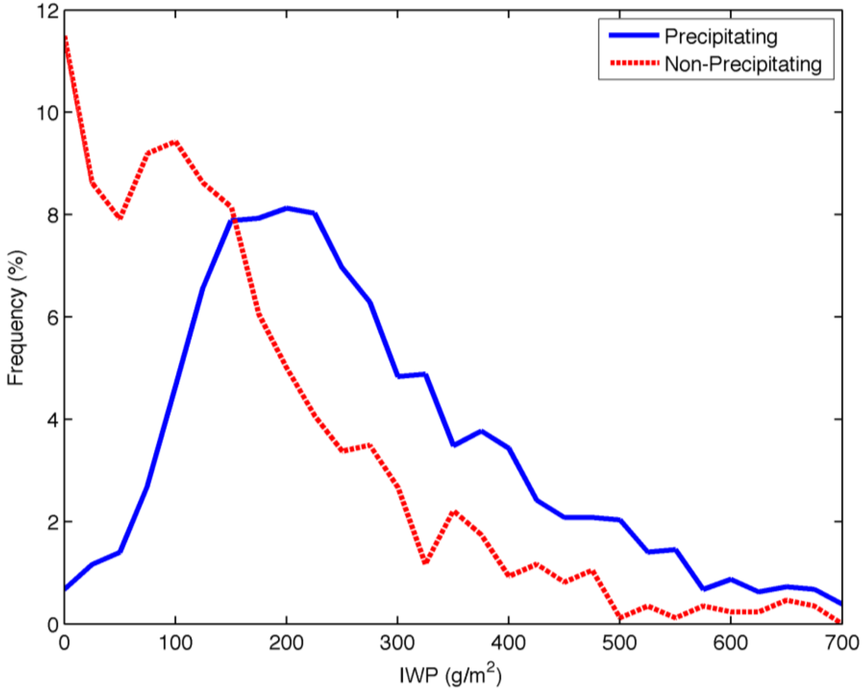

Figure 28. Frequency distribution of water path (gm^{-2}) for precipitating and non-precipitating clouds for both (a) liquid phase and (b) ice phase. Frequency is relative to either precipitating or non-precipitating scenarios.

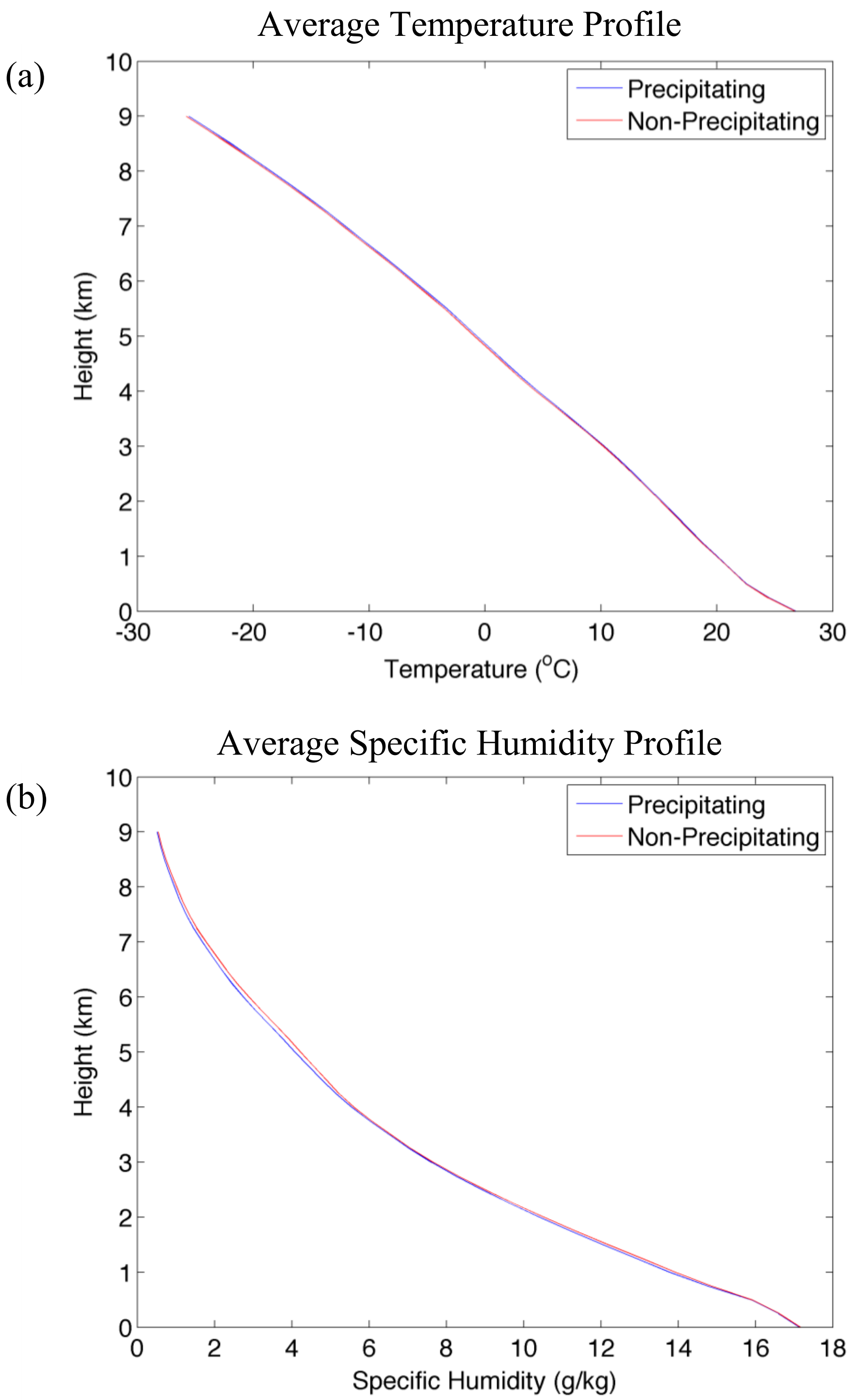

Figure 29. Environmental profile for (a) temperature (°C) and (b) specific humidity (gkg^{-1}) for single-layer clouds. Note the similarities between precipitating and non-precipitating clouds.

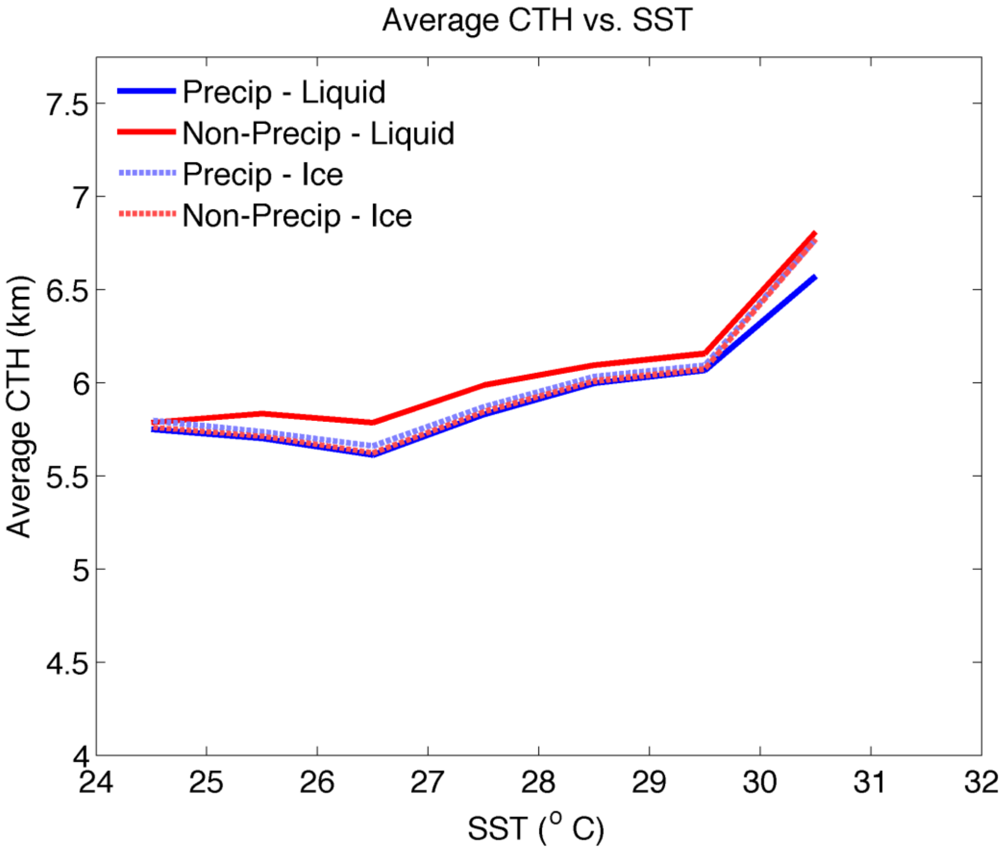

Figure 30. Average CTH (km) with respect to SST (°C).

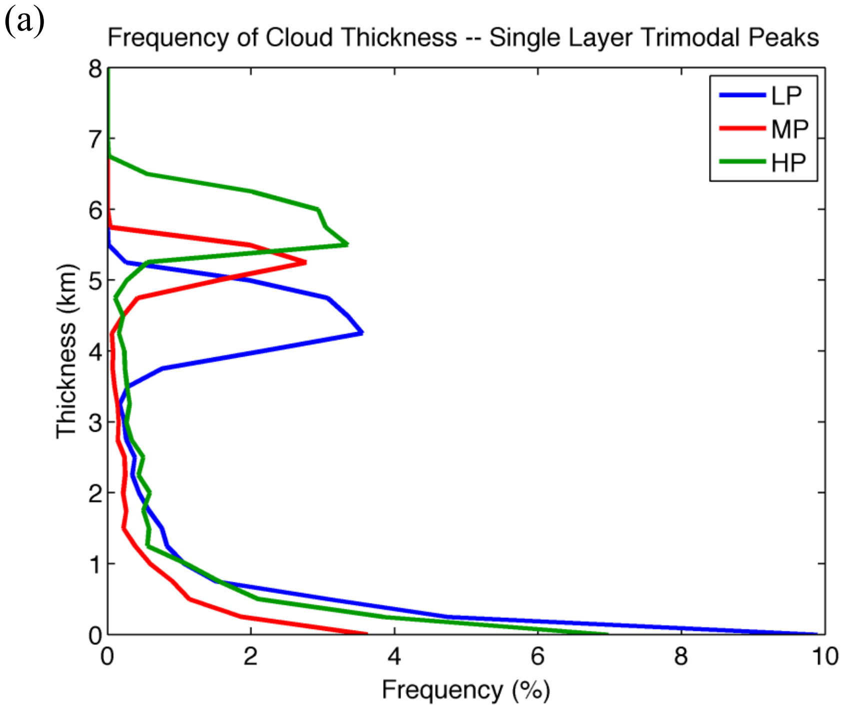

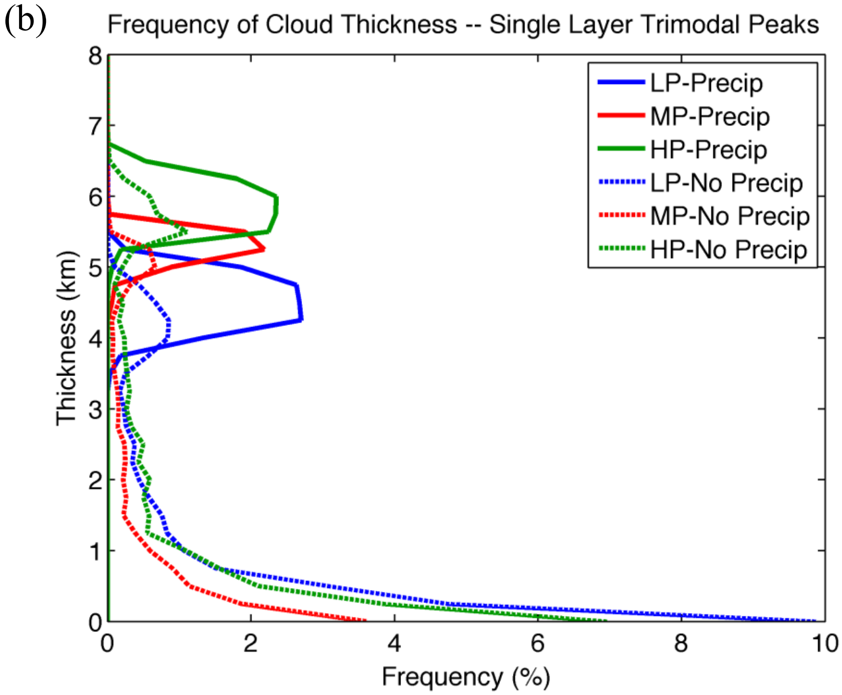

Figure 31. Frequency of single-layer trimodal peak thickness for a) all peak clouds and b) precipitating and non-precipitating peak clouds relative to total clouds in each peak. (LP = low peak, MP = mid peak, and HP = high peak)

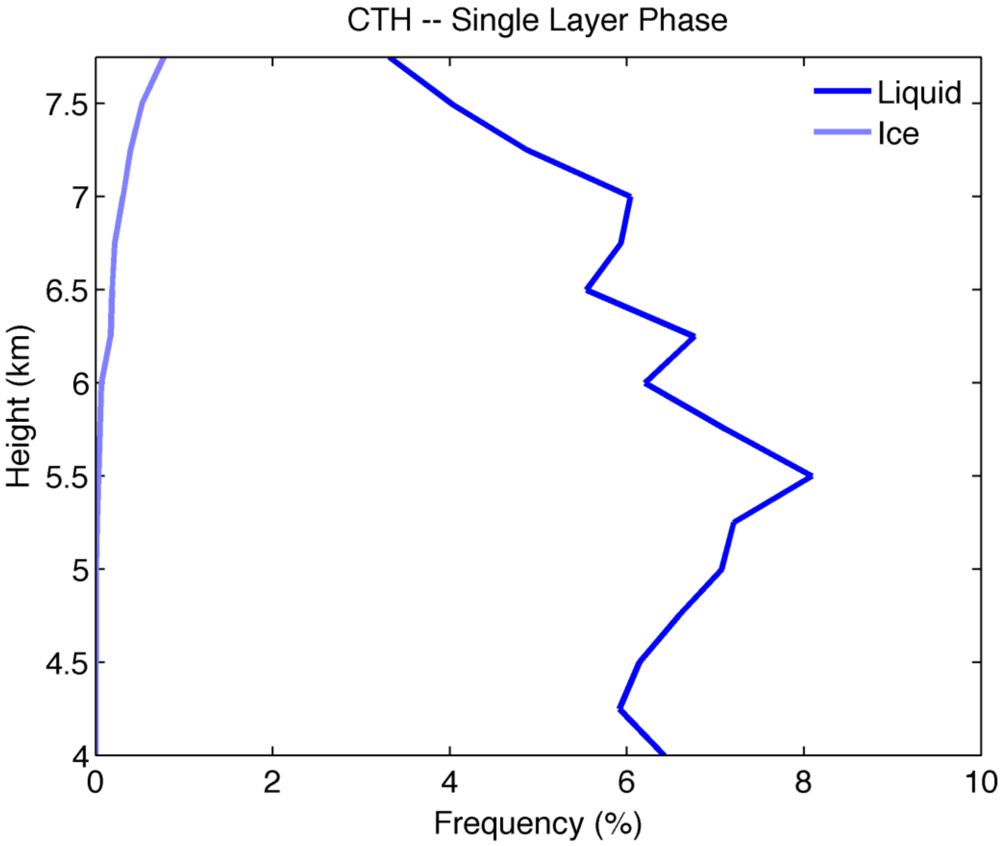

Figure 32. CTH (km) frequency of liquid and ice single-layer midlevel clouds relative to total single-layer midlevel clouds.

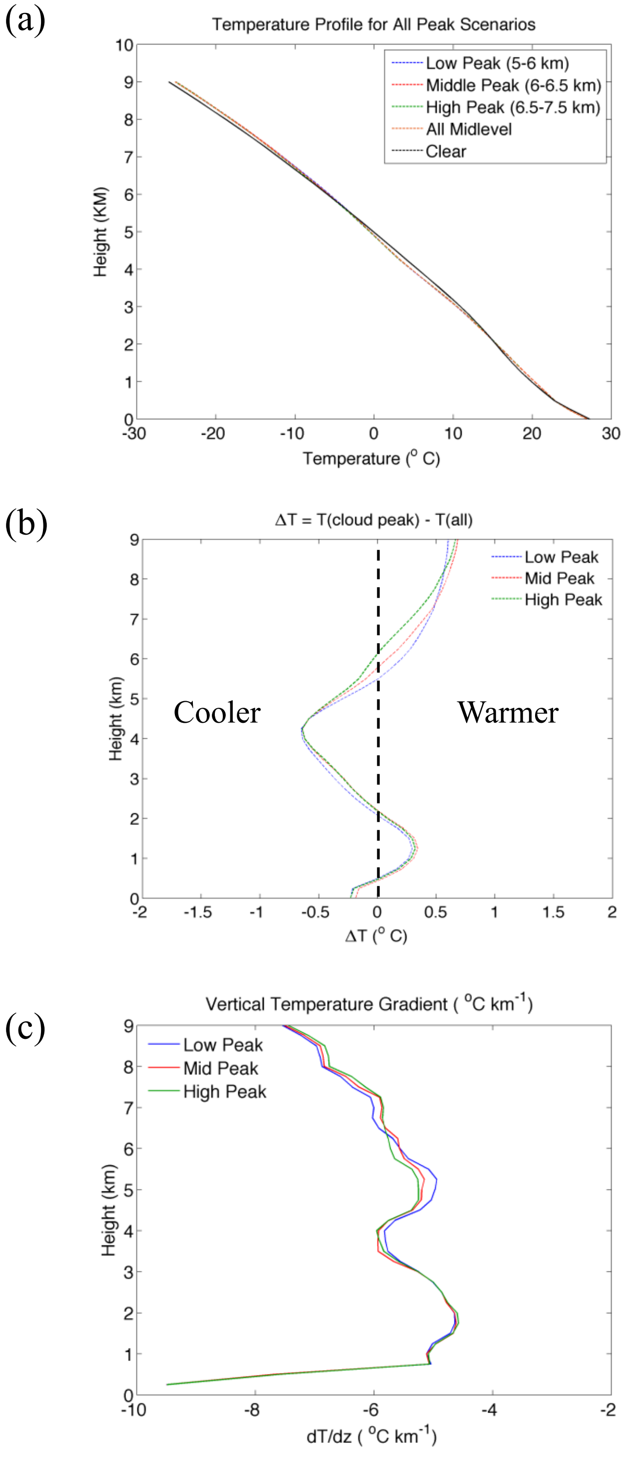

Figure 33. (a) Average temperature profile (°C) for each individual peak and (b) shows the difference (ΔT) in temperature between each cloud scenario and all scenes (all cloud and clear scenes) and (c) shows the vertical temperature gradient (°C km^{-1}).

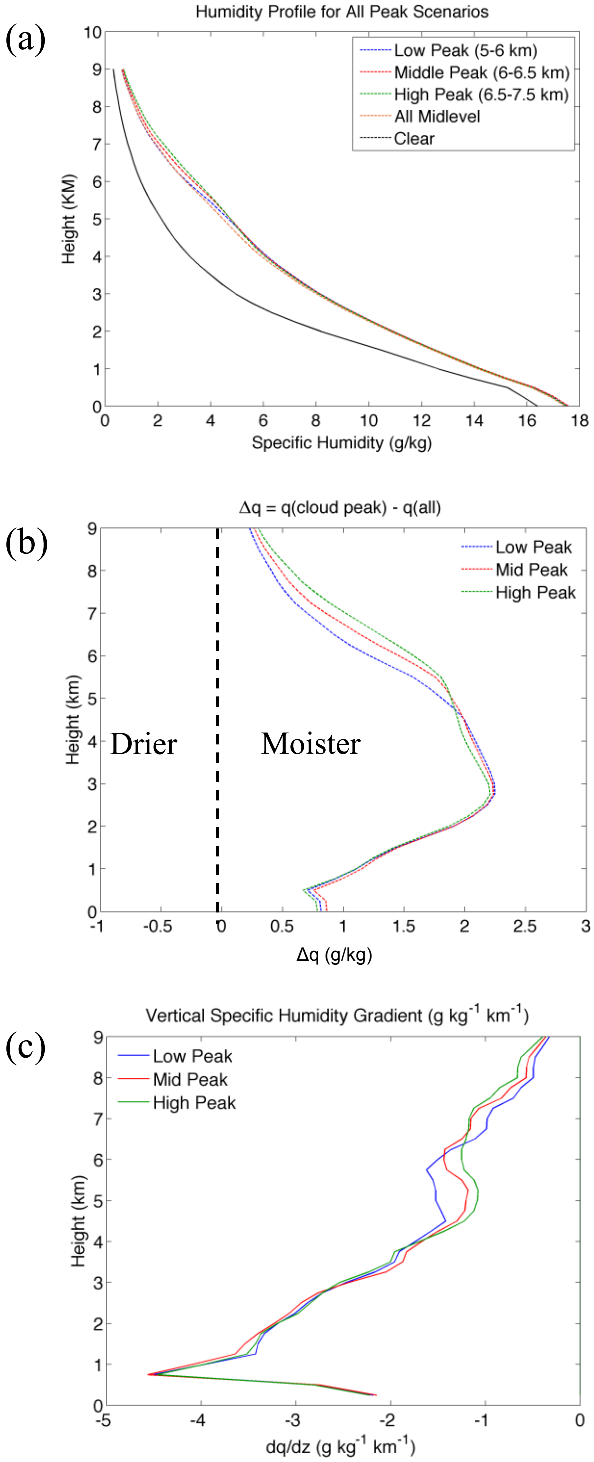

Figure 34. (a) Average atmospheric specific humidity (q) profile and (b) shows the difference in q (Δq) between each cloud scenario and all scenes (all cloud and clear scenes) and (c) shows the vertical specific humidity gradient (g kg^{-1} km^{-1}).

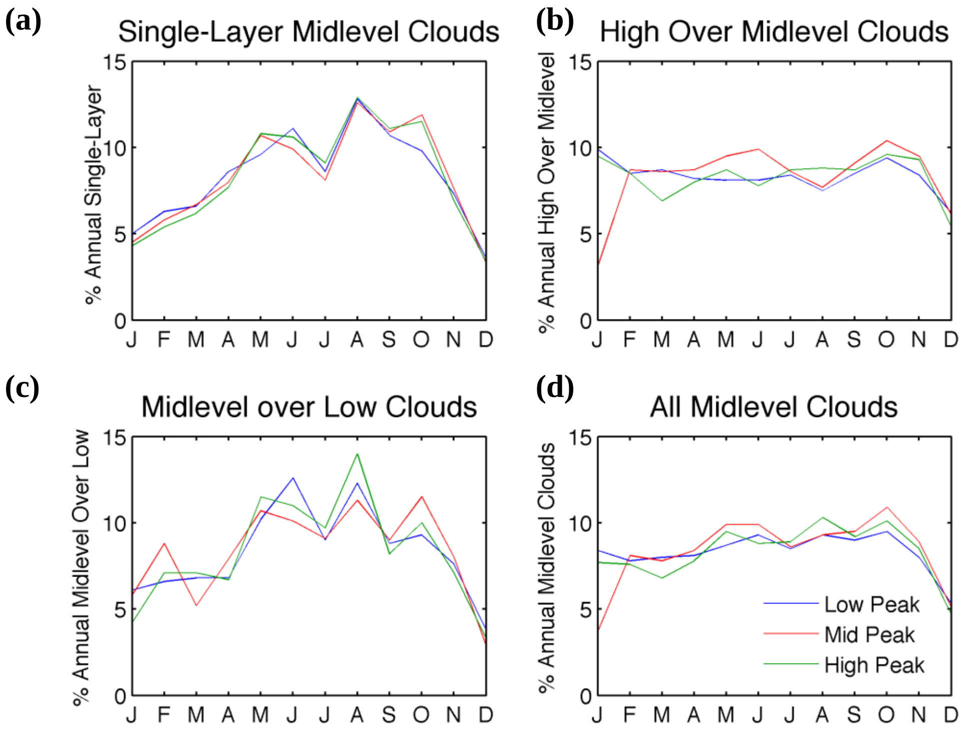

Figure 35. The seasonal cycle of the three peaks' frequency for the different cloud layer scenes and all single and two-layered midlevel clouds relative to the annual frequency of clouds in each category.

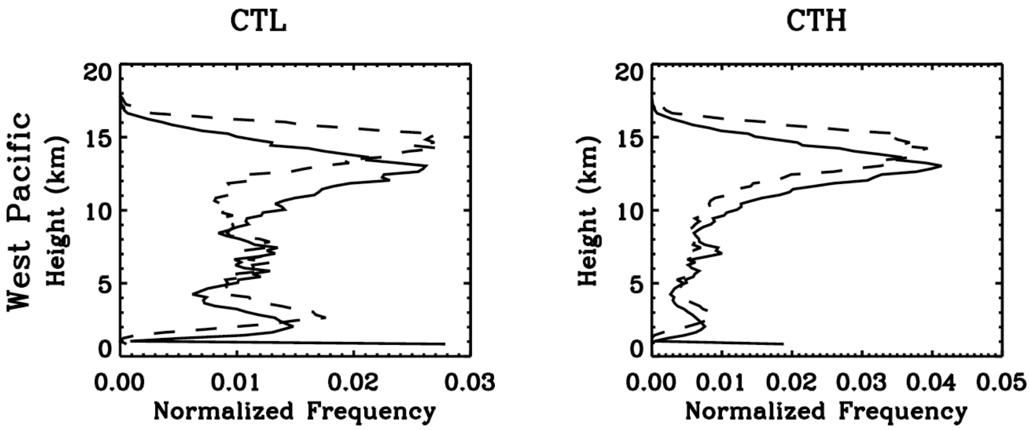

Figure 36. Vertical profiles for the lowest layer cloud top height (CTL) and the highest layer cloud top height (CTH) for the West Pacific Ocean. The solid lines represent all clouds and the dashed are precipitating clouds. Each profile is normalized by the total occurrence of the respective cloud type. In each case there is evidence of a bimodal distribution. Adapted from Haynes and Stephens (2007), Figure 4.

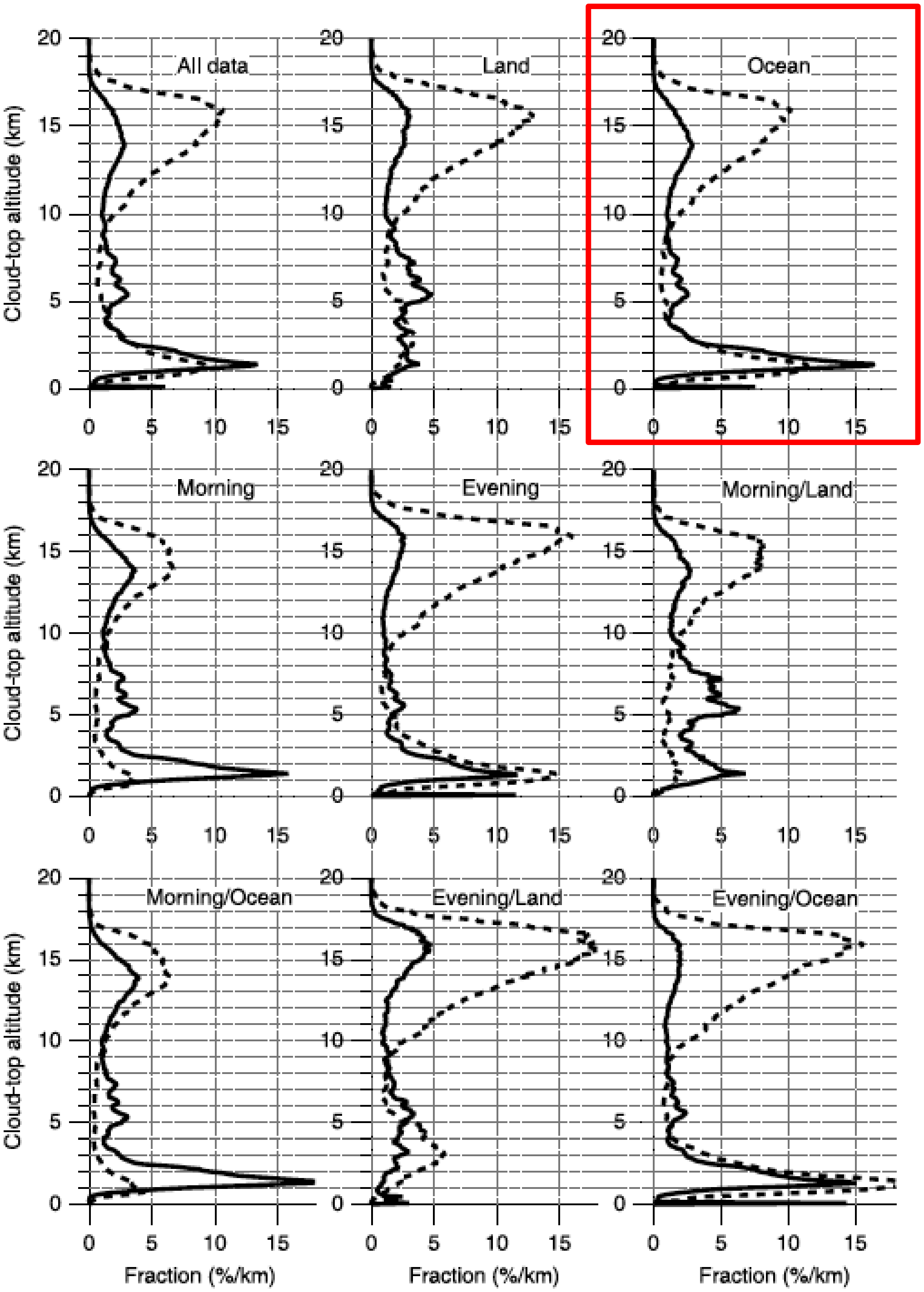

Figure 37. Vertical frequency distribution of GLAS observations (percent per km) between 10°S and 20°N. The solid lines are for thick clouds, and the dashed lines are for thin clouds. Taken from Dessler et al. (2006), Figure 2.

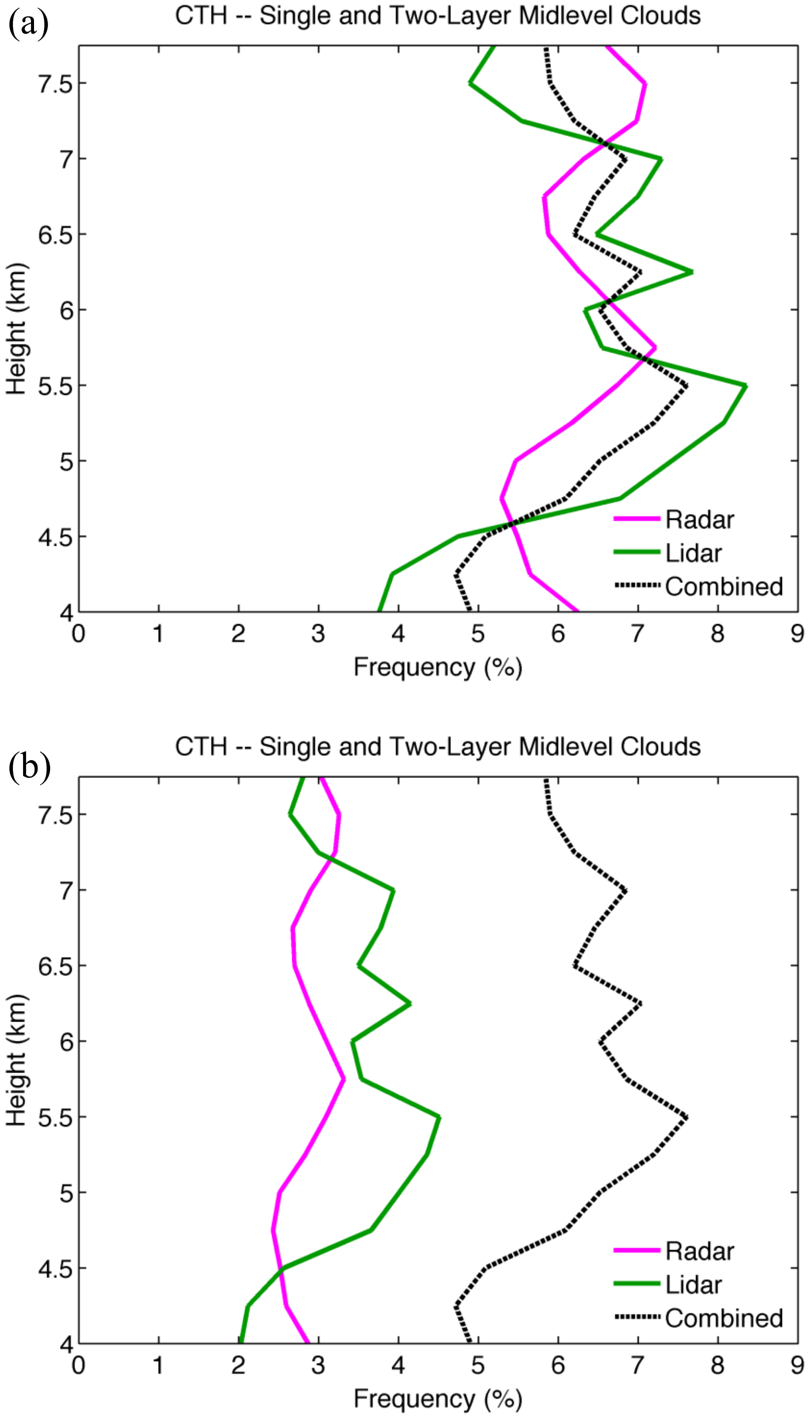

Figure 38. Vertical distribution of CTH (km) frequency for cloud tops detected by only radar, only lidar, and total midlevel clouds. (a) Frequency relative to each instrument and (b) frequency relative to total single- and two-layer midlevel clouds.